



Numéro National de Thèse : 2022LYSEN005

THÈSE DE DOCTORAT DE L'UNIVERSITÉ DE LYON

opérée par

l'École Normale Supérieure de Lyon

École Doctorale N° 206

École Doctorale de Chimie (Chimie, Procédés, Environnement)

Spécialité : Chimie Théorique

Discipline : Chimie

Soutenue publiquement le 18/03/2022, par :

Muhammad Akif Ramzan

***Ab-initio* simulations of catalytic transformation of biomass-derived molecules to building blocks of industrial interest**

Simulations *ab initio* de la transformation catalytique de molécules issues de la biomasse en sous-unités d'intérêt industriel

Devant le jury composé de :

Jean-François PAUL	Professeur	Université de Lille	Rapporteur
Karoliina HONKALA	Professeure	University of Jyväskylä	Rapporteuse
Tzonka MINEVA	Directrice de Recherche	Université Montpellier	Examinatrice
Carine MICHEL	Chargée de recherche CNRS	ENS de Lyon	Directrice de thèse
Raphael WISCHERT	Ingénieur Recherche	Solvay, Shanghai	Co-encadrant de thèse

In loving memory of my dad,

Our beloved Abu Jee

افسر دگی نہیں طربِ انشائے التفات
ہاں دردِ بن کے دل میں مگر جا کرے کوئی
(غالب)



Acknowledgements

First of all, I would like to thank my supervisor Dr. Carine Michel for all her guidance, support, encouragement and patience during the course of this PhD work, in general, and writing of this manuscript, in particular. Special thanks to her for reading this thesis as it was being written and suggesting valuable corrections and improvements. I am also grateful to Drs. Raphael Wischert and Marc Pera-Titus for their valuable comments and input during all the meetings we had with experimental collaborators and people from Solvay. My gratitude also goes to Dr. Stephan Steinmann for all the insightful scientific discussions and guidance, in particular, for the work on the surface state characterization.

I would like to thank Hang Hu who performed all the experiments on the isomerization and amination of isosorbide; some of those results have been reproduced in this manuscript for comparison of the experimental results with the theoretical ones. His help with the writing of the our first collaborative paper was invaluable.

Special gratitude to all my colleagues and other support staff of the lab, in particular, Dr. Tao Jiang, for helping me with the installation and use of Python libraries and other useful scripts to facilitate the execution of simulations, and Christian Melkonian for his help to keep our laptops running without any trouble.

Thanks to my family for their support and prayers, in particular my father who did not live long enough to read this manuscript or see me become the first PhD doctor of his family but who left no stone unturned in providing valuable education to his children. It was his support that made it possible for someone like me, coming from a very remote place in Pakistan, to one day come to Europe and study at prestigious institutes like ENS de Lyon and be a part of a rich scientific tradition.

Finally, I would like to thank Solvay Inc., Shanghai, for funding my PhD. work and also PSMN and Occigen centres for their generous computational resources.



Abstract

We have investigated heterocatalytic reactions of isosorbide (IS), a crucial platform molecule with industrial applications. Mainly, we have looked at the isomerization of IS to its less abundant isomers, isoidide and isomannide, with a special focus to understanding the indispensable role of hydrogen. The isomerization is a potential route in any reaction that involves dehydrogenation of IS, i.e. amination, and thus needs in depth understanding to aid in our attempts to valorize IS into other useful chemicals. The isomerization reaction takes place in the presence of aqueous solvent, up to 50 bar pressure of hydrogen and temperature as high as 200 °C using carbon-supported ruthenium catalyst. Using periodic density functional theory, we have investigated the potential energy surface for the isomerization of IS both in the absence and the presence of hydrogen. Our results indicate that a coverage of hydrogen on the catalyst surface plays an important role in destabilizing the otherwise very stable reaction intermediates thereby reducing the overall barriers involved in the reaction. As a second step, we have characterized the surface state of the catalyst under experimental conditions of temperature and pressure using ab initio atomistic thermodynamics. Our findings reveal that in the absence of any hydrogen, the surface can get (partially-)oxidized even by the mere presence of water. This further signifies a potential role of hydrogen as a protecting agent in the isomerization reaction. Finally, using kinetic modelling, we have investigated the amination reaction of IS with a view to understanding the potential poisoning of the catalyst surface by NH_x species.

Keywords: Density Functional Theory, heterogeneous catalysts, biomass, isosorbide, solvation



Contents

Acknowledgements	v
Abstract	vii
Table of Contents	ix
Introduction	1
References	3
1 Bibliographic study	5
1.1 Computational chemistry an indispensable tool in heterogeneous catalysis	7
1.2 Catalytic Sites	8
1.3 Gaseous Environment	10
1.4 Aqueous Environment	11
1.5 Conclusion	12
References	13
2 Methodology	19
2.1 Model of the catalyst	20
2.1.1 Supercell	20
2.2 Schrödinger Equation	23
2.3 Density Functional Theory	26
2.4 Thermodynamic Model	31
2.5 Solvation - MMsolv	33
2.6 Microkinetic Modelling	35
References	39
3 Isosorbide	43
I Isomerization	45
3.1 Introduction	47
3.2 Computational Details	50

Contents

3.3	Gas-Phase Geometry of Molecules	50
3.4	Mechanistic Investigation by Periodic DFT	51
3.4.1	Adsorption of isohexides	53
3.4.2	Free energy profile in the limit of a low H surface concentration	54
3.4.3	Rotation of MK and role of ring ethers	58
3.4.4	Free energy profile in presence of a high H ₂ pressure	59
3.5	Conclusion	73
II	Amination	75
3.6	Introduction	77
3.7	Computational Details	80
3.8	Results	81
3.8.1	Adsorption Structures	81
3.8.2	Free-energy profile	81
3.8.3	Kinetic Results	82
3.9	Conclusion	83
	References	85
4	Surface State of Ru catalysts	91
4.1	Introduction	92
4.2	Methodology - Ab-initio Thermodynamics	94
4.2.1	Solid Phase	96
4.2.2	Challenge of Phase Space	98
4.2.3	Gas Phase Reservoir	101
4.3	Computational Details	103
4.4	Results and Discussion	105
4.4.1	Single atom/molecule adsorption	105
4.4.2	Validation of MMSolv approach	105
4.4.3	Systematic adsorption of H and O	111
4.4.4	Full Phase Space: H/O/OH/H ₂ O	114
4.5	Conclusion	119
	References	121
	Conclusions and Outlook	125



Introduction

Modern society owes a great deal of its amenities and luxuries to the developments made in the field of catalysis. Is it because of catalysis that today our cars produce less and less toxic emissions; our supermarkets are always full of fresh food and we have a plethora of pharmaceuticals that keep us from getting sick. Almost all the industrial processes for the large scale production of fuels, chemicals and other commodities require a catalyst to be economically feasible. Catalysis thus lies at the heart of the modern economy. It is estimated that economic contribution of catalysis exceeds 35 % of the world GDP¹ and roughly 90 % of all chemicals, from fuels, pharmaceuticals, paints, cosmetics etc., require a catalyst for their production. This significance of catalysis was reflected in the decision of the Royal Swedish Academy of sciences to award the Nobel Prize in Chemistry for 2021 jointly to Benjamin List and David W.C. MacMillan for the development of asymmetric organocatalysis². In fact, many other aspects of catalysis have been recognized by the Nobel Prize committee over the years by honouring the works of W. Ostwald (1909); P. Sabatier (1912); K. Ziegler and G. Natta (1963); J.W. Cornforth (1975); W.S. Knowles, R. Noyori and K.B. Sharpless (2001); Y. Chauvin, R.H. Grubbs and R.R. Schrock (2005); and R.F. Heck, E.-i. Negishi and A. Suzuki (2010)³.

Catalysis is the science of speeding up a process by addition of a substance which itself is not consumed during the reaction. The catalyst binds with the reacting species to facilitate the breaking and making of the chemical bonds and eventually decouples unchanged from the products. In some cases, the catalyst actually makes the reaction happen and without it there is no transformation at all (Figure 1). Since any chemical or biological transformation is an activated process i.e. the starting species have to overcome an activation barrier before they can be converted into final products, catalyst achieves this feat by providing an alternative reaction pathway involving lower activation barriers such that more molecules have the energy to overcome this barrier and convert into final products. As such, catalyst does not alter the thermodynamic

outcome of a reaction, it merely changes the time to reach that outcome.

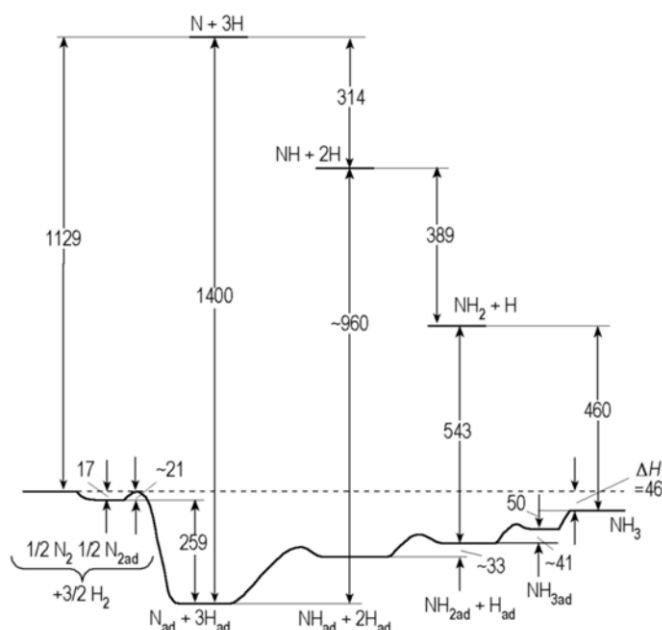


Figure 1: Schematic energy profile of the progress of ammonia synthesis on Fe (energies in kJ/mol). Without Fe catalyst, reaction is highly endothermic and thus impossible due to high activation energy of N_2 bond dissociation. Taken from ref. ⁴.

Use of solid, heterogeneous catalysts, mostly consisting of different metals or metal oxides, makes it easier for a post-reaction separation and subsequent reuse of the catalyst making them ideal for large-scale industrial applications. This characteristics of heterogeneous catalysts is desirable for their application in valorization of biomass which is deemed to replace the traditional fossil-based feedstock for the production of fuels and chemicals. Realization of novel and characterization of existing catalysts thus lies at the heart of a biobased economy with a greener environmental footprint.

Computational chemistry over the past two decades has matured into a sophisticated tool for the study of heterogeneous catalytic systems and has, therefore, paved the way not only for atomic-scale understanding of complex catalytic processes over existing catalysts but also for *in silico* prediction and realization of new and improved catalysts. The work performed during the course of this PhD involved use of computational tools for the study of industrially-relevant reactions of biomass-derived molecules on supported metal catalysts with a special focus to elucidating the role of particular reaction conditions and characterizing the surface state of the catalyst under those particular conditions.

In Chapter 1 we review the state of the art of computational chemistry, especially density functional theory, in reference to three major aspects of a heterogeneously catalyzed reaction namely active sites, gaseous environment and aqueous environment. In Chapter 2, we highlight the computational and thermodynamic models used to calculate the adsorption free energies of various species on solid, metallic surfaces. This is followed by Chapter 3 which concerns with the full theoretical investigation of the isomerization and amination of isosorbide on supported Ru/C catalyst. Lastly, Chapter 4 gives our results of the surface state characterization of supported-Ru catalysts in vapor or liquid water and under an external pressure of H₂.

Bibliography

- [1] *Industrial Catalysis*; John Wiley & Sons, Ltd, 2015; Chapter 17, pp 459–462.
- [2] Nobelprize.org, *The Nobel Prize in Chemistry 2021*. <https://www.nobelprize.org/prizes/chemistry/2021/summary/> [Accessed : November 9], 2021.
- [3] Nobelprize.org, *All Nobel Prizes in Chemistry*. <https://www.nobelprize.org/prizes/list/all-nobel-prizes-in-chemistry/> [Accessed : November 9], 2021.
- [4] Appl, M. *Ullmann's Encyclopedia of Industrial Chemistry*; John Wiley & Sons, Ltd, 2006; _eprint: https://onlinelibrary.wiley.com/doi/pdf/10.1002/14356007.a02_143.pub2.



1 Bibliographic study

Chapter 1. Bibliographic study

In the present chapter, we review the state of the art of computational theoretical chemistry in reference to biomass valorization using heterogeneous catalysis¹, in particular supported metal catalysts. Firstly, we introduce in a broader sense the field of computational chemistry which is rapidly transforming into an indispensable tool of investigation for chemists, surface and material scientists. We pose that the *first-principles* based computational studies have tried to tackle various questions of interest, at different length and time scales and to varying levels of accuracy, in heterogeneous catalysis over the past two decades²; and have proven helpful in rationalizing the experimentally observed trends of selectivity and reactivity by analyzing complex potential energy surfaces (PES) involving various different pathways; and utilizing the information provided by PES to study the underlying reaction kinetics.

To stay true to the general theme of the work performed during the preparation of this thesis, this review focuses on three key aspects of the heterogeneous catalysis where simulations have shown considerable potential as a valuable tool not only of rationalization but also of prediction: structure sensitivity i.e. effect of different catalytic sites on reaction outcome, modification of the catalytic activity and selectivity under external gaseous and/or aqueous environments (Figure Figure 1.1). We show that the latter two aspects can, in turn, add to the structure sensitivity problem either by modifying the surface state (active site) of the catalyst under *operando* conditions or through direct interaction with the reacting species and/or reaction intermediates and transition states.

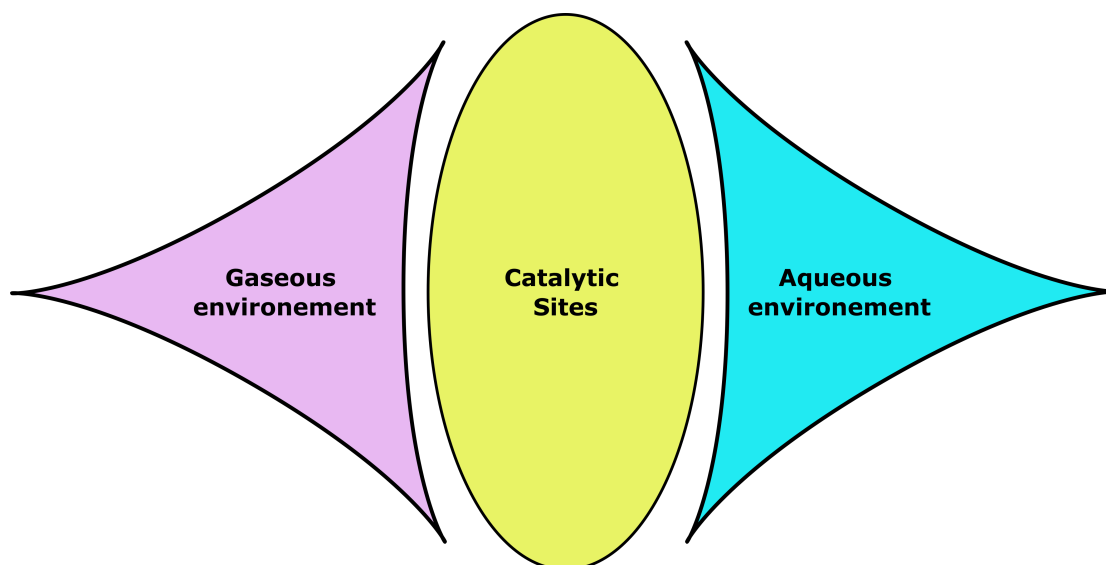


Figure 1.1: Three aspects of heterogeneous catalysis reviewed in this bibliographic study. Catalytic sites are prone to modification under gaseous or aqueous environments.

1.1 Computational chemistry an indispensable tool in heterogeneous catalysis

Computational chemistry concerns mainly with determination of electronic energy of a collection of atoms based on quantum mechanical principles subjected to varying degree of approximation. The electronic system of interest in heterogeneous catalysis is generally a solid catalyst interacting with reacting species in gas or liquid phase. Such a system can undergo transformations at different length and time scales (Figure 1.2); and a single overarching computational technique is unable, and essentially impossible, to describe all the various phenomena that take place at those length and time scales. This limitation is easily overcome by constructing a multiscale approach comprising of many different computational paradigms starting from atomistic, nanoscale description of individual chemical bonds (point **a** in Figure 1.2) all the way up to the macroscale description of heat and mass flow at the level of a full catalytic reactor (point **d** in Figure 1.2). Computational chemistry concerns itself mainly with the first two stages of the multiscale approach depicted in Figure 1.2; and density functional theory (DFT) has become the workhorse of all modern computational studies of heterogeneous catalytic systems due to its excellent cost-efficiency balance^{3–12}.

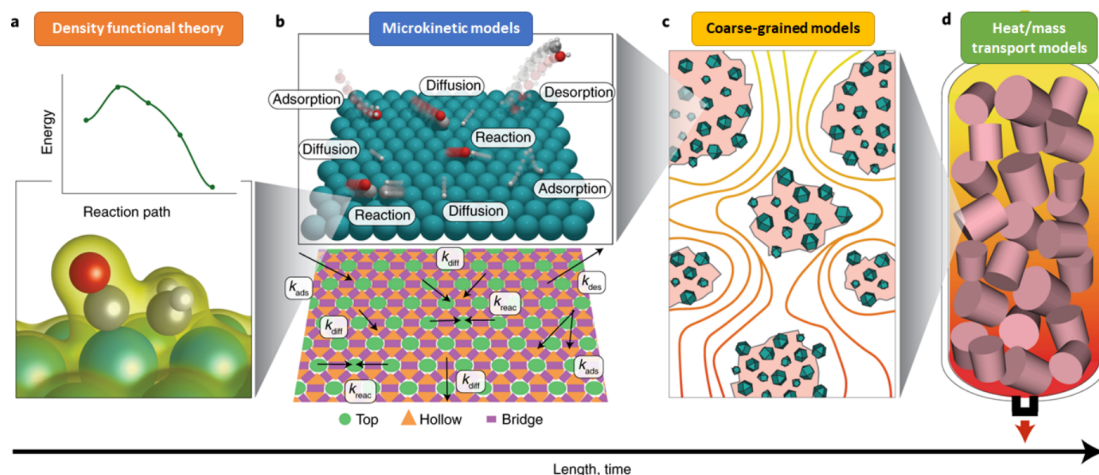


Figure 1.2: An illustration of different length and time scales involved in a heterogeneously-catalyzed reaction. Various theoretical and computational models combined in a multiscale approach are required for a bottom-up realization of a full catalytic process. Taken from ref¹³.

At the microscopic scale, DFT is employed for the study of elementary reaction steps and provides a reasonably accurate, predictive description of binding/adsorption of

reacting species to the metallic surfaces¹⁴. Assuming a particular mechanism, energy profiles can be constructed for a full reaction pathway by determining the most stable configurations of likely intermediates and transition states^{15;16}. The reaction energy profiles are, in turn, used to extract activation energies and elementary rate constants which are given as input to a microkinetic model, either of mean-field nature^{16–18} or kinetic Monte-Carlo^{19–21}, to study the interplay between different elementary reaction steps at given conditions of temperature, pressure and concentrations of reacting species.

One special achievement of DFT-aided computational studies of heterogeneous catalysts is the discovery of so called *scaling relations* which are empirical correlations between the binding energies of a wide range of catalytic reaction intermediates on a range of metallic surfaces^{22;23}. The use of these *scaling relations* have made it possible to do *in silico*, high-throughput screening of potential catalytic systems by rapidly recognizing the active sites and mechanisms^{24;25}.

However, the molecules and reaction conditions involved in biomass valorization are quite complex and *scaling relations* offer no help. One has to resort to brute-force investigation of the reaction profiles of these complex molecules on metallic surfaces which are often subjected to severe external conditions of temperature and pressure making it hard to characterize the relevant active sites and their potential modification under *operando* conditions. This difficulty faced by quantum chemistry is reflected in three main themes which are individually discussed in the following.

1.2 Catalytic Sites

Determination of the active sites for elementary reactions steps involved in a catalytic cycle is of paramount importance and a variation of the active sites could potentially result in a different reaction outcome (Figure 1.3)^{26–28}. In principle, active sites can be located on a single-crystal, compact plane; on the edges of the nanoparticle (NP) or even at the triple phase boundary with the support. This presents computational chemists with the difficulty of having to choose a proper model for the catalytic system which best represents the experimental reality and is computationally tractable at the same time. This predicament is best represented visually by Figure 1.4 which highlights the model reductionism often practiced in computational catalysis, mainly to overcome the prohibitive computational cost of having to treat a full catalytic system.

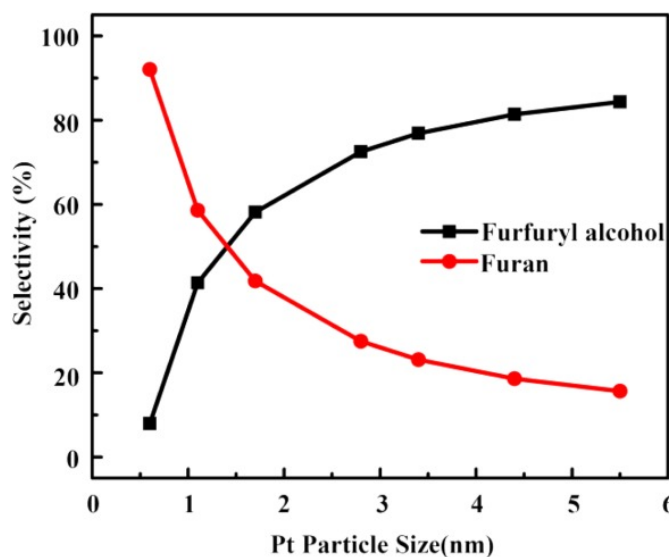


Figure 1.3: The predicted selectivity as a function of the Pt nanoparticle size at $T = 473\text{ K}$ and $p_{\text{H}_2} = 93\text{ kPa}$ ($p_{\text{C}_4\text{H}_3(\text{CO})\text{O}} = 9.3\text{ kPa}$). Reprinted from ref.²⁶.

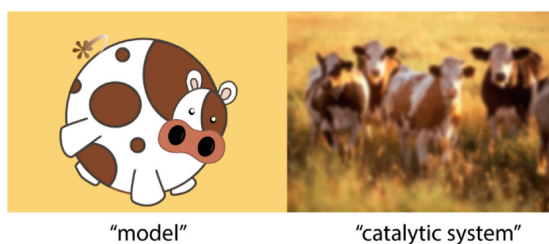


Figure 1.4: Illustrative example of excessive reductionism in modeling. Despite being in a partial agreement (e.g., spectral features, patterns, and size) with the "experiment", the model may not be adequate for the description of the key details within the catalytic system and its overall function. Reprinted from ref.²⁹.

Typical models employed in computational heterogeneous catalysis are so called *slab model* to represent single-crystal surfaces, often in combination with periodic boundary conditions; isolated cluster models to represent NPs of various sizes and supported-clusters to represent the experimentally realistic supported NP catalysts. The level of accuracy provided by each model is also limited by the underlying level of theory employed and, hence, an important task of the computational chemists involved in heterogeneous catalysis research is to choose a combination of model-method that best describes the salient features of their system keeping in view the computational prowess at their disposal²⁹.

1.3 Gaseous Environment

Reactions involving biomass and biomass-derived molecules often require a constant flow of a gaseous environment, either an inert gas like Ar, N₂ or more reactive H₂. For example isomerization of isosorbide on solid, supported Ru catalysts is an industrially important reaction that requires very high pressure (~ 10-50 bar) of H₂; without H₂ there is no reaction at all, although, H₂ is not required stoichiometrically³⁰.

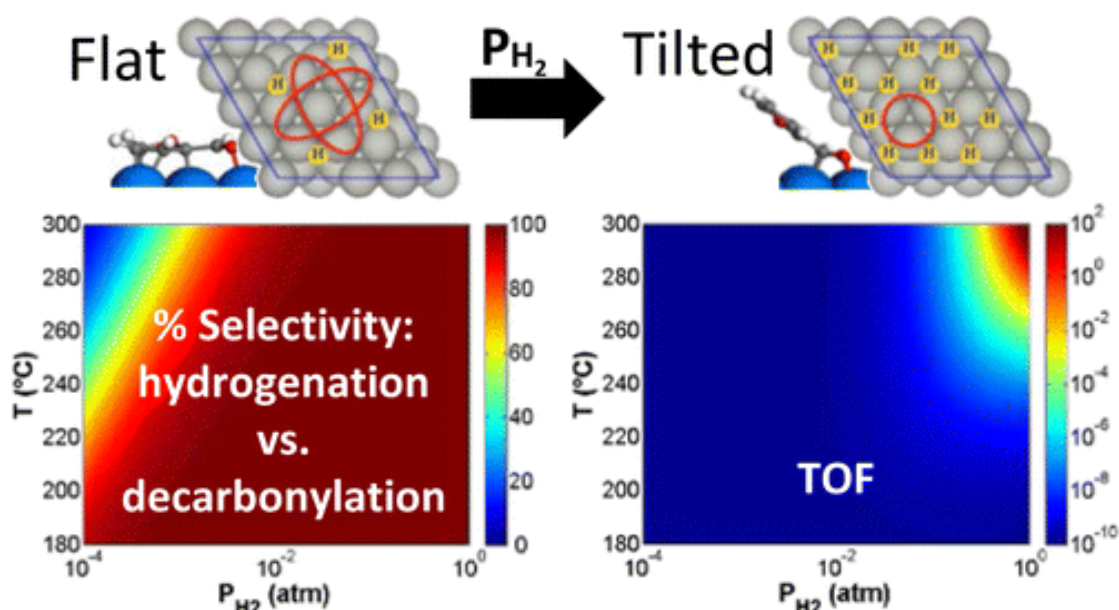


Figure 1.5: Coverage induced conformational change in the adsorption geometry of furfural leading to different reaction mechanism at higher pressure and thus a different product. Reprinted from ref³¹.

DFT-aided computational studies have been able to tackle this problem of external pressure in terms of coadsorption of species on the surface at coverages corresponding to the macroscopic thermodynamic descriptors (temperature, pressure) of the surrounding gas phase environment. Vlachos et al. showed that a pressure-induced coverage of H species on Pd(111) surface modifies the adsorption conformation of furfural leading to either furan as main product (low H coverage, flat adsorption conformation) or furfuryl alcohol as the major product (high H coverage, tilted conformation) (Figure 1.5)³¹. Such pressure induced conformational change in the adsorption geometry is also observed for alanine on Ni(111) surface³². Sarah et al. have also investigated the coadsorption of butadiene with H for hydrogenation reaction and highlighted the limitations of applied exchange-correlation functionals in correctly predicting the stability of cohabitation state compared to the state where surface is

fully covered with H and butadiene is in gas phase³³.

Furthermore, to study the potential impact of external pressure on the surface topology of the catalyst and, in turn, on catalytic sites, *ab-initio* atomistic thermodynamics is often employed to relate the static, zero-point electronic energies obtained from DFT with the dynamic, gaseous environment around the solid catalyst and the determine the most stable phase at a give temperature and pressure³⁴. The biplanar to cuboctahedral morphology change of Pt₁₃ clusters supported on γ -Al₂O₃ as a function of H₂ pressure is an example of the power of computational chemistry in rationalizing and predicting the effect of external environment on the structure sensitivity of the catalyst³⁵.

1.4 Aqueous Environment

Due to its enhanced tendency to solubilize biomass feedstock, metal-supported catalysts are often employed in combination with water for upgrading the biobased chemical. In certain cases, e.g. for supported-Ru catalysts³⁶, water is found to significantly increase the activity of the metal catalysts. This puzzling aspect requires a clear understanding of the interaction of water with the metallic surfaces as well its potential interaction with the reaction species.

Continuum models like PCM³⁷ are increasingly being used to model the reactions at the metal/water interface and give valuable insight when charger separation is involved as is the case in electrocatalysis³⁸. The PCM model can be combined with microsolvation to include direct solvation effects^{39–41}. Ab-initio molecular-dynamics (AIMD), combined with appropriate enhanced sampling schemes like thermodynamic integration⁴² or metadynamics⁴³, seems an appealing option but the computational cost for such explicit water models remains prohibitive. Our research group has recently developed a QM/MM explicit solvent approach based on empirical metal/water force-fields t account for the structural changes in adsorption energies upon solvation⁴². We have used a modified version of this approach to look at the differences of solvation enthalpies between different adsorption geometries. It is further explained in Chapters 2 and 4.

1.5 Conclusion

We have established that DFT is an excellent elucidation, and sometimes even predictive, tool for the study of heterogeneous catalytic systems. Using appropriate thermodynamic and kinetic models, the information obtained from static DFT calculations can be related with the experimental conditions of temperature and pressure. The work presented in this thesis made extensive use of DFT along with microkinetic modelling and ab-initio thermodynamics to (i) build reaction profiles for the isomerization of isosorbide with and without coadsorbed H atoms on supported Ru/C catalyst (ii) study the potential poisoning of the Ru/C catalyst with NH_x species during amination of isosorbide (iii) characterized the surface state of the supported-Ru catalysts in vapor or liquid water and under a pressure of H_2 .

Bibliography

- [1] Besson, M.; Gallezot, P.; Pinel, C. Conversion of Biomass into Chemicals over Metal Catalysts. *Chemical reviews* **2013**, 114.
- [2] van Santen, R.; Sautet, P. *Computational Methods in Catalysis and Materials Science: An Introduction for Scientists and Engineers (English Edition)*, 1st ed.; Wiley-VCH, 2015.
- [3] Deng, J.; Li, H.; Xiao, J.; Tu, Y.; Deng, D.; Yang, H.; Tian, H.; Li, J.; Ren, P.; Bao, X. Triggering the electrocatalytic hydrogen evolution activity of the inert two-dimensional MoS₂ surface via single-atom metal doping. *Energy Environ. Sci.* **2015**, 8, 1594–1601, Publisher: The Royal Society of Chemistry.
- [4] Hellman, A. *et al.* Predicting Catalysis: Understanding Ammonia Synthesis from First-Principles Calculations. *The Journal of Physical Chemistry B* **2006**, 110, 17719–17735, Publisher: American Chemical Society.
- [5] Honkala, K.; Laasonen, K. Oxygen Molecule Dissociation on the Al(111) Surface. *Phys. Rev. Lett.* **2000**, 84, 705–708, Publisher: American Physical Society.
- [6] Kerber, T.; Sierka, M.; Sauer, J. Application of semiempirical long-range dispersion corrections to periodic systems in density functional theory. *Journal of Computational Chemistry* **2008**, 29, 2088–2097, Publisher: John Wiley & Sons, Ltd.
- [7] Gao, G.; Jiao, Y.; Wacławik, E. R.; Du, A. Single Atom (Pd/Pt) Supported on Graphitic Carbon Nitride as an Efficient Photocatalyst for Visible-Light Reduction of Carbon Dioxide. *Journal of the American Chemical Society* **2016**, 138, 6292–6297, Publisher: American Chemical Society.
- [8] Chun, H.-J.; Apaja, V.; Clayborne, A.; Honkala, K.; Greeley, J. Atomistic Insights into Nitrogen-Cycle Electrochemistry: A Combined DFT and Kinetic Monte Carlo Analysis of NO Electrochemical Reduction on Pt(100). *ACS Catalysis* **2017**, 7, 3869–3882, Publisher: American Chemical Society.
- [9] Rosen, J.; Hutchings, G. S.; Lu, Q.; Rivera, S.; Zhou, Y.; Vlachos, D. G.; Jiao, F. Mechanistic Insights into the Electrochemical Reduction of CO₂ to CO on Nanostructured Ag Surfaces. *ACS Catalysis* **2015**, 5, 4293–4299, Publisher: American Chemical Society.

Chapter 1. Bibliographic study

- [10] Norskov, J.; Scheffler, M.; Toulhoat, H. Density functional theory in surface science and heterogeneous catalysis. *MRS BULLETIN* **2006**, *31*, 669–674.
- [11] Neyman, K.; Illas, F. Theoretical aspects of heterogeneous catalysis: Applications of density functional methods. *CATALYSIS TODAY* **2005**, *105*, 2–16.
- [12] Rosen, A. S.; Notestein, J. M.; Snurr, R. Q. Identifying promising metal-organic frameworks for heterogeneous catalysis via high-throughput periodic density functional theory. *JOURNAL OF COMPUTATIONAL CHEMISTRY* **2019**, *40*, 1305–1318.
- [13] Chen, B. W. J.; Xu, L.; Mavrikakis, M. Computational Methods in Heterogeneous Catalysis. *Chemical Reviews* **2021**, *121*, 1007–1048, PMID: 33350813.
- [14] Mazheika, A.; Levchenko, S. V. Ni Substitutional Defects in Bulk and at the (001) Surface of MgO from First-Principles Calculations. *The Journal of Physical Chemistry C* **2016**, *120*, 26934–26944, Publisher: American Chemical Society.
- [15] Liu, Z.; Hu, P. CO oxidation and NO reduction on metal surfaces: density functional theory investigations. *TOPICS IN CATALYSIS* **2004**, *28*, 71–78.
- [16] Honkala K.; Hellman A.; Remediakis I. N.; Logadottir A.; Carlsson A.; Dahl S.; Christensen C. H.; Nørskov J. K., Ammonia Synthesis from First-Principles Calculations. *Science* **2005**, *307*, 555–558, Publisher: American Association for the Advancement of Science.
- [17] Xu, D.; Wu, P.; Yang, B. Essential Role of Water in the Autocatalysis Behavior of Methanol Synthesis from CO₂ Hydrogenation on Cu: A Combined DFT and Microkinetic Modeling Study. *The Journal of Physical Chemistry C* **2019**, *123*, 8959–8966, Publisher: American Chemical Society.
- [18] Pilot, I. A. W.; van Santen, R. A.; Hensen, E. J. M. The Optimally Performing Fischer–Tropsch Catalyst. *Angewandte Chemie International Edition* **2014**, *53*, 12746–12750, Publisher: John Wiley & Sons, Ltd.
- [19] Chatterjee, A.; Vlachos, D. G. An overview of spatial microscopic and accelerated kinetic Monte Carlo methods. *Journal of Computer-Aided Materials Design* **2007**, *14*, 253–308.
- [20] Stamatakis, M.; Chen, Y.; Vlachos, D. G. First-Principles-Based Kinetic Monte Carlo Simulation of the Structure Sensitivity of the Water–Gas Shift Reaction on

- Platinum Surfaces. *The Journal of Physical Chemistry C* **2011**, 115, 24750–24762, Publisher: American Chemical Society.
- [21] Sendner, C.; Sakong, S.; Groß, A. Kinetic Monte Carlo simulations of the partial oxidation of methanol on oxygen-covered Cu(110). *Surface Science* **2006**, 600, 3258–3265.
- [22] Greeley, J. Theoretical Heterogeneous Catalysis: Scaling Relationships and Computational Catalyst Design. *Annual Review of Chemical and Biomolecular Engineering* **2016**, 7, 605–635.
- [23] Calle-Vallejo, F.; Loffreda, D.; Koper, M. T. M.; Sautet, P. Introducing structural sensitivity into adsorption–energy scaling relations by means of coordination numbers. *Nature Chemistry* **2015**, 7, 403–410.
- [24] Vojvodic, A.; Nørskov, J. K. New design paradigm for heterogeneous catalysts. *National Science Review* **2015**, 2, 140–143.
- [25] Xu, H.; Cheng, D. First-principles-aided thermodynamic modeling of transition-metal heterogeneous catalysts: A review. *Green Energy & Environment* **2020**, 5, 286–302.
- [26] Cai, Q.-X.; Wang, J.-G.; Wang, Y.-G.; Mei, D. Mechanistic insights into the structure-dependent selectivity of catalytic furfural conversion on platinum catalysts. *AIChE Journal* **2015**, 61, 3812–3824, Publisher: John Wiley & Sons, Ltd.
- [27] Bray, J. M.; Schneider, W. F. First-Principles Analysis of Structure Sensitivity in NO Oxidation on Pt. *ACS Catalysis* **2015**, 5, 1087–1099, Publisher: American Chemical Society.
- [28] Zhang, B.-Y.; Su, H.-Y.; Liu, J.-X.; Li, W.-X. Interplay Between Site Activity and Density of BCC Iron for Ammonia Synthesis Based on First-Principles Theory. *ChemCatChem* **2019**, 11, 1928–1934, Publisher: John Wiley & Sons, Ltd.
- [29] Pidko, E. A. Toward the Balance between the Reductionist and Systems Approaches in Computational Catalysis: Model versus Method Accuracy for the Description of Catalytic Systems. *ACS Catalysis* **2017**, 7, 4230–4234, Publisher: American Chemical Society.

- [30] Engel, R. V.; Niemeier, J.; Fink, A.; Rose, M. Unravelling the Mechanism of the Ru/C-Catalysed Isohexide and Ether Isomerization by Hydrogen Isotope Exchange. *Advanced Synthesis & Catalysis* **2018**, 360, 2358–2363, Publisher: John Wiley & Sons, Ltd.
- [31] Wang, S.; Vorotnikov, V.; Vlachos, D. G. Coverage-Induced Conformational Effects on Activity and Selectivity: Hydrogenation and Decarbonylation of Furfural on Pd(111). *ACS Catalysis* **2015**, 5, 104–112, Publisher: American Chemical Society.
- [32] Nicklin, R. E. J.; Shavorskiy, A.; Aksoy Akgul, E.; Liu, Z.; Bennett, R. A.; Sacchi, M.; Held, G. “Pop-On and Pop-Off” Surface Chemistry of Alanine on Ni{111} under Elevated Hydrogen Pressures. *The Journal of Physical Chemistry C* **2018**, 122, 7720–7730, Publisher: American Chemical Society.
- [33] Gautier, S.; Sautet, P. Coadsorption of Butadiene and Hydrogen on the (111) Surfaces of Pt and Pt₂Sn Surface Alloy: Understanding the Cohabitation from First-Principles Calculations. *The Journal of Physical Chemistry C* **2017**, 121, 25152–25163, Publisher: American Chemical Society.
- [34] Reuter, K.; Scheffler, M. Composition, structure, and stability of RuO₂(110) as a function of oxygen pressure. *Phys. Rev. B* **2001**, 65, 035406, Publisher: American Physical Society.
- [35] Mager-Maury, C.; Bonnard, G.; Chizallet, C.; Sautet, P.; Raybaud, P. H₂-Induced Reconstruction of Supported Pt Clusters: Metal–Support Interaction versus Surface Hydride. *ChemCatChem* **2011**, 3, 200–207, Publisher: John Wiley & Sons, Ltd.
- [36] Michel, C.; Gallezot, P. Why Is Ruthenium an Efficient Catalyst for the Aqueous-Phase Hydrogenation of Biosourced Carbonyl Compounds? *ACS Catalysis* **2015**, 5, 150529175450002.
- [37] Mathew, K.; Sundararaman, R.; Letchworth-Weaver, K.; Arias, T. A.; Hennig, R. G. Implicit solvation model for density-functional study of nanocrystal surfaces and reaction pathways. *The Journal of Chemical Physics* **2014**, 140, 084106, Publisher: American Institute of Physics.
- [38] Steinmann, S. N.; Michel, C.; Schwiedernoch, R.; Filhol, J.-S.; Sautet, P. Modeling the HCOOH/CO₂ Electrocatalytic Reaction: When Details Are Key. *ChemPhysChem* **2015**, 16, 2307–2311, Publisher: John Wiley & Sons, Ltd.

-
- [39] Michel, C.; Zaffran, J.; Ruppert, A. M.; Matras-Michalska, J.; Jędrzejczyk, M.; Grams, J.; Sautet, P. Role of water in metal catalyst performance for ketone hydrogenation: a joint experimental and theoretical study on levulinic acid conversion into gamma-valerolactone. *Chem. Commun.* **2014**, *50*, 12450–12453, Publisher: The Royal Society of Chemistry.
- [40] Schweitzer, B.; Steinmann, S. N.; Michel, C. Can microsolvation effects be estimated from vacuum computations? A case-study of alcohol decomposition at the H₂O/Pt(111) interface. *Phys. Chem. Chem. Phys.* **2019**, *21*, 5368–5377, Publisher: The Royal Society of Chemistry.
- [41] Kelly, C.; Cramer, C.; Truhlar, D. Adding explicit solvent molecules to continuum solvent calculations for the calculation of aqueous acid dissociation constants. *JOURNAL OF PHYSICAL CHEMISTRY A* **2006**, *110*, 2493–2499, Place: 1155 16TH ST, NW, WASHINGTON, DC 20036 USA Publisher: AMER CHEMICAL SOC Type: Review.
- [42] Clabaut, P.; Schweitzer, B.; Götz, A. W.; Michel, C.; Steinmann, S. N. Solvation Free Energies and Adsorption Energies at the Metal/Water Interface from Hybrid Quantum-Mechanical/Molecular Mechanics Simulations. *Journal of Chemical Theory and Computation* **2020**, *16*, 6539–6549, PMID: 32931268.
- [43] Réocreux, R.; Girel, E.; Clabaut, P.; Tuel, A.; Besson, M.; Chaumonnot, A.; Cabiac, A.; Sautet, P.; Michel, C. Reactivity of shape-controlled crystals and metadynamics simulations locate the weak spots of alumina in water. *Nature Communications* **2019**, *10*, 3139.



2 Methodology

“The fundamental laws necessary for the mathematical treatment of a large part of physics and the whole of chemistry are thus completely known, and the difficulty lies only in the fact that application of these laws leads to equations that are too complex to be solved.”

Paul Dirac

In this Ph.D work our goal is to study (i) the adsorption of different atomic and molecular species on metallic catalyst surfaces and (ii) the reactivity of industrially important, biobased molecules on those surfaces by monitoring the formation and breaking of relevant chemical bonds during the course of a catalyzed reaction. This goal can be achieved by solving the underlying many-body electronic structure problem using advanced techniques of quantum chemistry to obtain the Gibbs free energy of adsorption of various reaction intermediates and transition states. In this chapter we outline the models and methodologies employed during the course of this work. In the first section, we introduce the model adopted to simulate a catalyst surface. It is followed by a brief overview of the *first-principles* quantum mechanical formalism, mainly Density Functional Theory (DFT), which was used to obtain the electronic, and wherever applicable, the enthalpic and entropic contributions to the total energy of the model system. The third section gives details of the thermodynamic model necessary to convert the DFT energies into useful thermodynamic quantities i.e. Gibbs free energy. Fourth section details a novel approach to explicitly take into account solvation effects on the adsorption of different species. Finally, we end the chapter with a brief description of a simplified microkinetic model based on DFT Gibbs free energies.

2.1 Model of the catalyst

Realistic metal-supported, heterogeneous catalysts are generally composed of an active metal part in the shape of nanoparticles (NP) containing many thousands of atoms dispersed on a support material, typically oxides or activated carbon¹ (Figure 2.1). Notwithstanding the significant increase in the computational prowess of modern-day computers² and developments made in the underlying theory and algorithms^{3;4}, systems of such large sizes still inaccessible to be treated by contemporary high-precision, quantum-mechanical techniques owing to their prohibitively high computational cost. This difficulty can be overcome by observing that on fairly large-sized NPs ($> 3\text{nm}$) supported on inert materials (activated carbon), the active sites can be modeled using single-crystal planes representing the individual exposed facets on the NP surface. This has led to the development of so called *slab model* which has become quite ubiquitous in the modelling of heterogeneous catalysis using *first-principles* calculations^{5;6}. Unless stated otherwise, the same *slab model* was employed for the computational studies reported in this thesis.

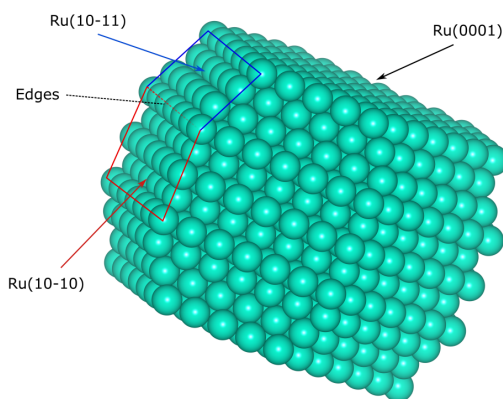


Figure 2.1: A Ru NP containing 1175 Ru atoms and exposing three major facets on its surface. A realistic NP can expose various facets and terminations leading to many different edge sites thereby further increasing the complexity. Prepared with ASE package⁷.

2.1.1 Supercell

The single-crystal planes exposed on a catalytic-NP surface can be of varying lattice symmetry and corrugation. One could easily establish a smallest unit, called primitive unit cell and often defined in more than one ways, which when repeated in two dimensions generates the entire planar lattice. The Figure 2.2 highlights the primitive unit cell (solid, black line, 1×1) and the corresponding lattice vectors **a**, **b** for the high symmetry, closed-pack, hexagonal lattice. The primitive unit cell for various crystal planes that are exposed on metal-NPs is usually too small to study the adsorption of molecular species, especially large molecules. This issue can

be resolved by constructing a so called *supercell* obtained by simply extending the primitive unit cell along the planar lattice vectors. Figure 2.2 shows the p(2x2) and p(3x3) *supercells* for hexagonal, closed-pack lattice constructed by multiplying the primitive lattice vectors by 2 and 3, respectively, in each planar direction (here p stands for primitive). Interestingly, it is also possible to work with *supercells* constructed from non-primitive unit cells. The purple lines in Figure 2.2 show a non-primitive unit cell with new lattice vectors $\sqrt{3}$ times the original lattice vectors after a rotation of 30° ($R30^\circ (\sqrt{3} \times \sqrt{3})$). Such non-primitive, fractional unit cells, and *supercells* based on them, are sometimes better suited to mimic the experimentally observed adsorption behavior of species on metallic surfaces, e.g. the ice-like bilayer structures observed on hexagonal, closed-pack Ru(0001) surface⁸. The final choice of the *supercell* size is generally dictated by the need to minimize lateral interactions between periodic copies of the adsorbing species and the computational resources at hand: a larger *supercell* would require simulating increasingly large number of atoms.

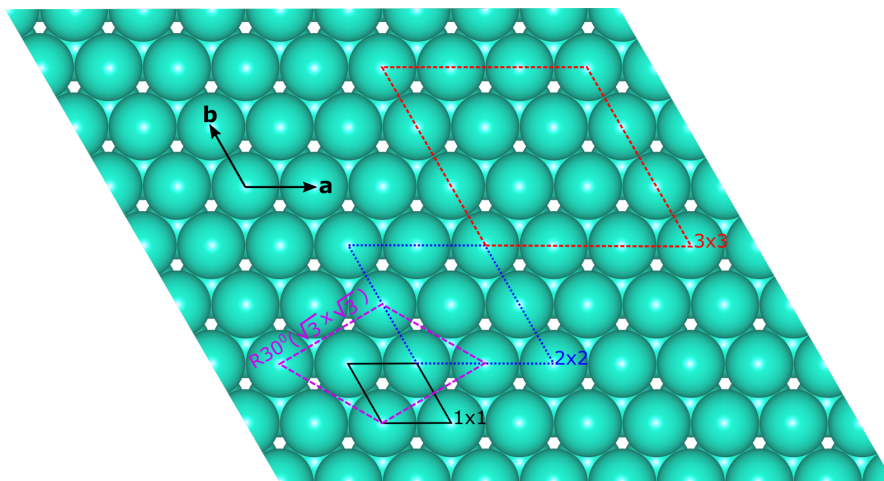


Figure 2.2: Illustration of different *supercell* sizes that could be used to simulate adsorption of molecules on metallic surface. The primitive unit cell shown in solid-black line can be extended in any lattice direction to achieve the desired simulation cell. Purple lines indicate a non-primitive unit cell with fractional multiple of primitive lattice vectors **a**, **b** rotated by 30° .

Apart from the lateral size, two other important factors need careful attention in the construction of a reasonable *supercell* representing a surface termination exposed on the catalyst NP. Firstly, one has to choose a suitable thickness of the *slab* for a given planar surface. This is often not straightforward to guess *a-priori* and convergence tests of adsorption energy of some representative species, or more generally surface energies⁹, against various simulation parameters (k-point, cutoff etc.) could be performed to get a *slab* thickness that gives best compromise between accuracy and efficiency. Secondly, a large enough region of vacuum must be introduced in the direction normal to the *slab* to minimize the interactions of the periodic copies of the *slab* in that direction and to essentially simulate a two-dimensional planar surface. Convergence tests could also be performed to choose a minimum length of

Chapter 2. Methodology

the vacuum region, although, one can get away by simply setting a very high value (≥ 15 Å). Figure 2.3 shows a detailed picture of the *slab model* adopted including the *supercell* size, the thickness of the *slab* and the vacuum added in the direction normal to the plane of the *slab*.

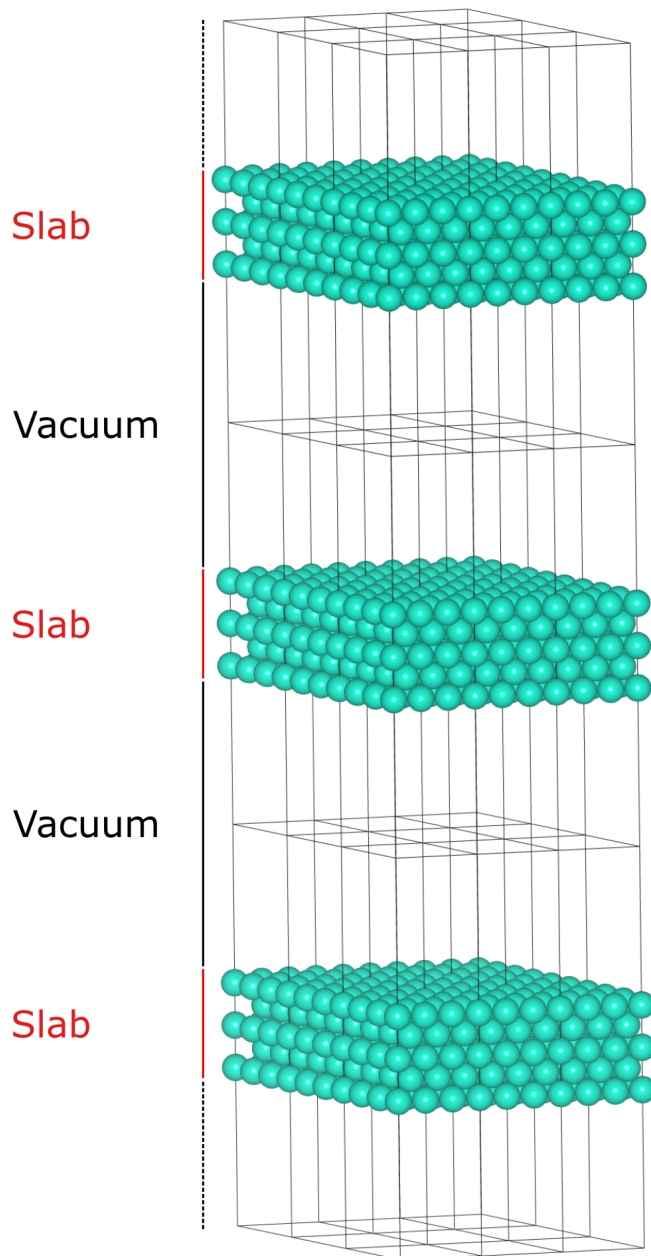


Figure 2.3: Representation of the *slab model* adopted to model the Ru(0001) facet exposed on the NP (Figure 2.1). The simulating unit was a $p(3 \times 3)$ *supercell* containing 5 layers of closed-packed Ru atoms. The *slab* is periodic in all three directions, however, vacuum was added in normal direction to minimize the interactions in that direction thereby simulating a potentially two-dimensional planar surface.

2.2 Schrödinger Equation

After setting up the model for the catalyst surface in the previous section, next challenge for a computational chemist is to solve the underlying many-body electronic structure problem involving interactions of various kinds to a reasonable accuracy. This is achieved, in principle exactly, by a solution of the non-relativistic, time-independent Schrödinger equation which can be compactly written as¹⁰

$$H\Psi = E\Psi, \quad (2.1)$$

where H is the Hamiltonian (total-energy operator) containing all the relevant energetic interactions involved in the system; E is the total energy of the system including electronic, translational, vibrational and rotational contributions and Ψ is the wavefunction of the system. For a molecule of N_{nu} nuclei and N_{el} electrons, the Hamiltonian can be broken down into terms representing the individual one and many-body interactions

$$H = T_N + T_e + V_{NN} + V_{Ne} + V_{ee}, \quad (2.2)$$

where the first term is the kinetic energy of each nuclei; the second term is the kinetic energy of individual electron; the third term is the repulsive Coulomb interaction between positively charged nuclei; fourth term accounts for the attractive Coulomb interaction between an electron and a nucleus and the final term gives the repulsive electron-electron interaction which is also of Coulomb nature. Following the atomic units, the individual terms can further be expressed as

$$\begin{aligned} T_N &= -\frac{1}{2} \sum_I^{N_{nu}} \frac{\nabla_I^2}{M_I}, \\ T_e &= -\frac{1}{2} \sum_i^{N_{el}} \nabla_i^2, \\ V_{NN} &= \sum_I^{N_{nu}} \sum_{J>I}^{N_{nu}} \frac{Z_I Z_J}{R_{IJ}}, \\ V_{Ne} &= -\sum_J^{N_{nu}} \sum_i^{N_{el}} \frac{Z_J}{R_{iJ}} \equiv \sum_i^{N_{el}} v_i, \\ V_{ee} &= \sum_i^{N_{el}} \sum_j^{N_{el}} \frac{1}{r_{ij}}, \end{aligned} \quad (2.3)$$

where ∇^2 is the Laplacian operator; Z_I is the charge on nuclei I ; R_{IJ} is the distance between nuclei I and J ; R_{iJ} is the distance between electron i and nucleus J and r_{ij} is the distance between two electrons i, j . A closer look at the expressions for different interactions in Eq. 2.3 reveals that the two kinetic energy terms and V_{Ne} are all one body interactions and can

Chapter 2. Methodology

be handled easily. In particular, V_{Ne} can be seen as each electron in the system feeling a collective attractive force towards all the nuclei in the system: v_i can be viewed as an external potential acting on electron i . However, the two-body terms, V_{NN} and especially V_{ee} , preclude a straightforward solution to Eq. 2.1 and thus require further treatment through various approximations.

Born-Oppenheimer Approximation

Born-Oppenheimer (BO) approximation usually serves as the first step towards solving Eq. 2.1 and is based on the recognition that electrons and nuclei have very different masses and thereby different timescales of their motion. Since mass of a nucleus is generally much higher than the mass of an electron, it can be assumed that electrons move instantaneously compared to the motion of the nuclei. This allows for a separation of variables and the total wavefunction of the system can then be written as product of an electronic and a nuclear part

$$\Psi_{total} = \Psi_{electronic} \Psi_{nuclear} \quad (2.4)$$

The approximation is often applied in two steps where first nuclei are fixed to specific positions ($T_{NN} = 0$) and electronic wavefunction is solved for a potential of fixed nuclei,

$$H = H_e + T_{NN} \quad (2.5)$$

where the H_e can be given as

$$H_e = -\frac{1}{2} \sum_i^{N_{el}} \nabla_i^2 + \sum_i^{N_{el}} v_i + \sum_I^{N_{nu}} \sum_{J>I}^{N_{nu}} \frac{Z_I Z_J}{R_{IJ}} + \sum_i^{N_{el}} \sum_{j>i}^{N_{el}} \frac{1}{r_{ij}} \quad (2.6)$$

Eq. 2.6 contains only the electronic degrees of freedom (the V_{NN} term involving repulsive interaction between nuclei just shifts the total energy but doesn't affect the overall conclusion) and the positions of nuclei appear just as a parameter leading to the following eigenvalue problem,

$$H_e \psi(\mathbf{r}; \mathbf{R}) = E_e(\mathbf{R}) \psi(\mathbf{r}; \mathbf{R}) \quad (2.7)$$

where $\mathbf{r}(\mathbf{R})$ represents positions of all the electrons(nuclei) and $\psi(\mathbf{r}; \mathbf{R})$ is the electronic wavefunction with a parametric dependence (signified by the semicolon) on the position of the nuclei. Solving the Eq. 2.6 leads to a potential energy surface, $E_e(\mathbf{R})$, which is used in the second step to evolve the nuclear degrees of motion along with nuclear kinetic energy part,

$$[T_{NN} + E_e(\mathbf{R})] \Phi(\mathbf{R}) = E \Phi(\mathbf{R}) \quad (2.8)$$

where $\Phi(\mathbf{R})$ is the nuclear wavefunction and can be further broken down into contributions involving translations, rotations and vibrations and E is the total energy of the molecular system including electronic, translational, vibrational and rotational components.

Although BO approximation provides an excellent starting point to solve the Eq. 2.1 by allowing a separation of electronic and nuclear degrees of freedom, it is still difficult to solve Eq. 2.7 exactly mainly because of the last term in Eq. 2.6 representing Columbic electron-electron repulsion. This term prohibits further separation of a complicated many-electronic problem into many simpler, one-electronic problems. Therefore, approximate solutions to Eq. 2.7 are sought which come in two major flavors: Hartree-Fock (HF) theory and the post-HF methods which improve upon HF formalism; and Density Functional Theory (DFT).

Post-HF methods require no *a-priori* parametrization and are found to be most accurate to study chemical problems, however, their computational cost scales unfavorably - $\mathcal{O}(N^4)$ for HF; $\mathcal{O}(N^5)$ for MP2; $\mathcal{O}(N^7)$ for CCSD(T) where N is some measure of system size i.e. number of electrons - with the system size limiting their use to only very small molecular systems. Besides, post-HF methods pose greater challenge in terms of their practical implementation to extended, periodic systems, especially infinite (metallic)surface slabs (2D) and crystals (3D)^{11;12}.

DFT on the other hand offers a unique compromise of accuracy and computational efficiency to tackle systems of reasonable chemical complexity and, therefore, serves as the workhorse of most of the modern computational chemistry investigations especially those in heterogeneous catalysis^{13;14}. Overall, it is customary to refer to both HF/post-HF and DFT as *ab-initio* or *first-principles* methods.

Hartree-Fock

HF serves as the starting point for all the advanced and more accurate approximations to solve the time-independent electronic Schrodinger equation. If we omit the parametric dependence on the nuclear coordinates, Eq. 2.7 can be rewritten as

$$H_e\psi(\mathbf{r}) = E_e\psi(\mathbf{r}). \quad (2.9)$$

The fermionic nature of electrons constrains the choice of $\psi(\mathbf{r})$ - it has to change sign if the coordinates of any two electrons are switched and it has to be orthonormalized. The former condition is referred to as antisymmetry of the electronic wavefunction and gives rise to the famous Pauli exclusion principle.

In most chemical problems, one is interested in the ground state energy, E_0 of a collection of

Chapter 2. Methodology

atoms. This can be achieved by finding the $\psi(\mathbf{r})$ that minimizes the energy of the system. This idea is supported by the variational principle which ensures that energy is always greater than or equal to E_0 for any given $\psi(\mathbf{r})$,

$$E[\psi(\mathbf{r})] = \int \psi^* H_e \psi d\mathbf{r} \equiv \geq E_0 \quad (2.10)$$

where the integral represents the average (expectation) value of the Hamiltonian.

HF principle builds an *ansatz* for the electronic wavefunction in terms of an antisymmetric product of functions which only depend on coordinates of one electron,

$$\psi_{HF}(\mathbf{r}) = \frac{1}{\sqrt{N!}} \det |\phi_1(\mathbf{r}_1)\phi_1(\mathbf{r}_2)\phi_1(\mathbf{r}_3)\dots\phi_1(\mathbf{r}_N)| \quad (2.11)$$

Replacing this *ansatz* in Eq. 2.9 for ψ leads to the HF energy expression. Solving this energy expression further using variational principle and under the assumption that the one electron wavefunctions, also referred to as orbitals, are orthonormal leads to so called Hartree-Fock equations,

$$\left[-\frac{1}{2}\nabla^2 + v_{ext}(\mathbf{r}) + \int \frac{\rho(\mathbf{r}')}{|\mathbf{r}-\mathbf{r}'|} d\mathbf{r}' \right] \phi_i(\mathbf{r}) + \int v_X(\mathbf{r},\mathbf{r}') \phi_i(\mathbf{r}') d\mathbf{r}' = \epsilon_i \phi_i(\mathbf{r}), \quad (2.12)$$

where $\rho(\mathbf{r})$ is the Coulomb potential signifying electron-electron repulsion and $v_X(\mathbf{r},\mathbf{r}')$ is the so called exchange potential resulting from the anti-symmetry requirement of electronic wavefunction. The HF equations need to be solved iteratively (self-consistently) since $\rho(\mathbf{r})$ and $v_X(\mathbf{r},\mathbf{r}')$ depend on the orbitals $\phi_i(\mathbf{r})$. Furthermore, v_{ext} is the average external potential felt by the electrons due to all the nuclei in the system which is why HF is often referred to as self-consistent, mean field approximation to the many-body electronic problem and the Eqs. 2.12 are called Self-Consistent Field (SCF) equations¹⁵.

The mean-field approximation in HF theory fails to capture Columbic correlations which can be systematically included by more advanced, post-HF methods¹⁶.

The sum of the occupied orbital energies ϵ_i gives the total energy of the system. The orbital energies for occupied orbitals are further related to the ionization potentials of the molecule through Koopman's theorem¹⁷.

2.3 Density Functional Theory

Density functional theory differs from the HF and post-HF methods in that it considers the electronic density, in contrast with the electronic wavefunction, as the main entity from which

all physical quantities can be calculated¹⁸. For a system of N electrons, the wavefunction corresponding to each electronic eigenstate depends on $3N$ variables (x, y, z degree of freedom for each electron) whereas the electronic density is a function of just 3 variables. The two quantities are related by the relation,

$$\rho(\mathbf{r}) = N \int d^3\mathbf{r}_1 \dots \int d^3\mathbf{r}_N \Psi^*(\mathbf{r}, \mathbf{r}_2, \dots, \mathbf{r}_N) \Psi(\mathbf{r}, \mathbf{r}_2, \dots, \mathbf{r}_N) \quad (2.13)$$

where Ψ in this case is a normalized electronic wavefunction and a solution to Eq. 2.7. The theoretical framework for DFT is based upon two theorems first presented and proved by Walter Kohn and Pierre Hohenberg in 1964¹⁹. The **HK1** theorem proves that the external potential v_{ext} is uniquely determined by the ground-state electronic density up to a trivial constant; **HK2** theorem proves the existence of an energy functional, $E[\rho]$, which is minimized by the ground-state electronic density, ρ_0 , and thus serves as the variational principle of DFT. Further development of DFT came at the hands of Walter Kohn and Lu JU Sham who managed to cast the complicated many-body problem of interacting particles onto a system of non-interacting particles with the same density as the interacting system. This led to the development of so called Kohn-Sham (KH) equations²⁰ which resemble the Hartree-Fock equations in structure and also their self-consistent nature.

$$\left[-\frac{1}{2}\nabla^2 + V_s(\mathbf{r}) \right] \phi_i(\mathbf{r}) = \epsilon_i \phi_i(\mathbf{r}) \quad (2.14)$$

where $V_s(\mathbf{r})$ is the single-particle effective potential defined as,

$$V_s(\mathbf{r}) = v_{ext}(\mathbf{r}) + \int \frac{\rho(\mathbf{r}')}{|\mathbf{r} - \mathbf{r}'|} d\mathbf{r}' + V_{XC}[\rho(\mathbf{r})] \quad (2.15)$$

where the first term is the external potential; second term is the Hartree-type Coulomb potential describing electron-electron repulsion and the last term is the exchange-correctional potential which encompasses all many-particle interactions between electrons. The solution to the Eq. 2.14 gives one-electron orbitals for the non-interacting system which reproduce the electronic density of the original interacting system,

$$\rho(\mathbf{r}) = \sum_{i=1}^N |\phi_i(\mathbf{r})|^2 \quad (2.16)$$

Exchange-Correlation Functional

The last term in Eq. 2.15 is often approximated by so called exchange-correlation functional and contains the major parts of electronic exchange and correlation effects. KH managed to

Chapter 2. Methodology

show that for slow-varying densities the following relation holds,

$$E_{XC}[\rho] = \int \rho(\mathbf{r}) \epsilon_{xc}[\rho] d\mathbf{r} \quad (2.17)$$

where $E_{XC}[\rho]$ is the electronic exchange-correlation energy functional and $\epsilon_{xc}[\rho]$ is the energy-density, energy per electron, functional expressable in terms of one and two-particle density matrices. Following the equation above, the last term in Eq. 2.15 is given by,

$$V_{XC}[\rho(\mathbf{r})] \equiv \frac{\partial E_{XC}[\rho]}{\rho(\mathbf{r})}. \quad (2.18)$$

Unlike HF, the orbital energies, ϵ_i in Eq. 2.14 do not have any physical meaning and are related to the total electronic energy as,

$$E = \sum_{i=1}^N \epsilon_i - \frac{1}{2} \int d\mathbf{r} \int d\mathbf{r}' \frac{\rho(\mathbf{r})\rho(\mathbf{r}')}{|\mathbf{r} - \mathbf{r}'|} + E_{XC}[\rho(\mathbf{r})] - \int V_{XC}[\rho(\mathbf{r})] \rho(\mathbf{r}) d\mathbf{r}. \quad (2.19)$$

Unfortunately, as was realized by KH, there is no exact functional form of $E_{XC}[\rho(\mathbf{r})]$ for arbitrary densities. Approximations, and parametrization, of the exchange-correlation functionals are, therefore, needed the simplest of which is the Local Density Approximation (LDA) which assumes that the exchange-correlation energy density per particle at every position in space for a molecule is the same as it would be for the uniform electron gas (UEG) having the same density as found at that position. It is customary to write the exchange-correlation functional as a sum of an exchange term and a correlation term

$$E_{XC}^{LDA} = E_X^{LDA} + E_C^{LDA} \quad (2.20)$$

where the exchange term has a simple analytic expression and the correlation term is obtained by fitting the results of accurate quantum Monte-Carlo calculations of UEG²¹. In principle, in LDA the exchange-correlation energy depends on just the density at any given point.

The next natural refinement could be made by making the energy-density depend not only on just the local density but also on its first derivative. This gives rise to the Generalized Gradient Approximation (GGA)²²⁻²⁴,

$$E_{XC}^{GGA}[\rho] = \int \rho(\mathbf{r}) \epsilon_{xc}(\rho(\mathbf{r}), |\nabla \rho(\mathbf{r})|) d\mathbf{r} \quad (2.21)$$

The higher, more accurate approximations are meta-GGA²⁵⁻²⁷ which include the second derivative of density and hybrid functionals²⁸⁻³⁰ which include a certain fraction of the exact Hartree exchange expanded in terms of KH orbital.

Jacob's Ladder

This hierarchy of DFT exchange-correlational functionals is often depicted conceptually in a so called Jacob's Ladder (Figure 2.4) where at the bottom is the Hartree world with just the exchange part of the correlation; the top is the coveted world of chemical accuracy with full exchange-correlation interactions and the in between are the various rungs of the ladder signifying various approximations to the KH exchange-correlation energy and, in principle, with increasing accuracy, and, therefore, increasing computational cost, from bottom rung (LSD) to top (RPA). Since DFT fails to explicitly account for long-range van der Waal's interactions, additional functions for dispersion corrections have been proposed in the literature along with the given exchange-correlation functionals like Grimme's D2³¹ and D3³² methods or the charge-density dependent dDSc dispersion correction³³. In our work, we have chosen to work at the GGA level with PBE exchange-correlation functional²³ and dDSc dispersion correction which is quite ubiquitous in the study of chemical reactions on metallic surfaces and offers a brilliant compromise between accuracy and computational cost^{34;35}.

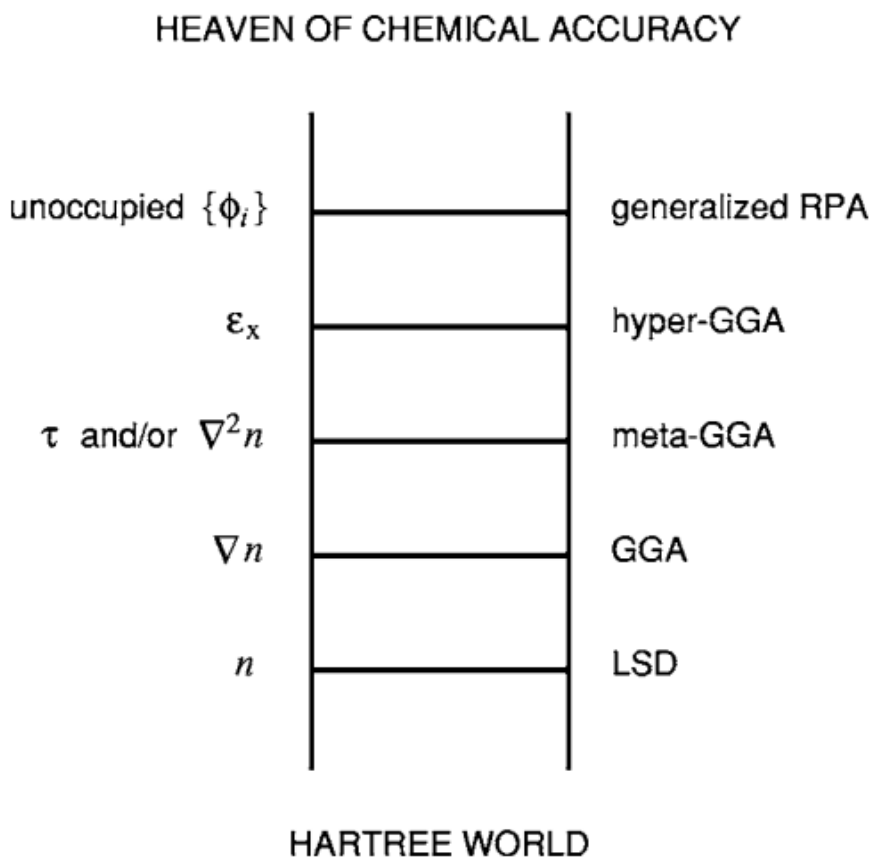


Figure 2.4: Jacob's ladder of density functional approximations to the exchange-correlation energy. Taken from ref³⁶.

Periodic Systems

Most of the DFT formalism presented above is valid for both molecular and extended systems; some conceptual and practical differences in the treatment of two systems are worth mentioning. First of all, the extended phase is generally composed of many more atoms than molecular systems which modifies its electron structure. In fact, it is customary for extended systems to talk about energy bands localized on a range of energy as opposed to molecular orbitals in molecular systems. Moreover, as described in Section 2.1, the catalyst surfaces in computational heterogeneous catalysis are often treated as periodic slabs (Figure 2.3) to mimic the intrinsic periodicity found in metallic crystals. This periodicity of the crystals is also displayed in the underlying Hamiltonian of the system. Thanks to this periodicity of the Hamiltonian, the extended systems can be studied using a small periodic unit of the underlying lattice subjected to Periodic Boundary Conditions (PBC) of Born-Von Karman type³⁷ which can be states as,

$$\psi(\mathbf{r} + \mathbf{T}) = \psi(\mathbf{r}) \quad (2.22)$$

where \mathbf{T} is a translation vector such that:

$$\mathbf{T} = \sum_i N_i \mathbf{a}_i \quad (2.23)$$

where \mathbf{a}_i are the primitive lattice vectors and N_i are integers by which the primitive unit cell of the lattice is multiplied to achieve the final simulation cell i.e. the *supercell*. Furthermore, Bloch showed that for an external potential that has the same periodicity as the Bravais lattice i.e. $V_{ext}(\mathbf{r} + \mathbf{T}) = V_{ext}$, the wavefunction of the non-interacting electrons (MO) for the entire crystal can be written as,

$$\psi_{\mathbf{k}}(\mathbf{r}) = e^{i\mathbf{k}\cdot\mathbf{r}} u_{\mathbf{k}}(\mathbf{r}) \quad (2.24)$$

where $u_{\mathbf{k}}(\mathbf{r} + \mathbf{T}) = u_{\mathbf{k}}(\mathbf{r})$ and \mathbf{k} is a point in the first Brillouin zone (1BZ) which is the most symmetric unit in the underlying reciprocal (Bravais) lattice. Bloch theorem, therefore, allows to perform DFT simulations for a single cell to get the Kohn-Sham wavefunctions for the entire (infinite) crystal. Due to Bloch theorem, each spatial orbital has an extra \mathbf{k} dependence in addition to the quantum number n and are denoted as $\psi_{n,\mathbf{k}}(\mathbf{r})$. A different Kohn-Sham equation is solved for each \mathbf{k} point to obtain the corresponding Bloch-wavefunctions, $\psi_{n,\mathbf{k}}(\mathbf{r})$. In principle, there are infinite \mathbf{k} points in 1BZ but the quantities like total energy converge with the number of \mathbf{k} points used. In practice, the calculations for periodic systems are performed on a grid in 1BZ (\mathbf{k} -point grid) and the quantities like density and total energy can be obtained

by averaging over 1BZ:

$$\rho(\mathbf{r}) = \frac{V_{cell}}{2\pi} \int_{BZ} \left(\sum_i^{Nel} |\psi_{n,\mathbf{k}}(\mathbf{r})|^2 \right) d\mathbf{k} = \frac{V_{cell}}{2\pi} \int_{BZ} \left(\sum_i^{Nel} |u_{n,\mathbf{k}}(\mathbf{r})|^2 \right) d\mathbf{k}. \quad (2.25)$$

2.4 Thermodynamic Model

In this section we give the equations relevant for converting the electronic energies obtained from DFT into useful thermodynamical quantities.

Adsorption free energy

For a slab containing i different species adsorbed on the surface, one could define the adsorption free energy as follows

$$G_{ads} = G_{slab-\{n_i\}} - G_{slab} - \sum_i n_i G_i(gas) \quad (2.26)$$

where $G_{slab-\{n_i\}}$ and G_{slab} are the free energy of the full slab-adsorbate system and the free energy of the bare slab, respectively. The latter is usually approximated as the DFT electronic energy of the slab i.e. $G_{slab} = E_{slab}$ whereas the former also included enthalpic and entropic contributions for the adsorbate part only. The n_i is the number of species i adsorbed on the surface and $G_i(gas)$ is the gas phase Gibbs free energy of species i .

For cases where there is dissociative adsorption as in case of $H_2(O_2)$, $G_i(gas)$ can either be taken as half of the gas phase free energies of $H_2(O_2)$ molecule or a calculation for single H(O) atom can be performed in the gas phase; the former approach was adopted in our work. With this definition, a negative value of G_{ads} shows an exothermic adsorption process. If $|G_{ads}| < 50 \text{ kJ.mol}^{-1}$, it is mostly considered as physisorption whereas $|G_{ads}| > 50 \text{ kJ.mol}^{-1}$ signifies a chemisorption process.

We further need to define different terms involved in $G_i(gas)$ for entropic and enthalpic contributions. The Gibbs free energy is defined as

$$G = H(T) - T \times S(T) = U(T) + PV - T \times S(T) = U(T) + k_B T - T \times S(T) \quad (2.27)$$

Where $H(T)$ is the enthalpy, $S(T)$ is the entropy, $U(T)$ is the internal energy, T is the temperature and k_B is the Boltzmann constant. We further need to give expressions for different components of $U(T)$ and $S(T)$ which are pretty standard equations and can be found in thermodynamics textbooks for example in chapter 10 of ref³⁸ and are implemented in simulation

Chapter 2. Methodology

codes like ASE⁷ or the specialized thermochemistry python library Panther³⁹. Here we only give the final equations for different terms.

U(T)

The internal energy of an ideal gas can be divided into further components as

$$U(T) = E_{elec} + ZPVE + U_{trans} + U_{rot} + U_{vib}. \quad (2.28)$$

The first term is the electronic energy which can be obtained by performing a DFT (or post-HF) calculation for one molecule. The second term is the zero-point vibrational energy and it requires computing the frequency modes of the molecule which can also be done using DFT. Once the frequency modes ω_i are known, $ZPVE$ can be calculated as below

$$ZPVE = \frac{1}{2} \sum_i h\omega_i \quad (2.29)$$

where h is Planck's constant. The third term in Eq. 2.28 is translational contribution and is given by $(3/2)RT$ for a 3-dimensional ideal gas where R is the ideal-gas constant. The fourth term is the rotational component and is given by RT for a linear molecule and $(3/2)RT$ for non-linear molecules. The last term is the vibrational contribution and it also requires calculating the frequency modes of the molecule. For a molecule containing N atoms, there are $3N-5$ ($3N-6$) vibrational degrees of freedom (DOF) if it is linear (non-linear). The general expression for the vibrational energy is given by,

$$U_{vib} = R \sum_i^{3N-6(5)} \frac{h\omega_i}{k_B(e^{h\omega_i/k_B T} - 1)} \quad (2.30)$$

S(T)

Just like $U(T)$, entropy can also be divided into different components

$$S(T) = S_{elec} + S_{trans} + S_{rot} + S_{vib}. \quad (2.31)$$

The first term is the electronic entropy which is zero if the ground state of the system is a singlet state and equal to $R \ln(2S + 1)$ if the ground state is a multiplet where S is the multiplicity of the ground state. The translational component of entropy can be calculated as given below,

$$S_{trans} = R \left\{ \ln \left[\left(\frac{2\pi M k_B T}{h^2} \right)^{3/2} \frac{V^0}{N_A} \right] + \frac{5}{2} \right\} \quad (2.32)$$

where M is the molar mass of the molecule, N_A is the Avogadro's constant and V^0 is the standard volume which can be related to stand state pressure by the ideal-gas law $P^0 V^0 = k_B T$. This is the only component of the entropy which has a volume dependence and thus requires choosing a stand state which in most cases is 1 atm pressure. The rotational entropy has different expressions depending on if the molecule is linear or non-linear. For linear molecules the expression is,

$$S_{rot}^{linear} = R \left[\ln \left(\frac{8\pi^2 I I k_B T}{\sigma h^2} \right) + 1 \right] \quad (2.33)$$

where I is the moment of inertial of the molecule and σ is the rotational constant which depends on the symmetry of the molecule and can be found in tabulated values if the point group of the molecule is known. For more generally encountered non-linear molecules, the rotational entropy is more complicated and requires computing three different moments of inertia along three directions, I_A , I_B and I_C ,

$$S_{rot}^{non-linear} = R \left\{ \ln \left[\frac{\sqrt{\pi I_A I_B I_C}}{\sigma} \left(\frac{8\pi^2 I I k_B T}{h^2} \right) \right] + \frac{3}{2} \right\} \quad (2.34)$$

The last term in Eq. 2.31 is the vibrational contribution to the entropy. This is given as,

$$S_{vib} = R \sum_i^{3N-6(5)} \left[\frac{h\omega_i}{k_B T (e^{h\omega_i/k_B T} - 1)} - \ln \left(1 - e^{-h\omega_i/k_B T} \right) \right] \quad (2.35)$$

It should be noted that Eq. 2.30 and Eq. 2.35 are valid under harmonic approximation. Using the equations provided above, one could calculate the Gibbs free energy of the gas phase species in Eq. 2.26. For the $G_{slab-adsorbate}$, however, if one decides to include the enthalpic and entropic contributions, then only the vibrational DOF are taken into account, the adsorption results in loss of translational and rotational DOF. During the course of work, this was only done for the adsorbate part for which frequency modes were calculated and used to calculate ZPVE and the vibrational contributions to the internal energy (Eq. 2.30) and entropy (Eq. 2.35).

2.5 Solvation - MMsolv

As established before in Chapter 1, most chemical transformations involving biomass valorization take place in liquid water. To study the effects of liquid water on the adsorption behavior of molecules on metallic surfaces, we have implemented a modified version of the hybrid quantum-mechanical/molecular-mechanics (QM/MM) approach developed in our group. The technique termed MMsolv⁴⁰ and implemented in a freely available package called SolvHybrid is an explicit solvation scheme that makes use of the optimized adsorption ge-

Chapter 2. Methodology

ometries and corresponding point charges obtained from a single DFT calculation (QM) and uses that information to build a MM calculation in combination with TIP3P model of liquid water⁴¹. In practice, the MM calculation implements an alchemical transformation based on thermodynamic integration (TI) to calculate the differences in solvation of the molecules from bulk water to that on the interface of the solid metallic surface. The calculated difference of solvation free energy from this scheme in combination with the gas phase DFT adsorption free energy (Eq. 2.26) gives the full adsorption energy of the molecule in the presence of liquid water.

In order for this technique to be of any quantitative value, force fields for the metal-water interaction must be refined. Unfortunately, this has not been the case for Ru. Therefore, we have modified the original scheme of MMsol_v to instead calculate the solvation enthalpy differences between two different adsorption topologies making use of modified UUF⁴² parameters for metal-water and adsorbate-water interactions. The modified scheme is pictorially explained in Fig. Figure 2.5 and is deemed to work well only for surfaces which are reasonably covered with adsorbates to minimize the direct interaction of MM water with the metallic surface. Furthermore, the scheme requires choosing a reference adsorption geometry against which differences of solvation for all other adsorption geometries are calculated, however, this choice is arbitrary and scheme is self consistent. Overall, the scheme implements the alchemical transformation where one starts with one adsorption geometry in water and the other one in gas phase and ends up with a state where the second geometry is in water and the first one in gas phase.

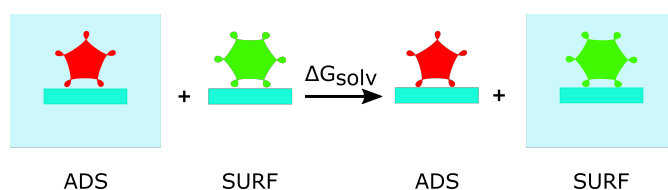


Figure 2.5: The modified MMsol_v scheme to calculate the difference in solvation enthalpy between two adsorption geometries on the metallic surface. The light blue rectangle represents a TIP3P water box of certain length around the adsorption geometry.

Similar to the original MMsol_v approach, TI was used to carry out the alchemical transformation in three steps. In the first *decharge* step, the DFT charges on the metallic surface and the adsorbates were gradually removed. The second step involved modification of the *van der Waal* interactions to go from one adsorption geometry to the other and finally, in the third *recharging* step the DFT charges were gradually introduced on the new surfaces with swapped adsorption geometries. Each step consisted of 11 TI windows and each window further involved three steps namely minimization, heating and equilibration. Furthermore, in accordance with the original MMsol_v approach, the metal and adsorbate parts were kept fixed to their optimized DFT geometries during the TI calculation. Using the scheme depicted

in Figure 2.5, the free energy difference of solvation of involved in the transformation can be calculated as,

$$\begin{aligned}\Delta G_{solv} = & E_{SURF}^{solv} + E_{ADS}^{gas} - E_{ADS}^{solv} - E_{SURF}^{gas} \\ & \left(E_{SURF}^{solv} - E_{ADS}^{solv} \right) + E_{ADS}^{gas} - E_{SURF}^{gas} \\ & \Delta TI + E_{ADS}^{gas} - E_{SURF}^{gas}\end{aligned}\quad (2.36)$$

where the ΔTI is the value obtained from the TI calculation and E_{ADS}^{gas} , E_{SURF}^{gas} are the gas phase single point energies for ADS and SURF adsorption geometries using MM force field. Under this convention, SURF is taken as the reference state and the transformation simulated by TI is ADS \rightarrow SURF.

2.6 Microkinetic Modelling

The microkinetic modelling based on *ab initio* Gibbs free energies of reaction intermediates and transition states was performed to study the potential poisoning of the catalyst surface by reacting phase species. Open source Python code *Micki* was used for the analysis. Here we give a brief overview of the *Micki* program; a detailed account of how the program works and its applications in heterogeneous catalysis could be found in refs^{43;44}.

Given a set of elementary reactions $\{r_i\}$, *Micki* solves the following set of differential equations for the concentration of each specie $\{C_i\}$,

$$\frac{dC_i}{dt} = \sum_{n=1}^{N_i} r_n - \sum_{m=1}^{M_i} r_m \quad (2.37)$$

where r_n is the reaction that generates C_i and r_m is the reaction that consumes C_i .

Fluid Phase

Micki treats the fluid phase as the ideal gas mixture:

$$Q_{\text{Ideal-gas}}(\{N_i\}) = \prod_i \frac{q_i^{N_i}}{N_i!} \quad (2.38)$$

where q_i is the one particle partition function of species i which is a product of translational, rotational, vibrational and electronic partition functions:

$$q_i^{fluid} = q_i^{trans} q_i^{rot} q_i^{vib} q_i^{elec}, \quad (2.39)$$

Chapter 2. Methodology

from which different contributions to energy and entropy can be computed using the equations defined in section 2.4. In *Micki*, the reference state is taken to be 1 Molar at standard temperature, instead of 1 atm pressure, which only affects the translational partition function and thus translation entropy (Eq. 2.32). This reference state is useful when taking into account solvation effects which can be easily included in the kinetic model by giving estimates of Gibbs free energy of solvation, obtained either by some computational method (continuum approaches) or from experiments.

Furthermore, the adsorption of gas phase species was treated under 2D ideal gas model where the transition state of adsorption was calculated as the adsorbing molecule in a 2D box of area A_{site} , the area per lattice site, which is defined in the following. This essentially represents a state where molecule is allowed to move in only two directions planar to the surface and has lost the third translation degree of freedom.

Lattice

Micki defined a lattice in terms of its geometry i.e. hexagonal, square etc. The geometry is defined by a lattice constant and the number of nearest neighbors. For example, Figure 2.6, shows a hexagonal lattice, as found in hcp(0001) or fcc(111) surfaces, with lattice constant a and each lattice site surrounded by 6 neighboring sites. This is the same lattice we have used in our work to study the poisoning of Ru(0001) surface. For such a lattice type, the area per lattice site, A_{site} is given by,

$$A_{site} = \frac{\sqrt{3}}{4} a^2. \quad (2.40)$$

The partition function for the lattice species was calculated as,

$$Q_{\text{Lattice}}(\{N_i\}) = \frac{M!}{N_0!} \prod_i \frac{q_i^{N_i}}{N_i!} \quad (2.41)$$

where N_i is the number of sites occupied by species i , assuming that each molecules adsorbs at exactly one site, out of a total of M sites and $N_0 \equiv M - \sum_i N_i$ is the number of empty lattice sites. The one-particle partition function for adsorbates is calculates as,

$$q_i^{\text{adsorbate}} = q_i^{\text{elec}} q_i^{\text{vib}}, \quad (2.42)$$

which means that all degrees of freedom are treated as vibrations under the harmonic approximation. Micki also allows multidentate binding for bigger adsorbates but this was not used in our work.

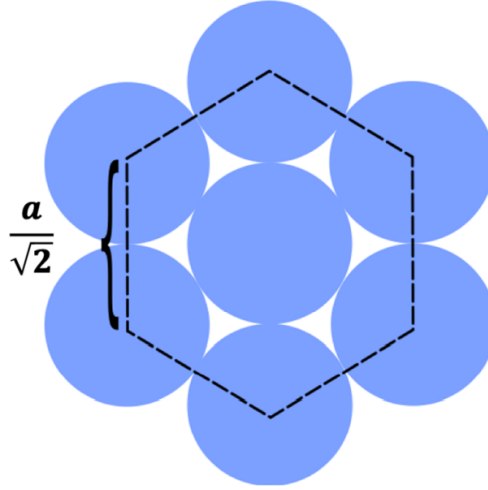


Figure 2.6: A hexagonal lattice with lattice constant a and each atom surrounded by 6 neighbors. Taken from ref⁴⁴

Equilibrium and rate constants

The equilibrium constant in Micki is calculated using the standard thermodynamic equation,

$$K_{eq}^{\circ} = \exp \left[\frac{\Delta G_{rxn}^{\circ}}{k_B T} \right] \quad (2.43)$$

where ΔG_{rxn}° is the standard Gibbs free energy change of reaction calculated as,

$$\Delta G_{rxn}^{\circ} = \mu_C^{\circ} - \mu_A^{\circ} - \mu_B^{\circ} \quad (2.44)$$

where μ_X° is the corresponding standard chemical potential which for a fluid phase species, X , is given by,

$$\mu_X^{\circ} = -k_B T \ln [q_X^{\circ}] \quad (2.45)$$

and for on-lattice species i can be calculated as,

$$\mu_i = k_B T \ln \left[\frac{\theta_0 \sigma_i q_i}{\theta_i} \right] \quad (2.46)$$

where θ_0 is the fraction of empty sites, N_0/M and θ_i is the fraction of sites occupied by species i , N_i/M .

The rate constants in Micki are calculated using the standard transition rate theory of Ar-

Chapter 2. Methodology

Arrhenius type. For an on site reaction, the forward and reverse rate constants are given by,

$$k_{for} = \frac{k_B T}{h} \exp \left[-\frac{\Delta G_{for}^\ddagger}{k_B T} \right] \quad (2.47)$$

$$k_{rev} = \frac{k_B T}{h} \exp \left[-\frac{\Delta G_{rev}^\ddagger}{k_B T} \right] \quad (2.48)$$

where ΔG_{for}^\ddagger is calculated using Eq. 2.44 considering the transition state of the reaction as the product. The imaginary modes of the transition state are ignored in the calculation of its partition function from Eq. 2.42. For the adsorption reaction, the rate constant is calculated by the collision theory,

$$k_{ads} = S_0 N_A A_{site} \sqrt{\frac{k_B T}{2\pi m_A}} \quad (2.49)$$

where S_0 is the sticking coefficient taken to be 1 for all gas phase species in our study. Furthermore, we have $K_{des} = k_{ads}/K_{eq}$.

Reactor - CSTR

Micki implements a simplified CSTR reactor model whereby they fix the concentration of some gas phase species. This amounts to a stirred reactor with infinite flow rate. Since the purpose of our study was to investigate the potential poisoning of the catalyst surface, we are only interested in the steady-state solution which is easily achieved by this simplified reactor model.

Bibliography

- [1] Kozlov, S. M.; Neyman, K. M. Catalysis from First Principles: Towards Accounting for the Effects of Nanostructuring. *Topics in Catalysis* **2013**, *56*, 867–873.
- [2] Moore, G. E. Cramming more components onto integrated circuits, Reprinted from Electronics, volume 38, number 8, April 19, 1965, pp.114 ff. *IEEE Solid-State Circuits Society Newsletter* **2006**, *11*, 33–35.
- [3] Mazur, G.; Makowski, M. Development and Optimization of Computational Chemistry Algorithms. *Computing and Informatics* **2009**, *28*, 115–125.
- [4] Herbst, M. F.; Levitt, A. Black-box inhomogeneous preconditioning for self-consistent field iterations in density functional theory. *Journal of Physics: Condensed Matter* **2020**, *33*, 085503, Publisher: IOP Publishing.
- [5] Freund, H.-J. Models for heterogeneous catalysts: studies at the atomic level. *Rendiconti Lincei* **2017**, *28*, 5–18.
- [6] Freund, H.-J.; Heyde, M.; Kuhlenbeck, H.; Nilius, N.; Risse, T.; Schmidt, T.; Shaikhutdinov, S.; Sterrer, M. Chapter model systems in heterogeneous catalysis at the atomic level: a personal view. *Science China Chemistry* **2020**, *63*.
- [7] Larsen, A. H. *et al.* The atomic simulation environment—a Python library for working with atoms. *Journal of Physics: Condensed Matter* **2017**, *29*, 273002.
- [8] Feibelman, P. J. Partial dissociation of water on Ru(0001). *Science (New York, N.Y.)* **2002**, *295*, 99–102, Place: United States.
- [9] Sun, W.; Ceder, G. Efficient creation and convergence of surface slabs. *Surface Science* **2013**, *617*, 53–59.
- [10] Szabo, A.; Ostlund, N. *Modern Quantum Chemistry: Introduction to Advanced Electronic Structure Theory*; Dover Publications: Mineola, New York, 1996.
- [11] Pisani, C.; Schütz, M.; Casassa, S.; Usvyat, D.; Maschio, L.; Lorenz, M.; Erba, A. Cryscor: a program for the post-Hartree–Fock treatment of periodic systems. *Phys. Chem. Chem. Phys.* **2012**, *14*, 7615–7628, Publisher: The Royal Society of Chemistry.
- [12] Müller, C.; Paulus, B. Wavefunction-based electron correlation methods for solids. *Phys. Chem. Chem. Phys.* **2012**, *14*, 7605–7614, Publisher: The Royal Society of Chemistry.
- [13] Neyman, K. M.; Illas, F. Theoretical aspects of heterogeneous catalysis: Applications of density functional methods. *Catalysis Today* **2005**, *105*, 2–16.

Chapter 2. Methodology

- [14] Nørskov, J.; Scheffler, M.; Toulhoat, H. Density Functional Theory in Surface Science and Heterogeneous Catalysis. *MRS Bulletin* **2006**, *31*, 669–674.
- [15] Lehtola, S.; Blockhuys, F.; Van Alsenoy, C. An Overview of Self-Consistent Field Calculations Within Finite Basis Sets. *Molecules (Basel, Switzerland)* **2020**, *25*.
- [16] Townsend, J.; Kirkland, J. K.; Vogiatzis, K. D. In *Mathematical Physics in Theoretical Chemistry*; Blinder, S., House, J., Eds.; Elsevier, 2019; pp 63–117.
- [17] Koopmans, T. Über die Zuordnung von Wellenfunktionen und Eigenwerten zu den Einzelnen Elektronen Eines Atoms. *Physica* **1934**, *1*, 104–113.
- [18] Parr, R. G.; Weitao, Y. *Density-Functional Theory of Atoms and Molecules*; Oxford University Press, 1994.
- [19] Hohenberg, P.; Kohn, W. Inhomogeneous Electron Gas. *Phys. Rev.* **1964**, *136*, B864–B871, Publisher: American Physical Society.
- [20] Kohn, W.; Sham, L. J. Self-Consistent Equations Including Exchange and Correlation Effects. *Phys. Rev.* **1965**, *140*, A1133–A1138, Publisher: American Physical Society.
- [21] Ceperley, D. M.; Alder, B. J. Ground State of the Electron Gas by a Stochastic Method. *Phys. Rev. Lett.* **1980**, *45*, 566–569, Publisher: American Physical Society.
- [22] Perdew, J. P.; Wang, Y. Accurate and simple analytic representation of the electron-gas correlation energy. *Phys. Rev. B* **1992**, *45*, 13244–13249, Publisher: American Physical Society.
- [23] Perdew, J. P.; Burke, K.; Ernzerhof, M. Generalized Gradient Approximation Made Simple. *Phys. Rev. Lett.* **1996**, *77*, 3865–3868, Publisher: American Physical Society.
- [24] Hammer, B.; Hansen, L. B.; Nørskov, J. K. Improved adsorption energetics within density-functional theory using revised Perdew-Burke-Ernzerhof functionals. *Phys. Rev. B* **1999**, *59*, 7413–7421, Publisher: American Physical Society.
- [25] Zhao, Y.; Truhlar, D. G. A new local density functional for main-group thermochemistry, transition metal bonding, thermochemical kinetics, and noncovalent interactions. *The Journal of Chemical Physics* **2006**, *125*, 194101, Publisher: American Institute of Physics.
- [26] Becke, A. D.; Johnson, E. R. A simple effective potential for exchange. *The Journal of Chemical Physics* **2006**, *124*, 221101, Publisher: American Institute of Physics.
- [27] Sun, J.; Remsing, R. C.; Zhang, Y.; Sun, Z.; Ruzsinszky, A.; Peng, H.; Yang, Z.; Paul, A.; Waghmare, U.; Wu, X.; Klein, M. L.; Perdew, J. P. Accurate first-principles structures and energies of diversely bonded systems from an efficient density functional. *Nature Chemistry* **2016**, *8*, 831–836.

-
- [28] Becke, A. D. Density-functional thermochemistry. III. The role of exact exchange. *The Journal of Chemical Physics* **1993**, 98, 5648–5652, Publisher: American Institute of Physics.
- [29] Perdew, J. P.; Ernzerhof, M.; Burke, K. Rationale for mixing exact exchange with density functional approximations. *The Journal of Chemical Physics* **1996**, 105, 9982–9985, Publisher: American Institute of Physics.
- [30] Heyd, J.; Scuseria, G. E.; Ernzerhof, M. Hybrid functionals based on a screened Coulomb potential. *The Journal of Chemical Physics* **2003**, 118, 8207–8215, Publisher: American Institute of Physics.
- [31] Grimme, S. Semiempirical GGA-type density functional constructed with a long-range dispersion correction. *Journal of Computational Chemistry* **2006**, 27, 1787–1799, Publisher: John Wiley & Sons, Ltd.
- [32] Grimme, S.; Antony, J.; Ehrlich, S.; Krieg, H. A consistent and accurate ab initio parametrization of density functional dispersion correction (DFT-D) for the 94 elements H-Pu. *The Journal of Chemical Physics* **2010**, 132, 154104, Publisher: American Institute of Physics.
- [33] Steinmann, S. N.; Corminboeuf, C. A generalized-gradient approximation exchange hole model for dispersion coefficients. *The Journal of Chemical Physics* **2011**, 134, 044117, Publisher: American Institute of Physics.
- [34] Göltl, E.; Murray, E. A.; Tacey, S. A.; Rangarajan, S.; Mavrikakis, M. Comparing the performance of density functionals in describing the adsorption of atoms and small molecules on Ni(111). *Surface Science* **2020**, 700, 121675.
- [35] Gautier, S.; Steinmann, S. N.; Michel, C.; Fleurat-Lessard, P.; Sautet, P. Molecular adsorption at Pt(111). How accurate are DFT functionals? *Phys. Chem. Chem. Phys.* **2015**, 17, 28921–28930, Publisher: The Royal Society of Chemistry.
- [36] Perdew, J. P.; Ruzsinszky, A.; Tao, J.; Staroverov, V. N.; Scuseria, G. E.; Csonka, G. I. Prescription for the design and selection of density functional approximations: More constraint satisfaction with fewer fits. *The Journal of Chemical Physics* **2005**, 123, 062201, Publisher: American Institute of Physics.
- [37] Ashcroft, N. W.; Mermin, N. *Solid State Physics*; Harcourt College Publishers: New York, 1976.
- [38] Cramer, C. J. *Essentials of Computational Chemistry: Theories and Models*, 2nd ed.; John Wiley & Sons, Ltd., 2002.

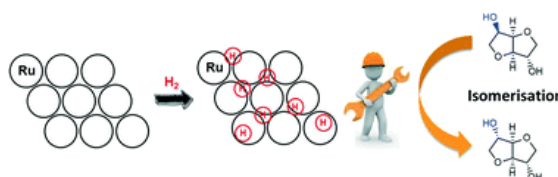
Chapter 2. Methodology

- [39] Mentel, L. M. PANTHER: Python Package for Anharmonic Thermochemistry. 2016–; <https://bitbucket.org/lukaszmentel/panther>.
- [40] Clabaut, P.; Schweitzer, B.; Götz, A. W.; Michel, C.; Steinmann, S. N. Solvation Free Energies and Adsorption Energies at the Metal/Water Interface from Hybrid Quantum-Mechanical/Molecular Mechanics Simulations. *Journal of Chemical Theory and Computation* **2020**, *16*, 6539–6549, PMID: 32931268.
- [41] Jorgensen, W.; Chandrasekhar, J.; Madura, J.; Impey, R.; Klein, M. Comparison of Simple Potential Functions for Simulating Liquid Water. *J. Chem. Phys.* **1983**, *79*, 926–935.
- [42] Rappé, A. K.; Casewit, C.; Colwell, K. S.; Goddard, W. A.; Skiff, W. M. UFF, a full periodic table force field for molecular mechanics and molecular dynamics simulations. *Journal of the American Chemical Society* **1992**, *114*, 10024–10035.
- [43] Hermes, E. D.; Janes, A. N.; Schmidt, J. R. Micki: A python-based object-oriented microkinetic modeling code. *The Journal of Chemical Physics* **2019**, *151*, 014112.
- [44] Hermes, E. D.; Janes, A. N.; Schmidt, J. R. Mechanistic Insights into Solution-Phase Oxidative Esterification of Primary Alcohols on Pd(111) from First-Principles Microkinetic Modeling. *ACS Catalysis* **2018**, *8*, 272–282.

3 Isosorbide

In this chapter we present the results of the theoretical investigation of the isomerization and amination reactions of isosorbide on supported Ru catalyst using periodic DFT and microkinetic modelling. The goal of the study was to elucidate the pivotal role of H_2 in the isomerization reaction of isosorbide and the potential poisoning of the catalyst surface by NH_x type species during the amination reaction. Results on the isomerization part have been published in the peer-reviewed journal article: H. Hu; A. Ramzan; R. Wischert; C. Michel; K. de Olivera Vigier; M. Pera-Titus, Pivotal role of H_2 in the isomerisation of isosorbide over a Ru/C catalyst, *Catalysis Science & Technology*, 11, 7973-7981, **2021**, <https://doi.org/10.1039/D1CY01709H>.

Abstract: Isosorbide isomerisation is a known reaction that can proceed over Ru and Ni-based heterogeneous catalysts. As a rule, an exogenous H_2 pressure (40–100 bar) is required, even though H_2 does not participate stoichiometrically in the reaction. By marrying experiments with DFT computations, we ascribe the role of H_2 in isosorbide isomerisation to a coverage effect on the catalyst surface. We demonstrate the possibility of conducting the reaction at a low H_2 pressure either in the presence of an inert gas to increase H_2 solubility in an underlying solvent or using 2-propanol as a hydrogen donor. This might benefit the economy and safety of a potential industrial process.

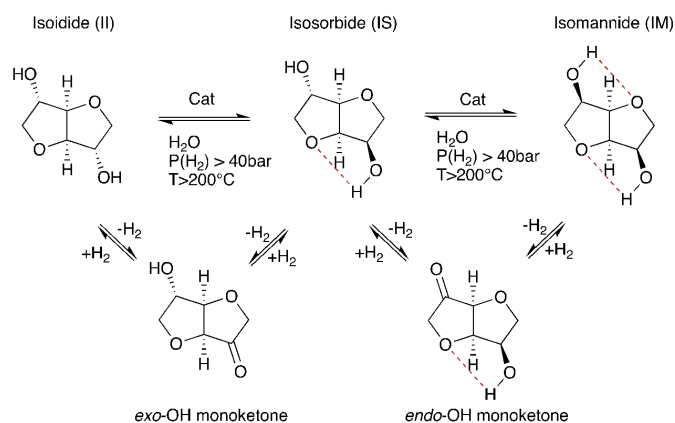


Isomerization **Part I**

3.1 Introduction

Isosorbide (IS) along with its isomers isomannide (IM) and isoidide (II), collectively referred to as isohexides, makes a group of biobased platform chemicals that have gained considerable interest over the past two decades as potential replacement to fossil-based products^{1–3}. In particular, isosorbide and its monamine and diamine derivatives have attracted great interest in the potential manufacturing of biobased polymers such as polyurethanes, copolyesters, polymethacrylates and polyamides which have better environmental footprint compared to fossil-based counterparts^{4–8}. Isohexides are obtained from acid-catalysed hydration of hexitols D-Sorbitol (IS), D-Mannitol (IM) and L-iditol (II) which can be produced through hydrogenation of monosaccharides, i.e. glucose and fructose¹ which in turn are produced from the hydrolysis of starch. Structurally, isohexides are diols consisting of two tetrahydrofuran rings fused in a rigid V-shaped structure (Scheme 3.1)^{9–13}. The three isomers differ in the relative configuration of the two secondary OH groups present on C2 and C5 carbon atoms: IS has OH groups in opposite (*endo-exo*) orientation relative to the ring skeleton, while IM (*endo-endo*) and II (*exo-exo*) have OH groups pointing in the same direction relative to the ring skeleton. Unlike *exo*-OH groups, *endo*-OH groups are better positioned to engage in intramolecular hydrogen-bonding with the oxygen atoms of the adjoining furan ring^{13;14}. These structural differences lead to differences in the physicochemical properties and reactivity of isohexides^{14;15}.

The catalytic isomerisation of IS was first described by Fletcher and Goepp in 1946 us-



Scheme 3.1: Structure of isohexide isomers: isomannide (IM) or 1,4:3,6-dianhydro-D-mannitol, isosorbide (IS) or 1,4:3,6-dianhydro-D-sorbitol, and isoidide (II) or 1,4:3,6-dianhydro-L-iditol. A possible isomerisation mechanism is driven by dehydrogenation- rehydrogenation through the monoketone intermediates.

ing Raney nickel for its dehydrogenating properties¹². Wright and Brandner performed the isomerisation in 1964 over Ni-Kieselguhr catalysts and pointed out an equilibrium distribution between the three isomers at ca. 55 % II, 39 % IS and 6 % IM¹⁶. Such thermodynamics-driven

equilibrium distribution is also at display in the synthesis of many other functional biobased chemicals derived from isohexides^{17–20}. With this perspective, understanding the isomerisation mechanism of the isohexide epimers is deemed a significant step towards rationalizing the outcomes of other transformations involving isohexides. In addition, the isomerisation reaction presents a viable route to obtaining isoidide which has less abundant sugar precursor (L-iditol)¹⁶ and is deemed more suitable for polymer applications due to its symmetric structure and high reactivity²¹.

The isomerisation of isohexides is believed to proceed *via* a dehydrogenation-rehydrogenation pathway (also referred to H₂-borrowing mechanism if no external pressure of H₂ is needed; Scheme 3.1)^{21;22}. When using a heterogeneous catalyst, since the intermediate (mono, di)ketones are not observed, dehydrogenation is often regarded as the rate-determining step²¹. An alternative route is the dehydration-rehydration pathway, but it was dismissed by authors in ref²¹ since the expected byproducts such as unsaturated isohexides or isohexides with OH group in 1-, 3-, 4- or 6-positions were absent in the reaction mixture obtained during the isomerisation of IS using Ru/C in water. Recently, Rose and co-workers studied in detail the mechanism for IM isomerisation²². Supported by deuterium-exchange experiments, they validated the dehydrogenation-hydrogenation mechanism at 120 °C. Above that temperature, and at a basic pH, full H–D exchange of all protons in IM was observed which they ascribed to a keto-enol equilibrium thereby hinting at a potential dehydration-rehydration mechanism. Considering that dimethyl isosorbide is also isomerised at similar conditions, the authors proposed an alternative *direct-hydride-exchange* pathway, preferentially at higher temperatures. They hypothesized that an α -C–H bond scission at high temperature results in the formation of a carbenium ion and a surface hydride (heterolytic cleavage). The carbenium ion then rotates around the C=O bond to facilitate the inversion of the chiral centre before being rehydrogenated from the opposite direction to yield the isomerized product. For species adsorbed on metallic surfaces, this mechanism resulting from a potential heterolytic cleavage is difficult to differentiate from dehydrogenation-rehydrogenation and would require a deeper investigation using *ab initio* modelling.

Notably, very high H₂ pressures (40–100 bar) were necessary to reach equilibrium when using Ni-Kieselguhr to isomerise IS, even if H₂ does not participate stoichiometrically to the reaction¹⁶. The II yield increased linearly with the pH (8–11) of the initial solution. At pH>11, poor selectivity was observed due to side reactions, which were not described. Earlier, Wright and Hartmann observed a similar behaviour for the isomerization of hexitols i.e. D-glucitol (sorbitol), D-mannitol and L-iditol which are the biobased precursors of IS, IM and II, respectively, using the same Ni-based catalytic system²³. Starting from a solution of D-glucitol under H₂ (>100 bar) and a base, a final 41 : 32 : 27 equilibrium mixture of D-glucitol, D-mannitol and L-iditol was achieved. More recently, van Es and co-workers reported the synthesis of II by IS isomerisation over Ru/C, leading to the same equilibrium distribution of the three

isomers²¹. Again, high H₂ pressure (40 bar) and temperature (220 °C) were necessary to reach equilibrium; and increasing the initial pH from 7 to 10 was key to improve the yield: the mass loss decreased from 25 % to 6.4 %. The observed byproducts such as linear diols or volatile alcohols were ascribed to hydrodeoxygenation of IS, which, in turn, could be attributed to acid-catalysed dehydration. Pd/C, Pt/C, Rh/C and Au/C were not active, while Ru/Al₂O₃ and Ni/SiO₂ showed slightly lower activity compared to Ru/C.

Isohexide isomerisation was also observed as a competing reaction in the homogeneously-catalysed, direct amination of IS by Matthias Beller et al. using inorganic ruthenium complexes with pincer-type phosphine ligands in *tert*-amyl-alcohol²⁴. This possibility was further explored by Dieter Vogt et al.²⁵ who recently reported synthesis of II from isomerization of IS under a biphasic (homogeneous) catalytic system which allowed the recovery and reuse the catalyst for an industrially viable, large-scale production of II²⁶. Surprisingly, in stark contrast to the heterogeneous catalytic system based on Ru/C, the reaction in homogeneous phase could be conducted without needing any exogenous H₂.

In the following, results of the *ab-initio* study of the isomerization of IS have been reported which help rationalize the peculiar role of H₂. The same was also observed by our experimental collaborators (Figure 3.1).

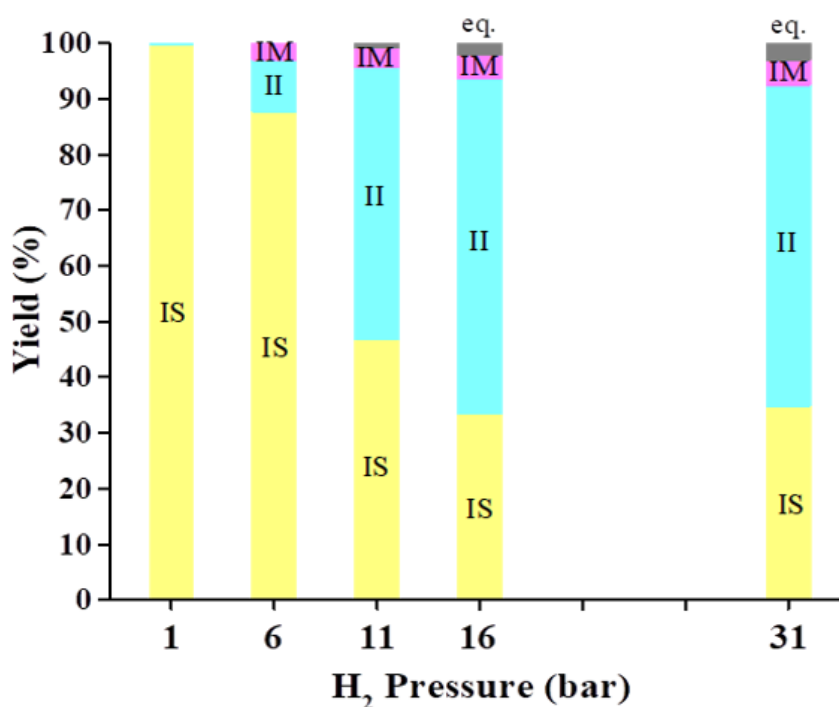


Figure 3.1: Product distribution and mass loss under different H₂ pressures. Reaction conditions: 1 g IS, 15 mL H₂O, pH 10, 0.05 g Ru/C (5wt %), 200 °C, 1 h²⁷.

3.2 Computational Details

Periodic Density Functional Theory as implemented in the Vienna Ab-initio Simulation Package (VASP)²⁸ was used to investigate the reaction pathways for the isomerisation of (*endo*, *exo*)-OH functional groups present in IS. Electronic energies were approximated at the GGA level using the Perdew-Burke-Ernzerhof (PBE)²⁹ exchange-correlation functional with dDSc dispersion correction³⁰. Ion-electron interactions were treated using Projector Augmented Wave (PAW)^{31;32} formalism with 850 eV cutoff for the augmentation charges and plan-wave basis set was truncated at 500 eV. The Ru catalyst was modelled by a 4 layered thick p(4 × 4) slab of Ru(0001) surface. The slab was cleaved from bulk Ru following a full optimization of the bulk which resulted in lattice parameters of $a = 2.702 \text{ \AA}$ and $c/a = 1.578$ in good agreement with the experimental values³³. The bottom two layers were kept frozen to their bulk positions; all other degrees of freedom were allowed to relax until all forces were less than 0.01 eV/\AA . The cutoff for the electronic self-consistency cycle was set to $1 \times 10^{-7} \text{ eV}$. All calculations for slab or slab-adsorbate systems used a Gamma-centered $5 \times 5 \times 1$ k-point mesh to sample the Brillouin zone. Second order Methfessel-Paxton smearing scheme was employed with a smearing width of 0.2 eV. To minimize the interactions between different periodic images of the system in the direction normal to the slab, a minimum vacuum gap of 25 Å augmented by a dipole correction to both energy and forces in that direction was employed.

Thermal and entropic contributions to the total energy were estimated under the harmonic approximation by calculating the normal modes for the adsorbate part of all reaction species using the central finite differences method with step size of 0.01 \AA . All normal modes (those below 50 cm^{-1} were rescaled to 50 cm^{-1}) were used to calculate the ZPVE and other thermal and entropic contributions considering ideal gas behavior.

The molecular species were optimized at Gamma point in a $20 \times 20 \times 20 \text{ \AA}^3$ cubic box. Due to polarity of the molecules, dipole correction was used in all directions. A reduced smearing width of 0.02 eV was employed for molecular species. The vibrational, rotational and translational contributions to the enthalpy and entropy were calculated under harmonic ideal gas approximation taking into account proper symmetry of the molecules.

3.3 Gas-Phase Geometry of Molecules

DFT and post-HF methods are well suited for the study of gas-phase properties of molecular species. In particular, the ground-state geometry and electronic energy can easily be obtained from a simple geometry optimization which can be followed by a frequency calculation to

determine the normal modes which provide the thermal and entropic contributions to the total energy. Figure 3.2 gives the geometries of the most stable conformers of isohexide isomers and the corresponding (mono, di)ketones in the gas phase using the computational setup described in the previous section. IS and IM were found to have two stable conformers: one with puckered ring skeleton (IS-a, IM-a) and the other with slightly flat ring structure (IS-b, IM-b), the effect being stronger for IM where both furan rings can be flat as opposed to IS where only one ring containing *endo*-OH group undergoes flattening. The latter flat topology allows a closer approach between H of *endo*-OH groups and the corresponding ring ethers in the adjoining ring indicated by the shorter O—H—...—O distances shown in Å. Furthermore, in contrast to the structure of IS reported in the literature, the optimal position for the *exo*-OH group was found to be below the ring skeleton which allows a better hydrogen-bonding-like interaction with the ether of the same furan ring. This below-the-ring position of *exo*-OH precludes for II the flat ring conformer observed for IS and IM. Furthermore, both IM and II have a C_2 symmetry in their most stable configuration as demonstrated by the same O—H—...—O distances for their different conformers.

The corresponding monoketones (MK) are shown as *endo*-OH-MK (which may result from dehydrogenation of IS or IM) and *exo*-OH-MK (derived from either IS or II). Further dehydrogenation of the either MK results in diketone which is a symmetric C_2 molecule.

3.4 Mechanistic Investigation by Periodic DFT

To understand why a high H_2 pressure is required for IS isomerisation, a computational mechanistic study was carried out. Relying on the experimental observation of MK traces found in the reaction, IS isomerisation is assumed to proceed *via* a sequential dehydrogenation-rehydrogenation mechanism, i.e. at any given time only one of the (*endo*, *exo*)-OH groups is dehydrogenated leading to the corresponding MK which is immediately rehydrogenated to give the (non-)isomerised product. This assumption precludes formation of the corresponding diketone on the surface, and is well justified based on the experimental observation of no di-ketone species detected in the reaction mixture. We further restricted our analysis to a reaction path starting from O—H scission followed by C—H bond breaking to form the chemisorbed MK (so called *alkoxy* pathway). The alternative route starting from C—H bond breaking followed by O—H scission (*alkyl* pathway) was dismissed based on previous studies of ketone hydrogenation³⁴ and alcohol dehydrogenation³⁵. These studies demonstrated the preference for the *alkoxy* pathway on oxophilic metals in terms of (i) difficulty of C—H bond breaking and (ii) the immense stability of the alkoxy intermediates resulting from initial O—H bond breaking step leading to a very exoenergetic change. Assuming an *alkoxy* pathway, the rehydrogenation of the MK species in the second half of the catalytic cycle was investigated starting exclusively at the α -C of the carbonyl group, giving alkoxy intermediates which are

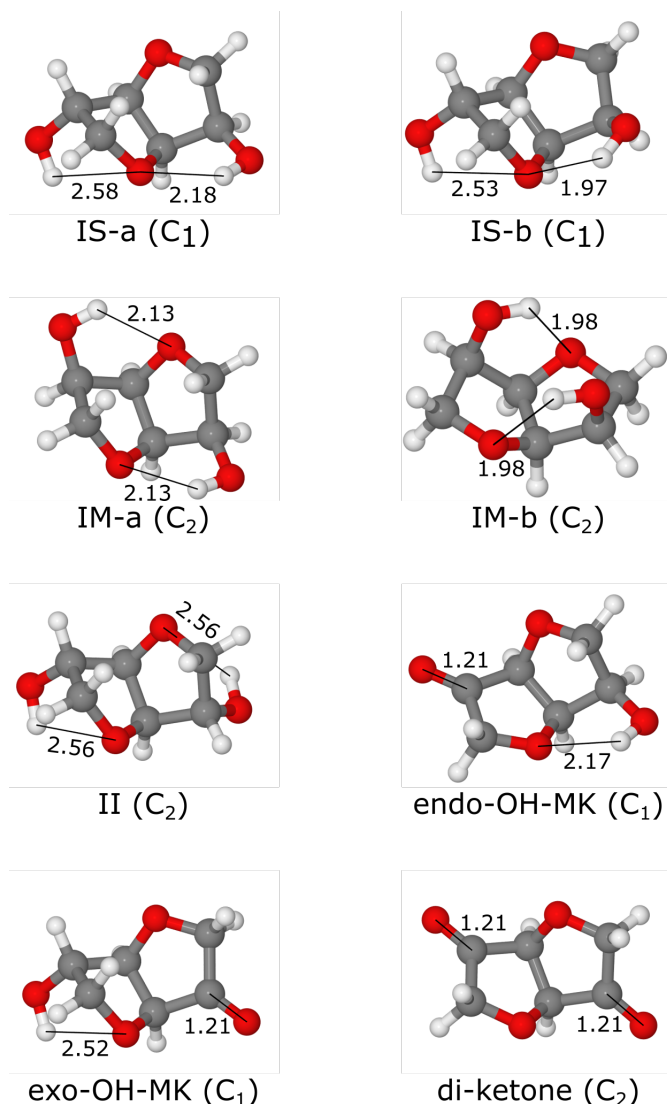


Figure 3.2: The most stable geometry of isohexide isomers and the corresponding (mono, di)-ketones. The numbers give the distances in Å and the symbol in parenthesis is the symmetry point-group of the molecule. Color scheme: red: O; gray: C; white: H

further hydrogenated to complete the catalytic cycle. However, the MK intermediates have to be rehydrogenated at α -C from the side opposite to that of the initial dehydrogenation to invert the configuration and give way to the isomerised product. Furthermore, the calculations of the isomerisation pathway were performed both with and without the presence of co-adsorbed H atoms to explicitly account for high H_2 pressures needed in the reaction and to make a comparison between high H_2 and no H_2 cases.

3.4.1 Adsorption of isohexides

Adsorption of IS on the catalyst surface is the branching point towards the formation of II (hereby referred to as **Endo2Exo** pathway) or IM (**Exo2Endo** pathway). Figure 3.3 shows different adsorption modes of isohexides depending on whether adsorption takes place mainly *via* the (*endo*, *exo*)-OH. In its most stable adsorption mode, IS lies parallel to the surface with the O atom of the *endo*-OH and the ether-O of the adjoining ring interacting with two neighbouring Ru atoms (Figure 3.3, **IS_{Endo}**). This adsorption mode was found to be much more stable ($G_{\text{ads}} = -26 \text{ kJ.mol}^{-1}$) than a perpendicular adsorption mode where only interaction with the surface is through the *endo*-OH ($G_{\text{ads}} = +16 \text{ kJ.mol}^{-1}$, Figure 3.3 (**b**)), indicating that the ether contributes a large part of the adsorption energy. Indeed, the corresponding distances show that the ether-O atom is closer (2.28 Å) to the surface than the O of the *endo*-OH group (2.32 Å). This slight tilt towards the ether-O also favours a weak agostic interaction between the H of the unbound *exo*-OH and the Ru surface^{36;37}; the corresponding H— — — Ru surface distance (2.60 Å) is indicated in blue in Figure 3.3. Adsorption through the *exo*-OH of IS (Figure 3.3, **IS_{Exo}**) involves the O atom of the *exo*-OH and the ether-O of the same ring lying on top of two neighbouring Ru atoms. Unlike **IS_{Endo}**, this adsorption mode is rather constrained and requires a distortion of the *exo*-OH from its most stable gas phase orientation which makes **IS_{Exo}** 14 kJ.mol⁻¹ less stable than **IS_{Endo}**. A slight distortion from the gas phase orientation is also observed in the H atom of the unbound *endo*-OH which points away from the corresponding ring ether to better point towards the surface, thus generating a slightly favourable, albeit weaker than that in **IS_{Endo}**, agostic interaction (3.01 Å). We emphasize here that the adsorption through ether-O, be it of the same ring or the adjoining ring, was found to be characteristic to all the reaction species involved in the isomerization; and a comparison of the **IS_{Endo}** and **IS_{Exo}** adsorption modes clearly demonstrates that better interaction is achieved when ether of the adjoining ring is involved in bonding with the surface.

II has both OH groups in *exo* position and thus exhibits an adsorption mode similar to **IS_{Exo}** (Figure 3.3, **II**). Likewise, IM has both OH groups in *endo* position and thus exhibits adsorption mode similar to **IS_{Endo}** (Figure 3.3, **IM**). Notably, the unbound *endo*-OH group in **IM** adsorption mode lies farther away from the surface in a hydrogen-bonding-like interaction with the ether-O of the adjoining ring, precluding any agostic interaction with the surface. This in turn makes the adsorption of IM less strong compared to that of IS in the similar **IS_{Endo}** mode. Finally, it is imperative to remark that although the *intrinsic error* of PBE cohesive energies is $\sim 30 \text{ kJ.mol}^{-1}$ ³⁸, the relative energies of the reaction intermediates and transition states do lend themselves to a quantitative prediction within a reasonable accuracy.

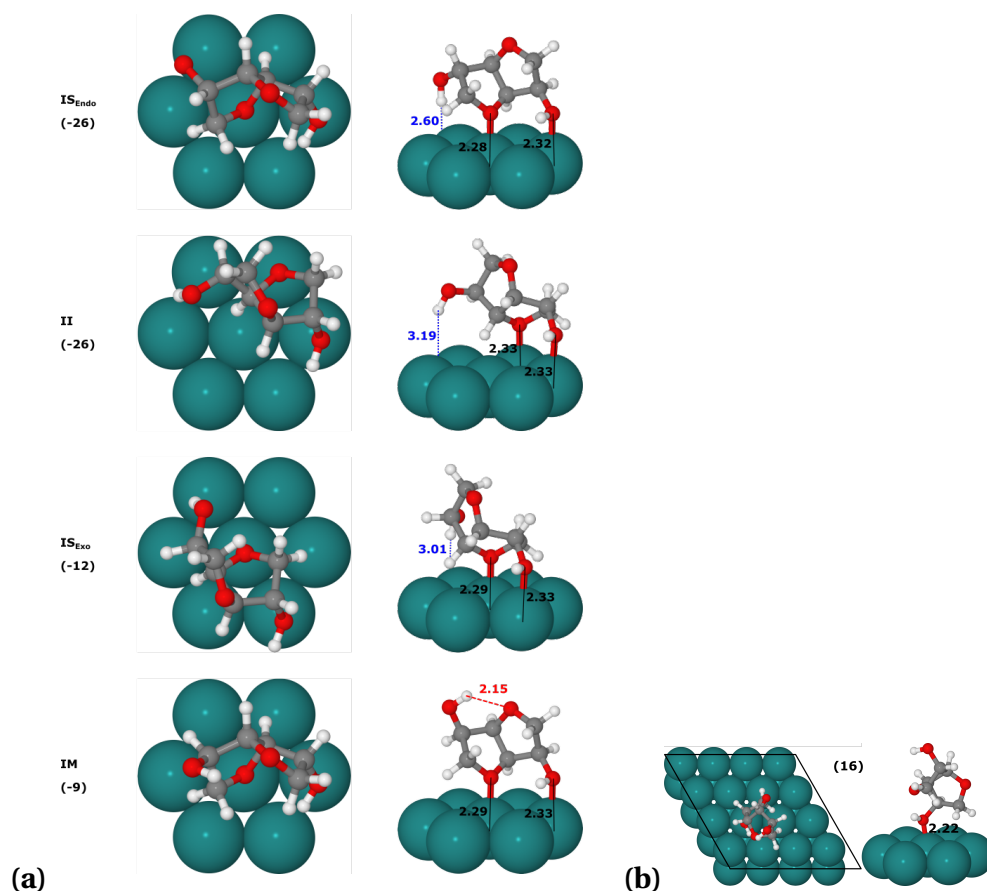


Figure 3.3: **(a)** Adsorption modes of isohexides on Ru(0001) surface and **(b)** the vertical adsorption mode of IS. Blue dashed lines indicate favourable agostic interaction with the surface; red dashed line represents hydrogen-bonding interaction. Main distances are provided in Å; the numbers in parenthesis are the Gibbs free energy of adsorption of the corresponding isomers in $\text{kJ}\cdot\text{mol}^{-1}$ at 160 °C temperature and 1 atm pressure. Colour scheme: green: Ru; red: O; gray: C; white: H

3.4.2 Free energy profile in the limit of a low H surface concentration

To investigate the free energy reaction profile in the limit of low H surface concentration, corresponding to a low H_2 pressure or concentration in the reaction mixture, all reaction species (RS) were optimized on a separate, clean $p(4\times 4)$ slab. The chemisorbed H atoms resulting from initial dehydrogenation were allowed to relax on separate slabs thereby making it zero co-adsorption case. The optimized geometries for all the relevant reaction intermediates (RI) and transition states (TS) are provided in Figure 3.4, whereas Figure 3.5 gives a plot of the free energy profiles computed for the two reaction pathways, **Endo2Exo** and **Exo2Endo**.

The two pathways follow the same sequence of steps, and differ only in the nature of the

3.4. Mechanistic Investigation by Periodic DFT

OH group that is isomerised. The first step corresponds to the initial adsorption of IS in **IS_{Endo}** (**Endo2Exo**) or **IS_{Exo}** (**Exo2Endo**) mode (Figure 3.3). The initial adsorption modes then serve as reactants for the first O–H scission TS, denoted **TS1(OH)** in Figure 3.4 and Figure 3.5. The relative stability of **TS1(OH)** for both pathways agrees well with the relative stability of **IS_{Endo}** and **IS_{Exo}** modes, the reactants for this TS. This translates into the fact that even though **TS1(OH)** for **Exo2Endo** pathway lies higher than **TS1(OH)** for **Endo2Exo** pathway by ~ 16 kJ.mol⁻¹, the overall barrier for this transformation is roughly the same for both pathways. The **TS1(OH)** leads to very stable alkoxy intermediates, **Alkoxy1**, with an adsorption pattern similar to **IS_{Endo}** and **IS_{Exo}** adsorption modes, only difference being the adsorption location of alkoxy O which sits atop a hollow fcc site instead of a Ru atom (Figure 3.4). This three-fold hollow-site adsorption is typical of alkoxy species on closed-pack Ru(0001) and renders them their stronger adsorption compared to their corresponding reactants. The relative energy difference of **Alkoxy1** intermediates involved in both pathways is 21 kJ.mol⁻¹ which is higher than the respective energy difference between **IS_{Endo}** and **IS_{Exo}** adsorption modes (14 kJ.mol⁻¹). The main source of this energy difference between the two **Alkoxy1** intermediates can be ascribed to the aforementioned difference of stability provided by the two different ethers (same furan ring or the adjoining ring) involved in the adsorption. Overall, the formation of alkoxy intermediates is a highly exoenergetic transformation which should happen spontaneously, given the very low activation barriers (42-44 kJ.mol⁻¹).

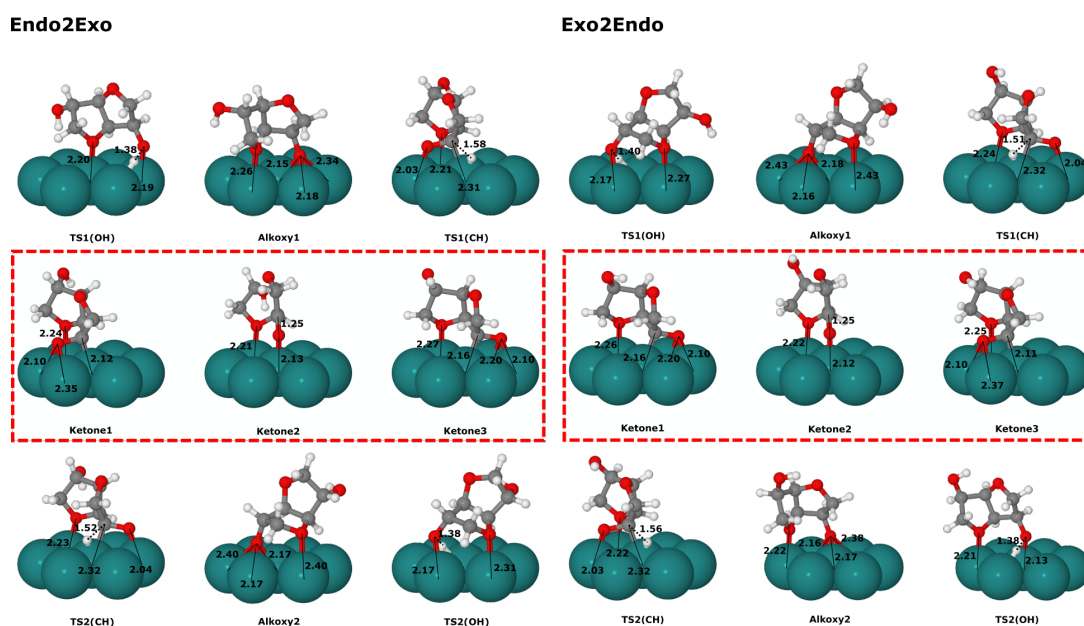


Figure 3.4: Optimized structures along the **Endo2Exo/Exo2Endo** pathways. Main distances are provided in Å.

The **Alkoxy1** intermediates further undergo C–H scission *via* **TS1(CH)** TS to produce first MK intermediates named (**Ketone1**). The structure of **TS1(CH)** involves, in addition to the

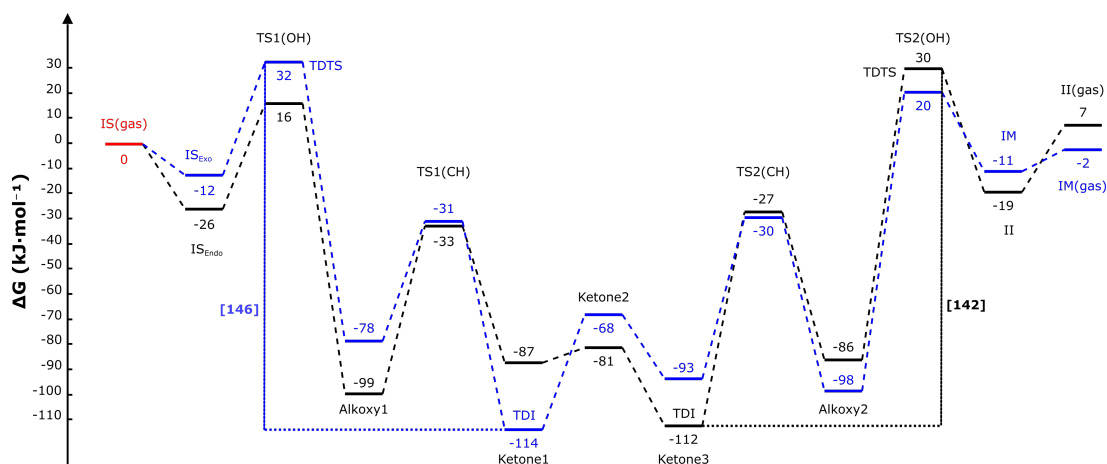


Figure 3.5: Gibbs free energy profiles for IS isomerisation. The black line represents **Endo2Exo** pathway; blue line **Exo2Endo** pathway. The energy spans are highlighted with vertical dotted line. The entropic and enthalpic contributions were calculated only for the adsorbates using an ideal gas harmonic approximation at 160 °C temperature and 1 atm pressure.

ether–Ru interaction observed in previous RS, C=O group lying on a bridge site in a di- σ fashion³⁹ either in front (**Endo2Exo**) or back (**Exo2Endo**) of the ring skeleton. This tridentate adsorption mode is necessary for the α -C to be close enough to the surface to lose its H atom. Notably, the ether-O–Ru interaction occurs through the ether of the adjoining ring for **TS1(CH)** TS of both **Endo2Exo** and **Exo2Endo** pathways, which explains their relative stability signified by very similar values on the free energy profile. However, the reactants for this transformation, i.e. **Alkoxy1**, must undergo strong distortion from their very stable three-fold, hollow sites to achieve the favourable topology for C–H bond breaking. This results in higher activation barriers for this second C–H bond-breaking TS, **TS1(CH)**, compared to the first O–H bond-breaking TS, **TS1(OH)**. The barrier involved in **TS1(CH)** is higher by ~ 20 kJ.mol⁻¹ for the **Endo2Exo** pathway, mainly, because the corresponding **Alkoxy1** intermediate is much more stable compared to the **Alkoxy1** in **Exo2Endo** pathway.

Monoketone RI **Ketone1** are the immediate products of the C–H bond-breaking step and thus manifest the same adsorption structure as their corresponding **TS1(CH)** TS. As mentioned before, to isomerise the respective OH group, the rehydrogenation of MK must happen on the side opposite to that of the first C–H scission TS. **Ketone1** does not facilitate this required directionality for isomerization and must undergo a rotation around the α -C. We believe this rotation of the C=O group goes through another MK RI, namely **Ketone2**, that is chemisorbed through the O of C=O and ether of the adjoining ring, similar to the **IS_{Endo}** mode of IS. This transformation from **Ketone1** to **Ketone2** is expected to be an activated process, however, we expect the relevant activation barriers to be much smaller compared to other bond-breaking barriers involved in the overall pathway. Moreover, all of these MK RI could eventually develop

3.4. Mechanistic Investigation by Periodic DFT

a thermodynamic equilibrium which would dictate their corresponding distribution in the reaction mixture.

The **Ketone2** RI displays the top ($\eta_1\mu_1$) adsorption mode³⁹ of carbonyl group and is more stable in **Endo2Exo** case for quite the similar reasons that make **IS_{Endo}** adsorption mode more stable than the **IM** adsorption mode (Figure 3.3). In **Ketone2** intermediate, the α -C is too far from the surface to undergo the subsequent rehydrogenation, hence, they have to move to a more favourable di- σ adsorption topology of either **Ketone1** or **Ketone3**. **Ketone3** intermediates are chemisorbed through the right face of the C=O bond and lead to the isomerized product by subsequent rehydrogenation. The MK intermediates are highlighted in red rectangle in Figure 3.4 and their interconversion is key to IS isomerisation and is discussed in detail in the following section. It is worth mentioning that this rotation of the C=O around α -C is indicative of the *direct-hydride-exchange* mechanism hypothesized in ref²². However, they premise this mechanism on the formation of a carbenium ion on the surface resulting from the heterolytic cleavage of C–H bond. Our calculations clearly lack evidence of any such carbenium ion formation on the surface. The most likely configuration for a carbenium ion would be similar to that of **Ketone2**, however, **Ketone2** intermediates manifest properties (C=O bond length, charge on α -C etc.) quite similar to those of corresponding gas-phase MK. The overall transformation from **Alkoxy1** to **Ketone3** is exoenergetic for both pathways.

In the second half of the catalytic cycle, **Ketone3** RI undergo rehydrogenation preferentially at the α -C to produce **Alkoxy2** intermediates, which feature an inverted symmetry at the α -C compared to their **Alkoxy1** counterparts. This transformation involves the C–H bond-making TS, labelled as **TS2(CH)** in Figure 3.4 and Figure 3.5. Subsequent hydrogenation of **Alkoxy2** generates either II or IM. This requires crossing a very high energy activation barrier through the O–H bond-making TS, **TS2(OH)**, and is highly endoenergetic for both pathways. The eventual desorption of IM and II completes the catalytic cycle and leads to the isomerised products.

Overall, both pathways feature similar free energy profiles with the highest-lying TS corresponding to the *exo*-O–H scission/formation (**TS1(OH)** in **Exo2Endo** and **TS2(OH)** in **Endo2Exo**) and the most stable RI being the chemisorbed MK which has the C=O group at the back of the ring skeleton (**Ketone1** in **Exo2Endo** and **Ketone3** in **Endo2Exo**). The first and last points on the free energy profile in Figure 3.5 correspond to the relative stability of the three isomers in the gas phase which is qualitatively wrong at the adopted PBE-dDSc level of theory and more accurate post-HF treatment is needed to reproduce the observed experimental distribution of the three isomers in the reaction. At the current level of theory considered, assuming that isomerisation of IS into II or IM is an athermic process, the energy span can be calculated as the difference of the free energy of TOF-determining transition state (TDTS) and TOF-determining intermediate (TDI)⁴⁰ both of which are highlighted on the profiles in Figure 3.5. The similar energy span for **Endo2Exo** and **Exo2Endo** pathways,

142 and 146 kJ.mol⁻¹, respectively, agrees well with the experimental observation that there is no prominent difference in the reactivity of (*endo*, *exo*)-OH groups in IS as is evident from the experimental kinetic profiles of the isomerization reaction starting from different isomer substrates shown in Figure 3.6.

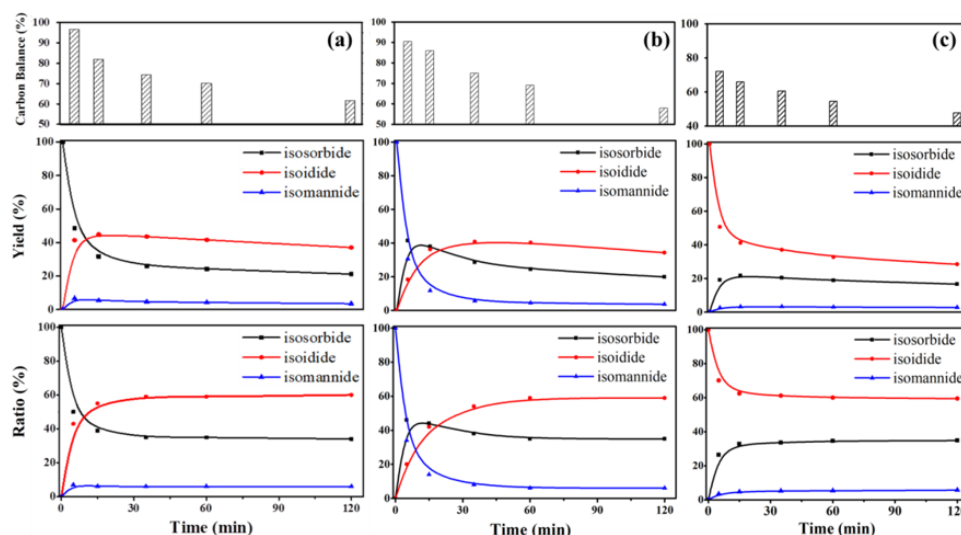


Figure 3.6: (Top) Carbon balance, (middle) yield and (bottom) ratio of isomers upon isomerisation of: (a) IS, (b) IM and (c) II. Reaction conditions: 1 g substrate, 15 mL H₂O, 0.05 g Ru/C (5wt%), 31 bar H₂, 200 °C.²⁷

3.4.3 Rotation of MK and role of ring ethers

The adsorption of MKs is discussed here in detail owing to their potentially pivotal role in the isomerisation mechanism elucidation. All MK RI adsorb on the surface through their C=O group in a top or di- σ fashion and the ether-O of the adjoining ring. We suspect that this adjoining-ring ether O, which is uniquely present due to the bicyclic nature of IS and its isomers, is suitably positioned relative to the C–O group not only to stabilize the MK, but also to aid in their proposed interconversion on the surface: the ether-O potentially acts as the anchor point of **Ketone1** to **Ketone3** rotation. To confirm this hypothesis, we looked at the dehydrogenation-rehydrogenation profile of a simpler molecule, 3-hydroxytetrahydrofuran (**3-OH-THF**), which is just one 5-membered ring of IS. Although **3-OH-THF** has a ring ether, its position relative to the OH group does not stabilize the ketone intermediates. Indeed, the most stable ketone intermediate for **3-OH-THF** has the ring ether pointing away from the surface and the only interaction with the surface is *via* the C=O group in a di- σ fashion (Figure 3.7). Consequently, the MK intermediates of IS are more strongly adsorbed compared to those of **3-OH-THF** by >30 kJ.mol⁻¹ (Figure 3.8). Owing to this strong adsorption, MK RIs probably act as a bottleneck along the isomerisation pathway, and an external H₂ pressure is required to

3.4. Mechanistic Investigation by Periodic DFT

push them out of this bottleneck. This was further confirmed experimentally by a catalytic test performed in the absence of H_2 using IS and **3-OH-THF** as substrates. While IS was found to be unreactive (no isomerisation, no production of (di, mono)ketones), **3-OH-THF** was reactive and a significant amount of ketone was detected after 2 h. In light of these results, we understand that IS is a unique substrate whose bicyclic nature combined with the presence of ethers in each ring contributes to its lower reactivity in the absence of H_2 .

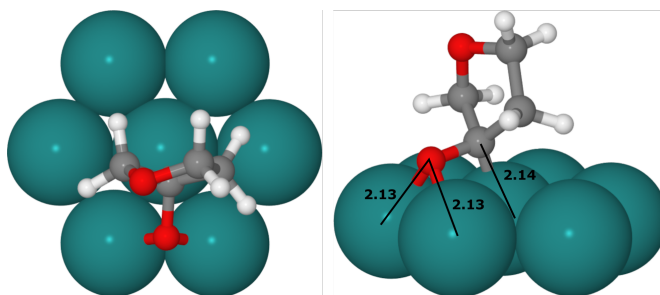


Figure 3.7: Most stable adsorption structure of ketone resulting from 3-OH-THF dehydrogenation. The $C=O$ group lies on hcp hollow site in a di- σ fashion with the ring ether-O away from the surface.

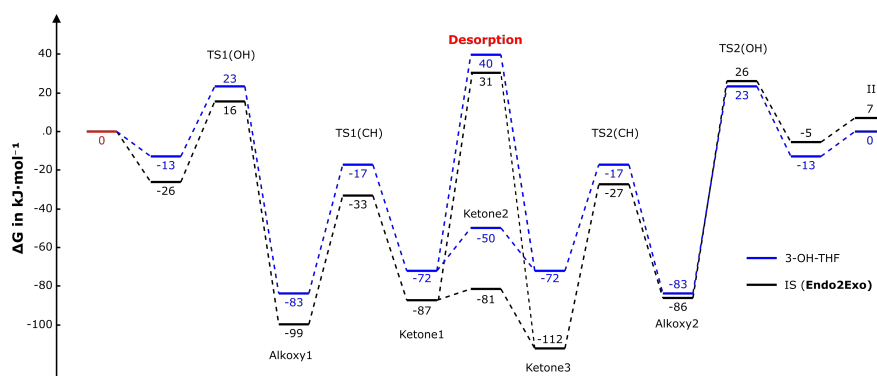


Figure 3.8: Comparison of dehydrogenation-rehydrogenation pathways of IS (**Endo2Exo**) and **3-OH-THF**. The ketone intermediates of **3-OH-THF** lie higher than those of IS by almost $40 \text{ kJ}\cdot\text{mol}^{-1}$. The desorption values represent the full desorption of ketone and hydrogen molecule leaving behind clean catalyst surface. The pathway for **3-OH-THF** is mirror symmetric around the desorption point i.e. **TS1(OH)** and **TS2(OH)** are same for **3-OH-THF**

3.4.4 Free energy profile in presence of a high H_2 pressure

The pristine Ru(0001) surface considered above to model the catalyst surface can be regarded as a hypothetical scenario representing very low H_2 pressure. Under an external H_2 pressure, the catalyst surface is expected to be covered by H species to varying extent. H adsorbs strongly on the Ru(0001) surface, preferentially on an fcc hollow site from 1 H atom ($G_{\text{ads}}/\text{atom} = -36 \text{ kJ}\cdot\text{mol}^{-1}$) up to a monolayer (ML) coverage ($G_{\text{ads}}/\text{atom} = -29 \text{ kJ}\cdot\text{mol}^{-1}$). Figure 3.9 shows the most stable distribution of H atoms on Ru(0001) at each level of coverage from 1 H atom up

to 1 ML, while Figure 3.10 shows the plot of average Gibbs free energy of adsorption at each coverage.

As a natural next step, the free energy profiles in Figure 3.5 were recomputed in the presence of explicitly co-adsorbed H. Two coverage levels of H were considered, $\theta_H = 0.5$ ML (8 H atoms on p(4x4) slab) and $\theta_H = 0.75$ ML (12 H atoms on p(4x4) slab). The new model for the catalyst surface was chosen to be the pristine Ru(0001) slab considered in the previous case ($\theta_H = 0.0$ ML) covered with most stable distribution of H at chosen coverage. Starting from the most stable adsorption geometries on the pristine surface (Figure 3.4), all the RS were reoptimized at the same level of theory in the presence of 8 or 12 H atoms. A systematic approach was employed to find the most suitable adsorption sites for the co-adsorbed H atoms around RS which is briefly outlined below.

Starting from the most number of H atoms that could be accommodated on fcc hollow sites around the given RS without inducing any overlaps with the adsorbate, H atoms were removed one by one to find the most stable co-adsorption geometry at each coverage level. All possible combinations of removing one H atom from a given co-adsorbed geometry were checked i.e. to find the best co-adsorbed geometry with 12 H atoms, we started from a structure with 13 co-adsorbed H atoms and checked for 13 possible combinations ($^{13}C_{12} = ^{13}C_1$). Lower level of theory (Gamma-point optimization with less strict criteria for force and electronic consistency cycle) was employed to scan the different possibilities and the adsorbate part of previously optimized RS (Figure 3.4) was kept fixed. An alternative approach could be to start with a surface preadsorbed with H up to a certain coverage and then allow the reactants to adsorb on that. However, this approach is quite difficult to realize in static calculations as adsorption of the reactants would involve rearrangement of pre-adsorbed H atoms to make way for the incoming reactant species. This approach would be even less suited for a higher coverage of pre-adsorbed H as reactants would need to displace large number of H atoms to find themselves a big enough pocket of free surface atoms to which they can chemisorb. That is also the reason why the highest θ_H we considered was 0.75 ML because for higher coverage there is no chemisorption between reactants and the metal surface. This former approach could, however, be implemented using dynamic techniques which were not considered in this work.

In general, at each θ_H coverage, co-adsorbed H atoms preferred adsorption sites that maximize their distance from the pre-adsorbed RS, in particular, H atoms bind to the Ru atoms which are not directly bonded to the RS. At $\theta_H = 0.5$ ML, enough sites are available for H atoms to adsorb far enough from the RS to cause little to no effect on the 0.0 ML adsorption geometry of RS apart from slightly-elongated O–Ru, ether-O–Ru distances between surface and the adsorbates. Table 3.1 gives the optimized structures for all the RSs of the **Endo2Exo** pathway with 8 co-adsorbed H atoms; and it can be easily visualized that co-adsorbed H atoms try

3.4. Mechanistic Investigation by Periodic DFT

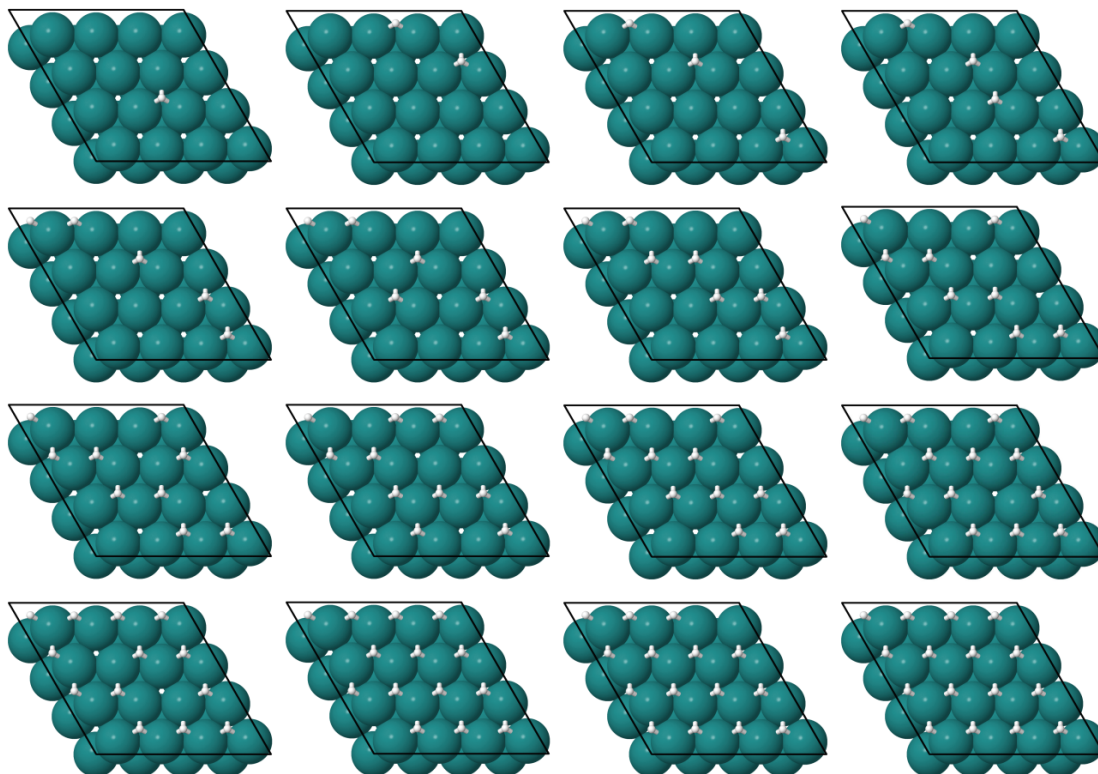


Figure 3.9: Most stable distribution of H on Ru(0001) surface up to 1 ML. H preferentially binds to three-fold fcc hollow sites. The shown distributions were found after checking all possible combinations of given number of H atoms over (4x4) supercell i.e. 16 fcc sites.

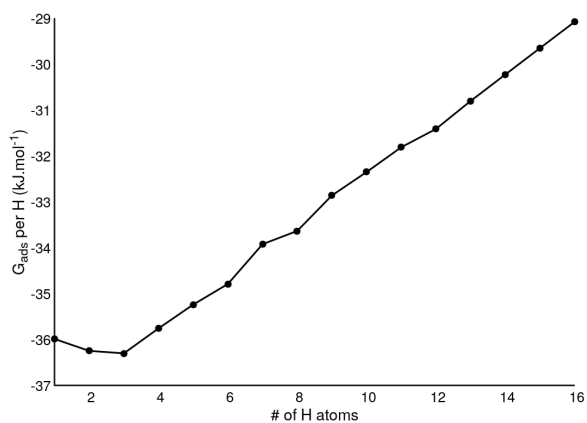
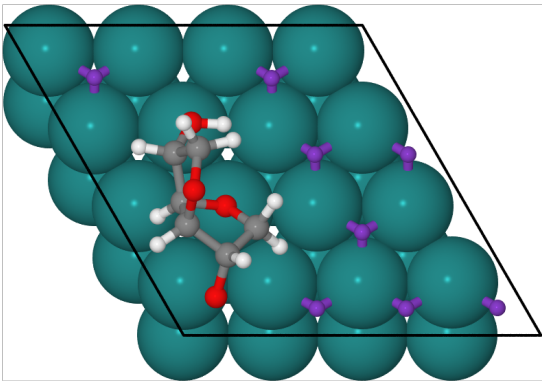
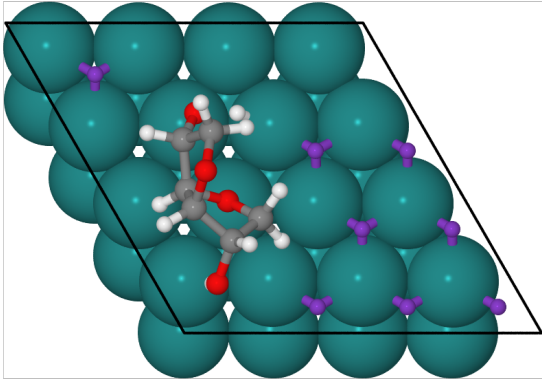


Figure 3.10: Gibbs-free energy of adsorption per H atom on Ru(0001) up to 1 ML relative to a H₂ molecule in the gas phase. Normal modes for the adsorbed H atoms were used to calculate ZPVE and other enthalpic and entropic contributions under harmonic approximation at 160 °C and 1 atm pressure.

to avoid binding to the Ru atoms which are directly bonded to the RS. This is quite easy to achieve for bidentate binding modes of RS like **IS_{Endo}** or **Ketone2**, however, for tridentate binding modes, there are one or two co-adsorbed H atoms that share a Ru atom with the RS e.g. the TS involving transformation of O–H bond. The trend is similar for RS of **Exo2Endo** pathway.

Table 3.1: Optimized structures of RS with 8 co-adsorbed H atoms shown in purple. Just top views are provided to visualize the distribution of the co-adsorbed H atoms around the RS which does not undergo any significant distortion in their corresponding 0.0 ML adsorption geometry.

RS	Structure
IS_{Endo}	
TS1(OH)	

3.4. Mechanistic Investigation by Periodic DFT

Table 3.1: Optimized structures of RS with 8 co-adsorbed H atoms shown in purple. Just top views are provided to visualize the distribution of the co-adsorbed H atoms around the RS which does not undergo any significant distortion in their corresponding 0.0 ML adsorption geometry.

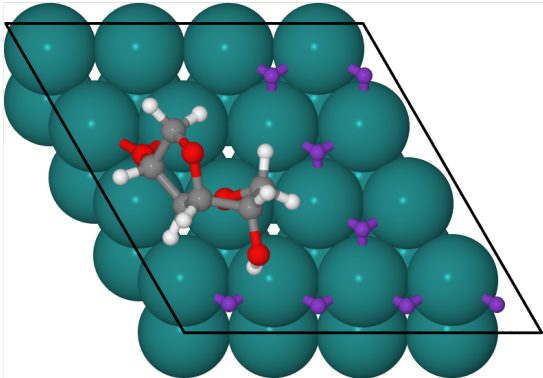
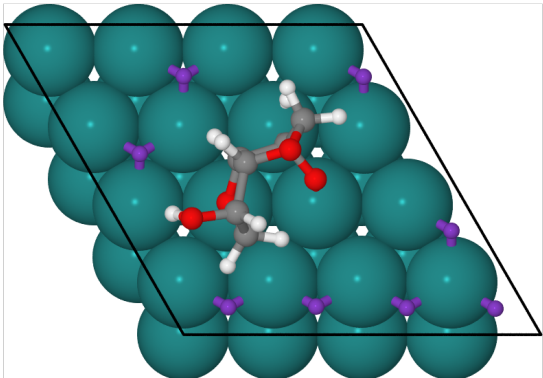
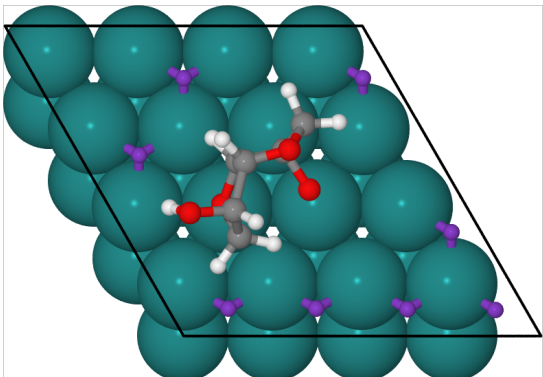
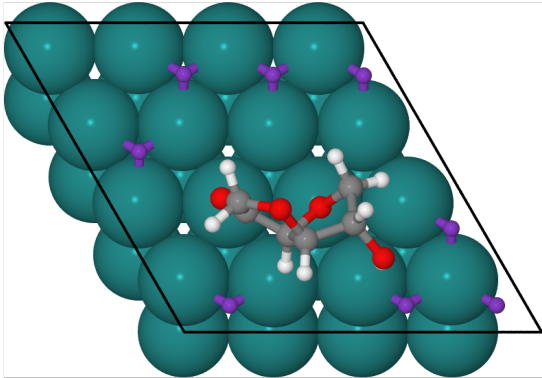
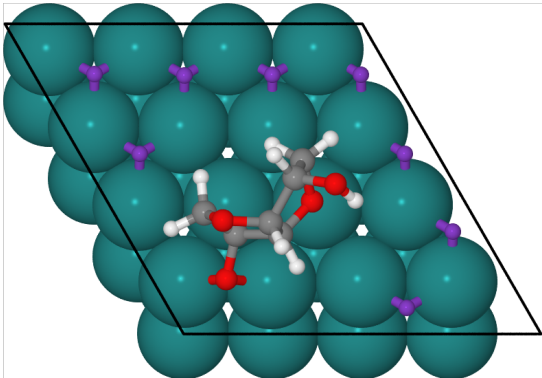
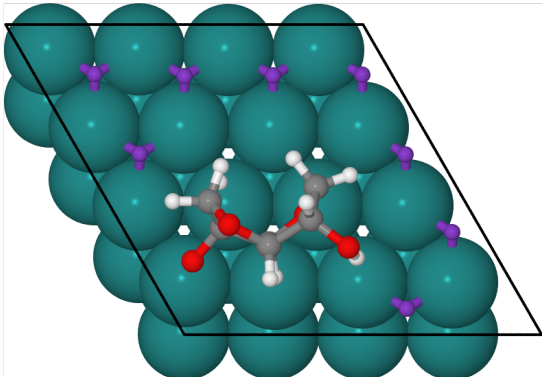
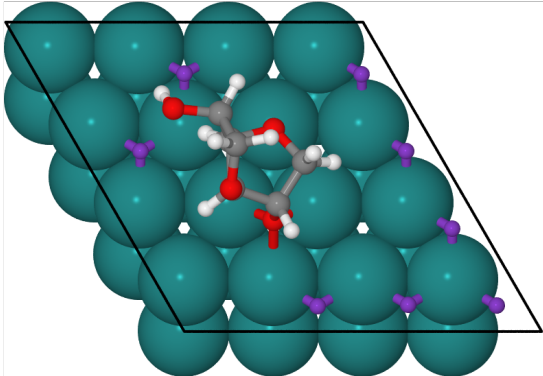
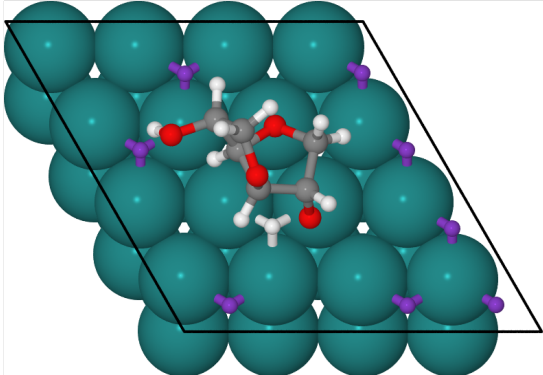
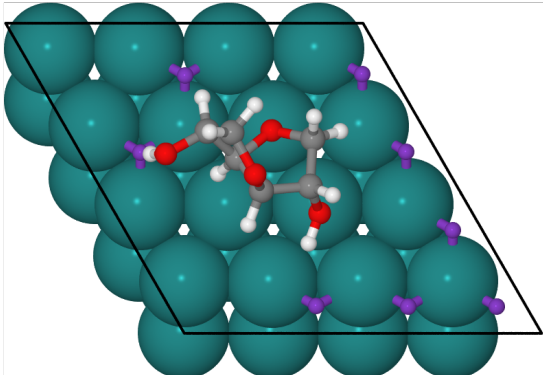
RS	Structure
Alkoxy1	
TS1(CH)	
Ketone1	

Table 3.1: Optimized structures of RS with 8 co-adsorbed H atoms shown in purple. Just top views are provided to visualize the distribution of the co-adsorbed H atoms around the RS which does not undergo any significant distortion in their corresponding 0.0 ML adsorption geometry.

RS	Structure
Ketone2	
Ketone3	
TS2(CH)	

3.4. Mechanistic Investigation by Periodic DFT

Table 3.1: Optimized structures of RS with 8 co-adsorbed H atoms shown in purple. Just top views are provided to visualize the distribution of the co-adsorbed H atoms around the RS which does not undergo any significant distortion in their corresponding 0.0 ML adsorption geometry.

RS	Structure
Alkoxy2	
TS2(OH)	
II	

At $\theta_H = 0.75\text{ML}$, however, H atoms have to adsorb closer to RS due to lack of space, thus inducing significant changes in the 0.0 ML adsorption geometry, especially for those RS having tridentate adsorption modes. For instance, the **Alkoxy2** intermediate of the **Endo2Exo**

pathway moves from a 3-fold fcc site to a 2-fold bridge site (signified by very large 2.52 Å distance in Table 3.2. Another effect observed at each H coverage, more so at 0.75 ML, is the elongation of the ether-O–Ru distance for all species, signifying that RS, when coadsorbed with H, lack the stabilizing effect of ring ethers observed on the pristine surface. This, in turn, could be construed as the destabilising effect of H coadsorption to push the very stable alkoxy and ketone RS up the potential well and thereby push the reaction out of the bottleneck of very stable intermediates.

Table 3.2: Optimized structures of RS for **Endo2Exo** pathway with 12 co-adsorbed H atoms shown in purple. Since at this θ_{H} coverage RS undergo significant distortion from their 0.0 ML geometry, we give the relevant distances as an indication of this distortion. The distances in red correspond to the given O–H or C–H bond-breaking(making) TS.

RS	Structure
IS_{Endo}	
TS1(OH)	
Alkoxy1	

3.4. Mechanistic Investigation by Periodic DFT

Table 3.2: Optimized structures of RS for **Endo2Exo** pathway with 12 co-adsorbed H atoms shown in purple. Since at this θ_{H} coverage RS undergo significant distortion from their 0.0 ML geometry, we give the relevant distances as an indication of this distortion. The distances in red correspond to the given O—H or C—H bond-breaking(making) TS.

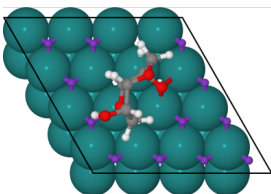
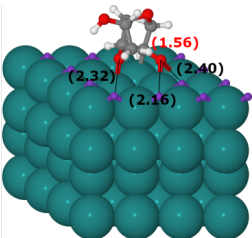
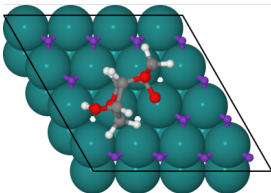
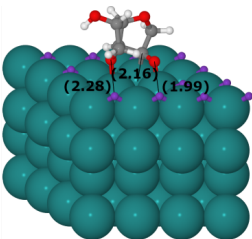
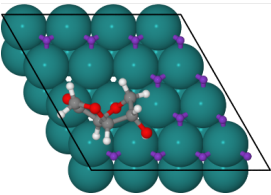
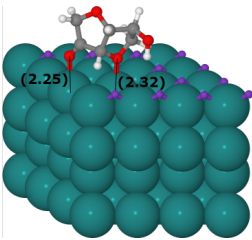
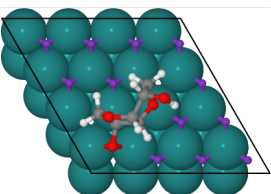
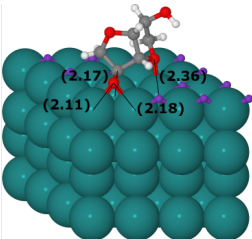
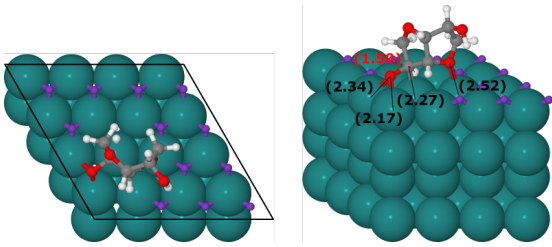
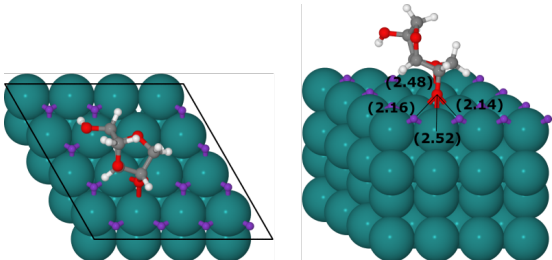
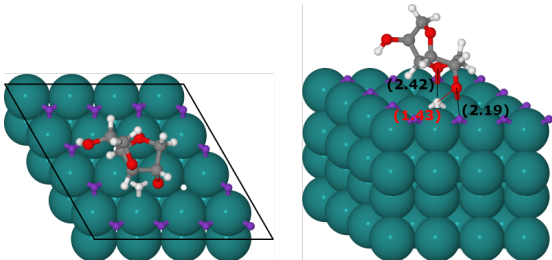
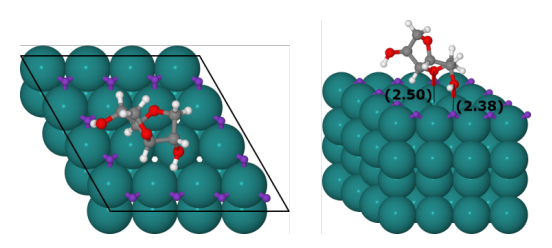
RS	Structure
TS1(CH)	 
Ketone1	 
Ketone2	 
Ketone3	 

Table 3.2: Optimized structures of RS for **Endo2Exo** pathway with 12 co-adsorbed H atoms shown in purple. Since at this θ_{H} coverage RS undergo significant distortion from their 0.0 ML geometry, we give the relevant distances as an indication of this distortion. The distances in red correspond to the given O—H or C—H bond-breaking(making) TS.

RS	Structure
TS2(CH)	
Alkoxy2	
TS2(OH)	
II	

The modified Gibbs-free energy profiles under coadsorption of H are given in Figure 3.11 (**Endo2Exo**) and Figure 3.12 (**Exo2Endo**) for the two pathways considered in Figure 3.5. As can be seen from these profiles, the coadsorption of H pushes up all RS on the energy profile, the effect being more pronounced for some species than the others. In particular, it can

3.4. Mechanistic Investigation by Periodic DFT

be observed that very stable MK RI at 0.0 ML undergo the most drastic destabilising effect: **Ketone3** is destabilized by 38 kJ.mol⁻¹ at 0.50 ML and by 75 kJ.mol⁻¹ at 0.75 ML for **Endo2Exo** pathway. This destabilising effect for MK intermediates is so pronounced that at 0.75 ML, one of the alkoxy intermediates (**Alkoxy1** in Figure 3.11) becomes the most stable one thereby pushing the reaction out of the bottleneck hinted at previously. As expected, the highest-lying TS involving O–H bond transformation is also pushed up in energy, the effect being stronger in going from 0.5 ML to 0.75 ML than that from 0.0 ML to 0.5 ML. This can be explained by the fact that at 0.75 ML, there is not enough space left on the surface to accommodate the incoming H from the O–H bond breaking. Notwithstanding, the highest-lying **TS2(OH)** is destabilized by 19 kJ.mol⁻¹ and 44 kJ.mol⁻¹ at 0.50 ML and 0.75 ML, respectively making the overall span lower than the 0.0 ML case. To rationalize the variable destabilising effect experienced by different species, a deformation-interaction analysis was performed which is outlined below.

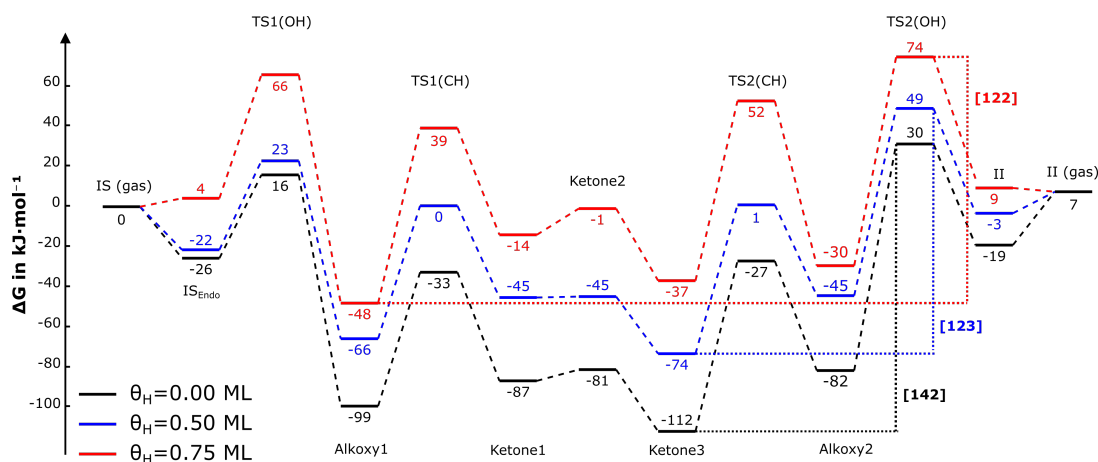


Figure 3.11: Gibbs free energy profiles for the **Endo2Exo** pathway at different surface concentrations of co-adsorbed H. The first and last points represent IS and II in the gas phase along with the Ru(0001) slab at different H coverage: 0.0 ML in black; 0.5 ML in blue; 0.75 ML in red. The two H atoms resulting from initial dehydrogenation were allowed to relax each on a separate H covered surface with 0, 8 or 12 H atoms. The energy spans are indicated by dotted lines. The entropic and enthalpic contributions for the adsorbates (RS + co-adsorbed H) were calculated using an ideal gas approximation at 160 °C temperature and 1 atm pressure.

Deformation-interaction analysis

In Figure 3.11 and Figure 3.12, we could see a clear destabilization experienced by the RS involved in the two reaction pathways when coadsorbed with H. We have investigated the main sources of this destabilization by performing an energy decomposition analysis⁴¹.

Scheme 3.2 gives the overall protocol adopted for the deformation-interaction analysis. The species on the top-left side of the horizontal arrow represent the most stable, fully optimized

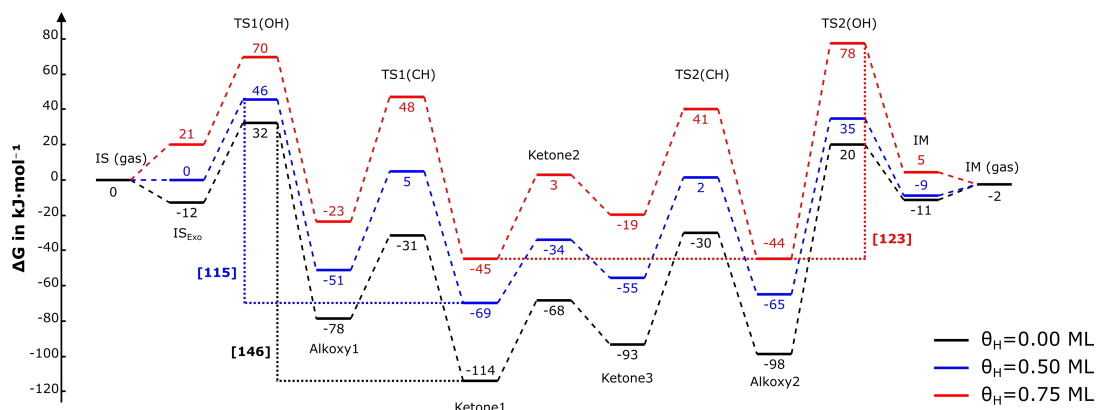
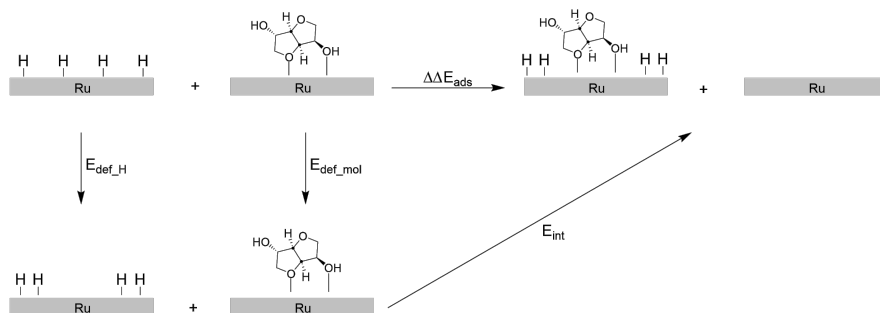


Figure 3.12: Gibbs-free energy profiles for the **Exo2Endo** pathway at different surface concentrations of co-adsorbed H. For details, see the corresponding text or the caption in Figure 3.11.

adsorption geometries of H at 0.5 ML or 0.75 ML coverage, and the RS on separate, pristine slabs with zero coadsorption. The species on the top right signify the fully optimized co-adsorbed geometry of RS along with the corresponding number of H atoms and the pristine, fully relaxed Ru(0001) slab. The corresponding energies for these species are known from our pathway investigation and are given in Figure 3.11 and Figure 3.12. The species at the bottom, however, represent the deformed geometries relative to the fully optimized geometries at the top-left and are obtained after removing the RS or the co-adsorbed H atoms from the fully optimized co-adsorbed geometry shown on top right. The change in adsorption energy upon



Scheme 3.2: Schematic of the deformation-interaction analysis performed for all reaction species at 0.50 ML and 0.75 ML co-adsorbed H.

coadsorption of H, denoted by $\Delta\Delta E_{\text{ads}}$ in Scheme 3.2, can be written as follows:

$$\Delta\Delta E_{\text{ads}} = E_{\text{def}_H} + E_{\text{def}_\text{mol}} + E_{\text{int}} \quad (3.1)$$

where E_{int} represents the interaction energy and $E_{\text{def}_\text{mol}}$, E_{def_H} are the deformation energies corresponding to the deformation experienced by the molecular species and the H atoms co-adsorbed on the surface, respectively. The latter two quantities were calculated by running

3.4. Mechanistic Investigation by Periodic DFT

Single Point energy calculations at the same level of theory as described before.

The calculated contributions to the $\Delta\Delta E_{\text{ads}}$ for four different possible scenarios are plotted in Figure 3.13. At 0.50 ML, the interaction energy is negative for all RS involved in the two pathways indicating a favorable energy change upon coadsorption with H. However, both H and RS have to undergo significant deformation to make the final co-adsorbed geometry possible which makes the overall effect unfavorable thereby destabilizing the RS under coadsorption of H. Notably, the $E_{\text{def_H}}$ is greater for most RS than $E_{\text{def_mol}}$ at 0.50 ML which could be explained by the fact that H atoms tend to adsorb far from each other on pristine Ru(0001) (Figure 3.9) but coadsorption with RS causes them to move closer to make room for the incoming RS. Unfortunately, there is no clear trend and the final result seems to be a combined effect of many different steric and electronic effects a clear understanding of which would need further analysis using advanced energy decomposition techniques.

At 0.75 ML coverage, even the interaction energy is positive for some RS and the corresponding deformation is even stronger which accounts for the large upward push of the corresponding free energy profiles shown in Figure 3.11 and Figure 3.12. At such high coverage of co-adsorbed H, $E_{\text{def_H}}$ and $E_{\text{def_mol}}$ have the similar destabilizing contribution. The positive interaction energy for some RS indicates that 0.75 ML is probably the maximum limit of H coadsorption.

Work Function

Analysis was also performed to look at the possible modification of the Fermi level (E_F) and work function (Φ) of the underlying catalyst model by H/RS adsorption⁴². Figure 3.14 gives the electronic potential for three different catalyst models considered (0.0 ML, 0.50 ML and 0.75 ML) and the IS_{Endo} adsorption mode on pristine surface and Table 3.3 gives the corresponding values for the E_F and Φ . It can be easily seen that the H adsorption does not modify the work function and the Fermi level of the underlying catalyst surface and adsorption of IS only modifies the Fermi level but the over all work function still remains the same. This further strengthens the point made above that the destabilization experienced by the RS is a cumulative effect of many different steric and to a lesser extent electronic contributions.

Table 3.3: The Fermi energy and the work function of the different catalyst models and the IS_{Endo} adsorption mode of IS on pristine Ru(0001) surface.

System	E_F (eV)	E_{vac} (eV)	$\Phi = E_{\text{vac}} - E_F$ (eV)
Ru(0001)	-1.25	3.83	5.08
IS_{Endo}	-0.67	4.34	5.01
0.50 ML	-1.20	3.86	5.05
0.75 ML	-1.17	3.88	5.05

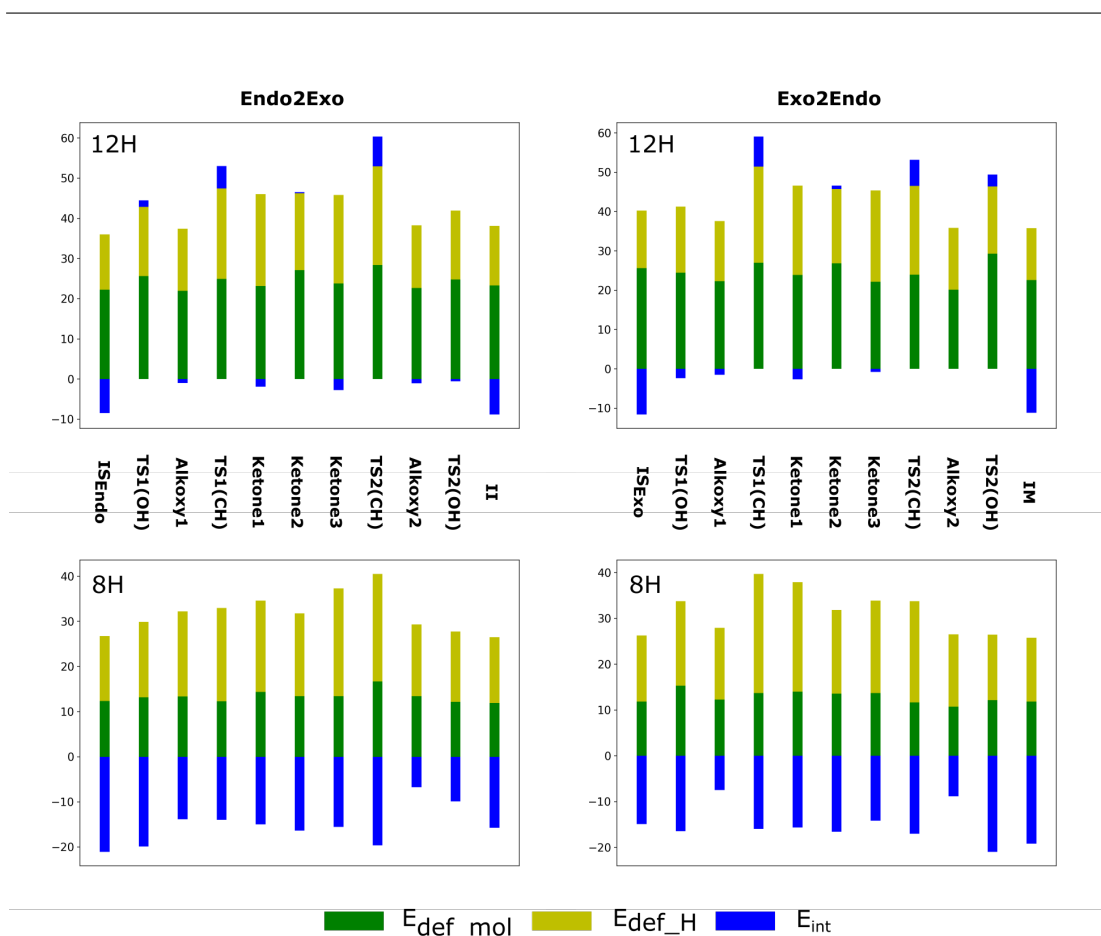


Figure 3.13: Results of the deformation-interaction analysis performed for two pathways under two different coverages of H.

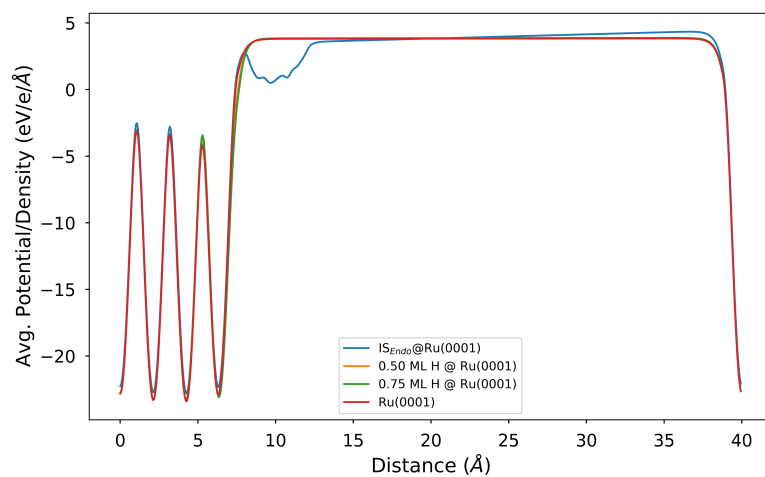


Figure 3.14: Planar-averaged electronic potential for different catalyst models and adsorption of IS in **ISEndo** mode. The potential was extrapolated to vacuum to calculate the corresponding work function.

Finally, for **Endo2Exo** pathway the new spans under H coadsorption are 123 kJ.mol⁻¹ (0.50 ML) and 122 kJ.mol⁻¹ (0.75 ML) which amounts to an increase of 50 in TOF. The similar value of span at the two coverages considered further indicates that the real H coverage in experiment is probably different and somewhere in between 0.50 ML and 0.75 ML (the maximum limit). In principle, under real experimental (T,p) conditions, each RS can have varying H coverage and develop a thermodynamic equilibrium between H on the surface H₂ in the gas phase. This would require investigating the reaction profiles with advanced techniques like Kinetic and Grand-Canonical Monte-Carlo simulations^{43;44} and could be the topic of future studies. Finally, the similar span values for two different pathways is a further indication of the fact that there is no difference in the isomerizing reactivity of the two OH groups present in IS (Figure 3.6).

3.5 Conclusion

We have investigated the thermodynamic reaction profiles for the isomerization of IS using state of the art periodic DFT to help rationalize the crucial role of an exogeneous H₂ pressure required during the reaction. Our calculations show that under no external H₂, the reaction suffers from a bottleneck whereby very stable ketone intermediates stop the progress of the reaction and potentially poison the catalyst. However, under a high pressure of H₂, surface can be partially covered with H atoms along side the reaction species and this coadsorption helps push the very stable reaction intermediates up the free energy potential surface of the reaction thereby pushing the reaction from its bottleneck. Furthermore, the deformation-interaction analysis performed indicates that the destabilizing effect of H coadsorption is irregular for different reaction intermediates and transition states which allows a decrease in over all span of the reaction leading to a ~ 50 times increase in the TOF of reaction. However, no clear pattern is displayed by the energy-decomposition analysis and the over all effect is a cumulative contribution arising from many different steric and to a lesser extent electronic effects. Based on the results of our study, we highlight the need for advanced Monte-Carlo simulations to study the variable H coverage on the surface along side different reaction species to better understand the effect of coadsorption. Such studies would have to take into account diffusion of H on the surface and potential equilibrium between H on the surface and H₂ in the gas phase. Moreover, results of our work could be used to compute the reaction rates to investigate the kinetic profiles of the isomerization reaction.

Amination Part II

3.6 Introduction

Amines are important building blocks of chemical industry with applications in polymers, surfactants, dyes, pharmaceuticals and agrochemicals⁴⁵. Traditionally, most of the amines are produced industrially from petrochemical precursors. However, recently search for biobased amines have grown considerably^{5;46} and new routes for the conversion of biobased platform molecules into useful amines have been sought (Figure 3.15).

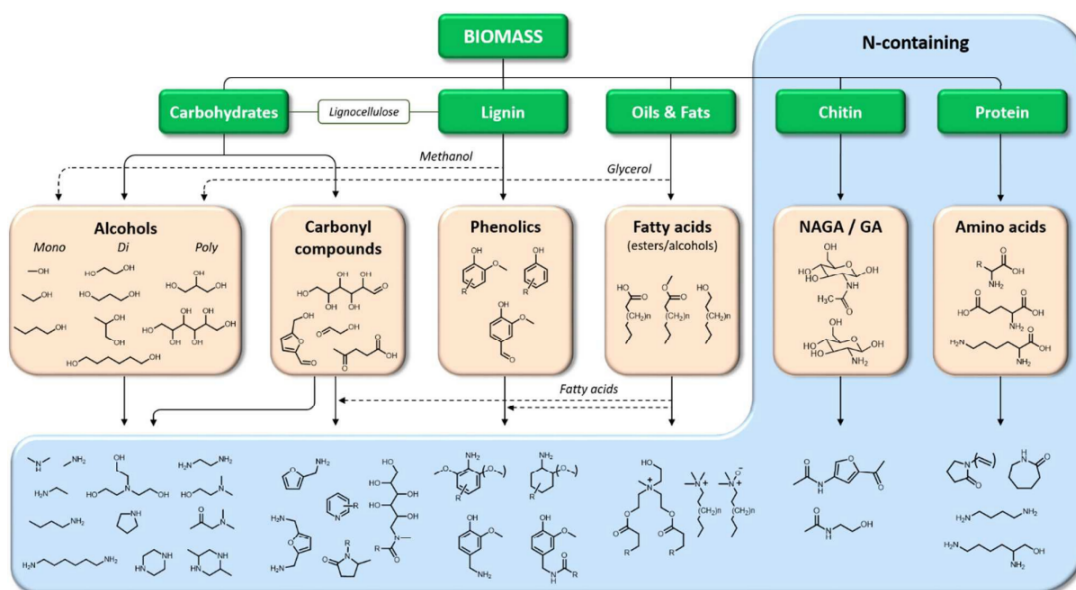
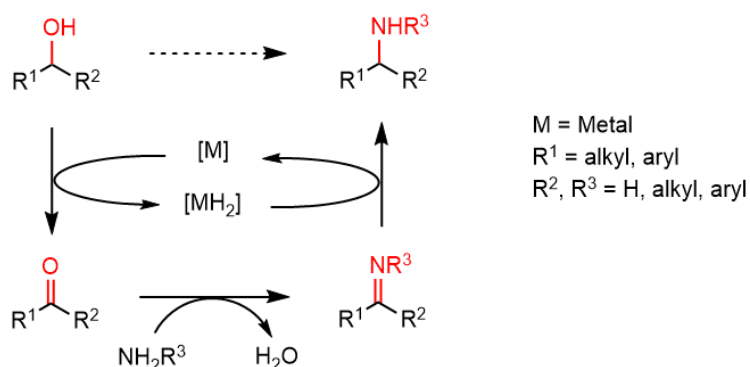


Figure 3.15: Overview of various biobased amines (blue box) that are obtained via specific (heterogeneous) catalytic transformations of the renewable platform molecules (orange boxes). These platform compounds are in turn produced through (catalytic) transformation of the different types of biomass (green boxes). Reproduced from ref⁴⁶.

Mono- and, more importantly, di-amines derived from isohexides are important biobased amines with potential applications in polymers like polyamides^{47;48} and polyimides⁴⁹. Direct catalytic amination of alcohols using gaseous or aqueous NH_3 presents itself as green method that offers the desired process economy for a potential industrial scale up⁵⁰. The direct amination is believed to proceed *via* hydrogen-borrowing mechanism (Scheme 3.3) whereby catalyst facilitates the initial extraction of H_2 from alcohol to produce ketone intermediate which undergoes condensation with NH_3 to produce imine intermediate. The subsequent hydrogenation of imine with the initially generated H_2 results in the final amine product with water as the biproduct.

Beller et al. reported the first direct amination of isosorbide with NH_3 to diamines using a homogeneous catalyst $\text{Ru}(\text{CO})\text{Cl}(\text{PPh}_3)_3$ in combination with phosphine ligand Xantphos²⁴. Starting from isosorbide, they reported 96 % diamine yield and a full conversion at 170 °C without needing any exogenous H_2 pressure indicating a hydrogen-borrowing mechanism.

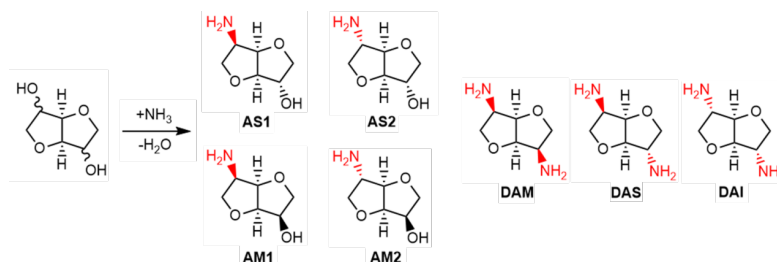


Scheme 3.3: Borrowing-hydrogen mechanism for direct amination.

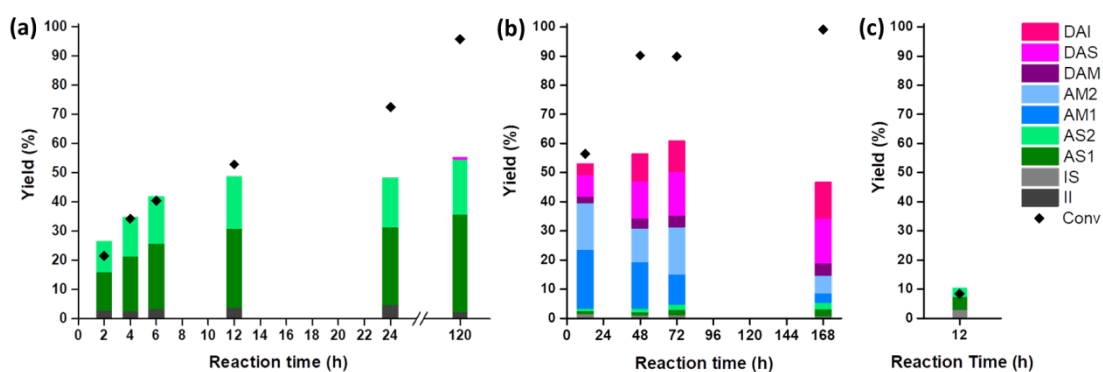
However, the stereochemistry of the final diamine products was not explicitly mentioned. Similar homogeneous catalytic combination of $\text{Ru}_3(\text{CO})_{12}$ and PNP pincer-type ligands was used by Vogt et al. for direct amination of isomannide to isohexide diamines with 96 % yield²⁵. BASF filed a patent on the catalytic amination of isohexides in organic solvents using various PNP pincer-type catalysts at 200 °C⁵¹. More recently, Jacolot et al. described the amination of isosorbide and isomannide with benzylamine in the presence of [Ir] homogeneous catalyst and diphenylphosphate, followed by the subsequent hydrogenation affording the desired isohexide diamines^{52;53}. Notwithstanding the efficiency of the homogeneous catalytic systems, they are unsuitable for industrial applications owing to the workup required to separate the products from the reaction mixtures and the use expensive ligands which are generally unstable under ambient conditions.

Solid heterogeneous catalysts present as a suitable alternative to homogeneous systems for the direct amination of isohexides. However, the efforts aimed at synthesis of isohexide diamines using solid catalysts have faced numerous challenges. Rose et al. have reported the only direct amination study of isohexides in aqueous NH_3 using a solid Ru/C catalyst²⁰. Unlike molecular catalysts, solid catalyst resulted in mostly amino-alcohols with very little diamine products. The amination of isohexides, unlike isomerization, involves a more complex chemical space and could potentially result in many different products (Scheme 3.4).

Our experimental collaborators have further explored the heterogeneously-catalyzed, direct amination of isohexides with aqueous NH_3 using Ru/C catalyst. The amination product distribution can vary depending on the starting isomer used (Figure 3.16). The amination of isosorbide only generated two amino-alcohol products with *exo*-OH (AS1 with *endo*-NH₂ and AS2 with *exo*-NH₂) and very few isoidide. Extending the reaction time to 120 h leads to full conversion and higher mass loss, but hardly any diamine is produced (0.7%), indicating low reactivity of *exo*-OH groups. Diamines products (DAM, DAS and DAI), along with amino

Scheme 3.4: Possible products from direct amination of isohexides with NH_3 .

alcohols AM1 and AM2, can be accessed from isomannide after 12 h, and the total diamine yield can be increased to 30% after 72 h, and to 32% after 168 h confirming the higher reactivity of *endo*-OH groups. Although a higher mass loss is observed at longer reaction times, the diamines to amino-alcohol ratio is improved. This indicates a slow amination of isomannide to amino alcohols, followed by amination of the former to diamines. Since the first step in amination is also deemed to be alcohol dehydrogenation to corresponding mono-ketones, this higher reactivity for *endo*-OH can be explained by the reaction profiles of isomerization (Figure 3.5) which involve lower activation barriers for dehydrogenation of *endo*-OH. Isoidide amination yields very small amount of isosorbide (3%) and amino-alcohols AS1 and AS2 (7%), pointing out a first isomerization step of isoidide to isosorbide, followed by isosorbide amination. Notably, at least dozens of hours are required to reach an equilibrium for amination reaction while isomerization equilibrium can be achieved at much shorter times.

Figure 3.16: Kinetic profiles for direct amination of: (a) isosorbide, (b) isomannide and (c) isoidide. Reaction conditions: 1 g substrate, 15 mL aq. NH_3 (25 wt.%), 0.2 g Ru/C (5 wt.%), 10 bar H_2 , 180 °C.

As the chemical space of isohexide amination is much more complex, a full reaction profile study like we have performed for isomerization is much more involved and, therefore, was not taken up in this work. Instead, we have tried to look at potential poisoning of the catalyst surface by reaction species, in particular NH_3 , which could preclude any further reaction. Since the reaction conditions in Figure 3.16 are quite similar to those of isomerization (Figure 3.6) with the exception of NH_3 , we could already see a poisoning role of NH_3 in slowing the

isomerization reaction. Furthermore, Wang et al. have studied the nitridation trends of different metallic surfaces under a pressure of NH_3 and H_2 and found that Ru is indeed quite prone to having surface nitride species when exposed to nitrogen environments⁵⁴. In this work, we have performed the *ab-initio* kinetic studies of the NH_3 splitting on Ru(0001) surface to determine the surface coverage of NH_x species which could potentially poison the catalyst. Since the amination reaction is carried out in aqueous phase, H_2O splitting was also included in the kinetic study.

3.7 Computational Details

The computational setup for the *ab-initio* part was the same as described in section 3.2. The adsorption energy of H was scaled by 0.1 eV in keeping with refs.^{55;56} to better match the experimental binding energies, however the results reported remain qualitatively same even without this scaling.

The kinetic analysis was performed for two cases: surface coverage vs. temperature and surface coverage vs. NH_3/H_2 molar ratio. For the former case, the kinetic equations were solved to find the steady state for an initial condition of 25 wt % aqueous NH_3 in 15 mL reactor and 10 bar H_2 pressure. This sets the initial molar concentrations of NH_3 , H_2O and H_2 . For the latter case, same initial condition for NH_3 was used and the concentration of H_2 was fixed by the corresponding NH_3/H_2 ratio.

The following elementary reactions were considered:

- $\text{NH}_{3(\text{g})} + * \rightleftharpoons \text{NH}_3^*$
- $\text{NH}_3^* + * \rightleftharpoons \text{NH}_2^* + \text{H}^*$
- $\text{NH}_2^* + * \rightleftharpoons \text{NH}^* + \text{H}^*$
- $\text{NH}^* + * \rightleftharpoons \text{N}^* + \text{H}^*$
- $2 \text{N}^* \rightleftharpoons \text{N}_{2(\text{g})} + 2 *$
- $\text{H}_2\text{O}_{(\text{g})} + * \rightleftharpoons \text{H}_2\text{O}^*$
- $\text{H}_2\text{O}^* + * \rightleftharpoons \text{OH}^* + \text{H}^*$
- $\text{OH}^* + * \rightleftharpoons \text{O}^* + \text{H}^*$
- $2 \text{H}^* \rightleftharpoons \text{H}_{2(\text{g})} + 2 *$

We have not considered the formation of N_2^* species on the surface but this does not alter the overall conclusion of the results reported here. The kinetic equations were solved using *Micki* program which is detailed in the previous chapter. *find_steady_state* functionality of *Micki* was used to find the steady state by solving the differential equations at the default tolerance values defined in *Micki*. The CSTR reactor with infinite flow rate was achieved by fixing the concentrations of $NH_{3(g)}$, $H_2O_{(g)}$ and $H_{2(g)}$.

3.8 Results

3.8.1 Adsorption Structures

Figure 3.17 gives the most stable geometries of the reaction intermediates and transition states involved in the elementary reactions described above. Adsorption geometry of H is the same as described in the isomerization part (Figure 3.9). All the species occupy their preferred adsorption sites as already observed in literature⁵⁷.

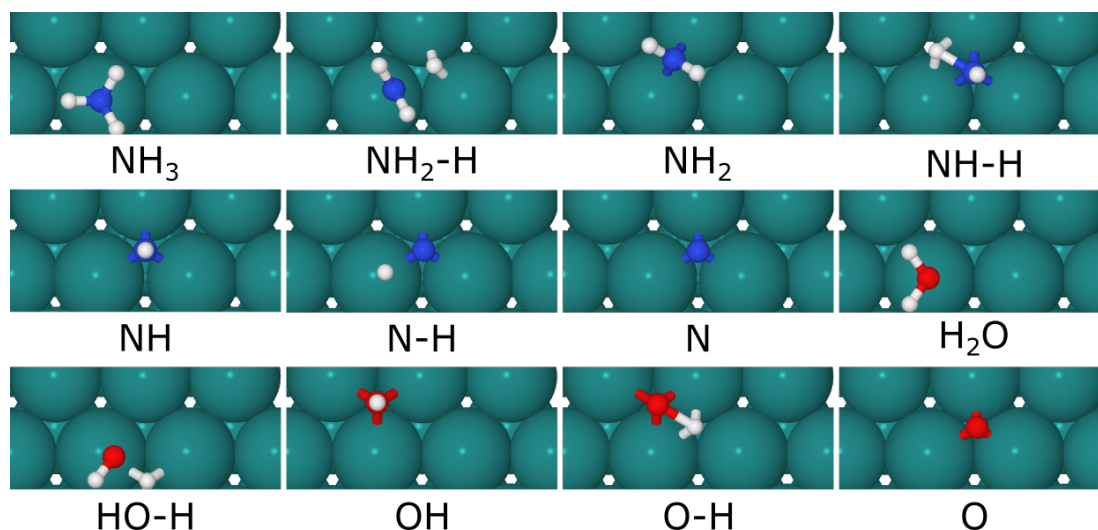


Figure 3.17: Most stable structures for the reaction intermediates and transition states considered in this study.

3.8.2 Free-energy profile

As a first step, we looked at the splitting of NH_3 and H_2O on Ru(0001) surface to produce NH_x and OH/O species. The resulting free-energy profile is given in Figure 3.18. NH_3 binds very strongly to Ru compared to H_2O and H (Figure 3.10). The first H dissociation barrier for NH_3 (104 kJ.mol^{-1}) is much higher compared to that of H_2O (66 kJ.mol^{-1}) mainly because

NH_3 adsorbs very strongly. The subsequent H dissociations for both NH_3 and H_2O have lower barriers which indicates a feasibility towards formation of OH/H and $\text{NH}_2/\text{NH}/\text{N}$ species on the surface. This is in line with the experimental observation of partially-dissociated $\text{H}_2\text{O}/\text{OH}/\text{H}$ adlayers found on Ru(0001) surface⁵⁸. Furthermore, the intermediate species resulting from successive dissociations bind stronger and stronger to the surface making the overall transformation exoenergetic, especially for NH_3 . These species could in turn render the catalyst surface inactive thereby stopping any further progress of the amination reaction.

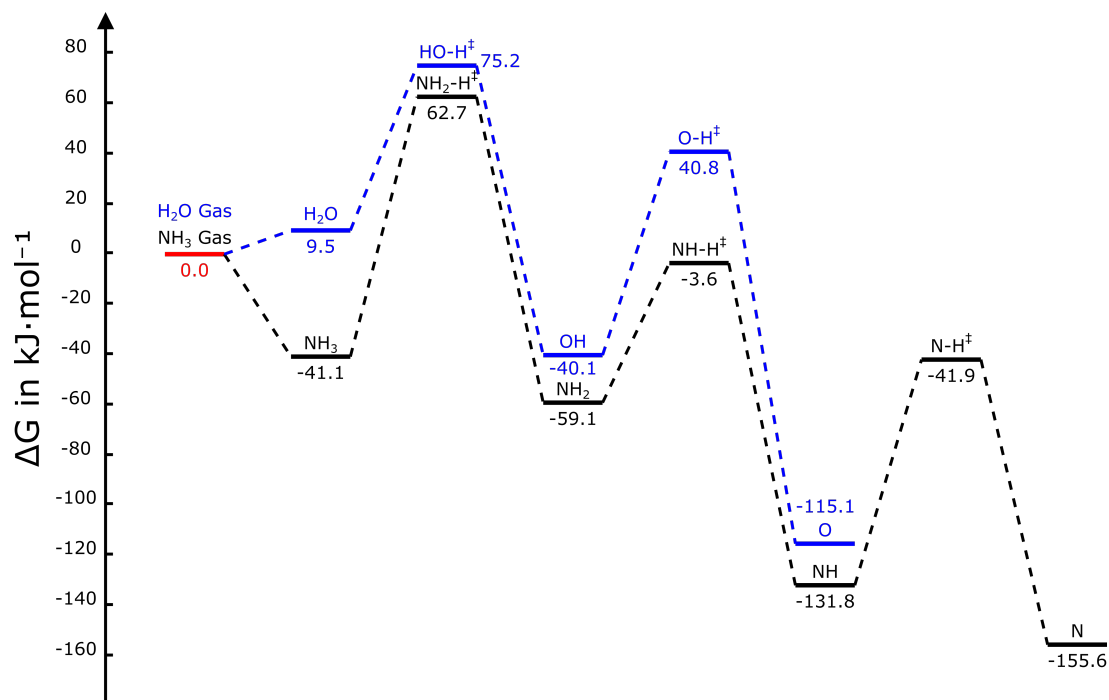


Figure 3.18: The free energy reaction profiles for NH_3 (black) and H_2O (blue) splitting on Ru(0001) surface. Frequency calculations for the adsorbate part were performed and used to calculate different contributions to enthalpy and entropy at 160 °C and 1 atm pressure under ideal-gas, harmonic approximation.

3.8.3 Kinetic Results

The free-energy profiles in Figure 3.18 clearly demonstrate thermodynamic feasibility for NH_3 and H_2O to split and produce NH_x and OH/H species on Ru surface. However, kinetic feasibility might be important and could play a major role in the final distribution of different species on the surface. Since the amination reaction of isohexides is generally carried out at 160-200 °C in the presence of a H_2 pressure, the kinetic studies were aimed at investigating the role of temperature and relative concentrations of NH_3 and H_2 .

Figure 3.19 shows the concentration of surface species in terms of temperature and NH_3/H_2

ratio at steady state. At constant NH_3/H_2 ratio, increasing the temperature results in increased NH_3 splitting to produce mostly NH and to a lesser extent N species on the surface. Third most abundant surface species is O which results from the splitting of water. The high coverage of NH species can be understood in terms of the free-energy profile which shows a very exothermic change (-73 kJ.mol^{-1}) in going from NH_2 to NH with a very small activation barrier (55 kJ.mol^{-1}). The further splitting from NH to N has a higher activation barrier (90 kJ.mol^{-1}) and is only slightly exothermic (-24 kJ.mol^{-1}) which makes it less feasible thereby resulting in the accumulation of NH species on the surface.

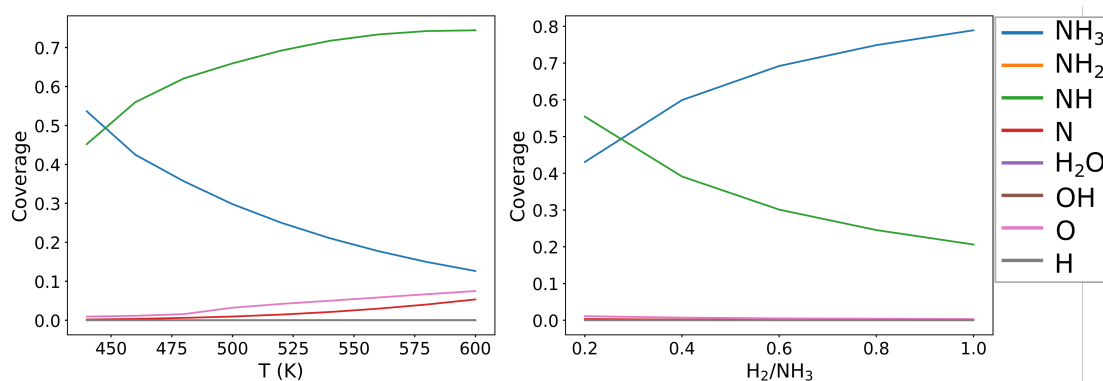


Figure 3.19: The steady-state coverage of surface species in terms of temperature and NH_3/H_2 molar ratio. For the former case, H_2 concentration was 10 bar and for the latter case the temperature was 440 K.

At constant temperature, increasing the NH_3/H_2 ratio simply reverses the surface concentrations of NH_3 and NH species and concentration of N becomes negligible. Notably, the surface coverage of H is still negligibly low and increasing H_2 pressure precludes any H_2O splitting signified by negligible concentrations of OH and O on the surface.

Overall, in both cases considered, catalyst surface seems to be covered with NH_x species even when there is very high H_2 pressure. This could be understood as a potential poisoning of the catalyst surface which is facilitated on one hand by the very strong adsorption of NH_3 and its feasibility to split on the other.

3.9 Conclusion

We have performed DFT-based kinetic study to investigate the potential poisoning of the Ru catalyst surface by NH_x species in aqueous NH_3 under a pressure of H_2 . Our results indicate that the surface is mostly covered with NH_3 and NH . A higher H_2 pressure simply reverses the surface concentrations of NH_3 and NH , NH_3 being more dominant with higher H_2 pressure, and reduces the surface concentrations of N and OH/O species resulting from

splitting of H_2O . This further serves as an example of a reaction where H_2 , although not required stoichiometrically, serves a crucial role in protecting the surface by limiting the poisoning effect of species like N, NH and O. This potential poisoning of the surface could render the catalyst inactive and stop the progress of the amination reaction. Furthermore, our preliminary results on other, more corrugated and stepped surfaces of Ru i.e. Ru(10-10) and Ru(10-11), indicate even stronger adsorption of the reaction species which signifies that the poisoning effect could be stronger on those surfaces.

Bibliography

- [1] Flèche, G.; Huchette, M. Isosorbide. Preparation, Properties and Chemistry. *Starch - Stärke* **1986**, *38*, 26–30, _eprint: <https://onlinelibrary.wiley.com/doi/pdf/10.1002/star.19860380107>.
- [2] Rose, M.; Palkovits, R. Isosorbide as a Renewable Platform chemical for Versatile Applications—Quo Vadis? *ChemSusChem* **2012**, *5*, 167–176, _eprint: <https://chemistry-europe.onlinelibrary.wiley.com/doi/pdf/10.1002/cssc.201100580>.
- [3] Delidovich, I.; Hausoul, P. J. C.; Deng, L.; Pfützenreuter, R.; Rose, M.; Palkovits, R. Alternative Monomers Based on Lignocellulose and Their Use for Polymer Production. *Chemical Reviews* **2016**, *116*, 1540–1599, Publisher: American Chemical Society.
- [4] Fenouillot, E.; Rousseau, A.; Colomines, G.; Saint-Loup, R.; Pascault, J.-P. Polymers from renewable 1,4:3,6-dianhydrohexitols (isosorbide, isomannide and isoidide): A review. *Progress in Polymer Science* **2010**, *35*, 578–622.
- [5] Froidevaux, V.; Negrell, C.; Caillol, S.; Pascault, J.-P.; Boutevin, B. Biobased Amines: From Synthesis to Polymers; Present and Future. *Chemical Reviews* **2016**, *116*, 14181–14224, Publisher: American Chemical Society.
- [6] Saxon, D. J.; Luke, A. M.; Sajjad, H.; Tolman, W. B.; Reineke, T. M. Next-generation polymers: Isosorbide as a renewable alternative. *Progress in Polymer Science* **2020**, *101*, 101196.
- [7] Wang, X.; Wang, Q.; Liu, S.; Wang, G. Synthesis and characterization of poly(isosorbide-co-butylene 2,5-furandicarboxylate) copolyesters. *European Polymer Journal* **2019**, *115*, 70–75.
- [8] Wang, X.; Wang, Q.; Liu, S.; Sun, T.; Wang, G. Synthesis and properties of poly(isosorbide 2,5-furandicarboxylate-co- ϵ -caprolactone) copolyesters. *Polymer Testing* **2020**, *81*, 106284.
- [9] Wiggins, L. F. 2. The anhydrides of polyhydric alcohols. Part I. The constitution of isomannide. *J. Chem. Soc.* **1945**, 4–7, Publisher: The Royal Society of Chemistry.
- [10] Hockett, R. C.; Fletcher, H. G.; Sheffield, E. L.; Goepp, R. M. Hexitol Anhydrides.1 The Structure of Isosorbide, a Crystalline Dianhydrosorbitol2. *Journal of the American Chemical Society* **1946**, *68*, 927–930, Publisher: American Chemical Society.
- [11] Montgomery, R.; Wiggins, L. F. 77. The anhydrides of polyhydric alcohols. Part IV. The constitution of dianhydro sorbitol. *J. Chem. Soc.* **1946**, 390–393, Publisher: The Royal Society of Chemistry.

-
- [12] Fletcher, H. G.; Goepp, R. M. Hexitol Anhydrides.1 1,4,3,6-Dianhydro-L-itol and the Structures of Isomannide and Isosorbide. *Journal of the American Chemical Society* **1946**, 68, 939–941, Publisher: American Chemical Society.
- [13] Aricò, E.; Tundo, P. Isosorbide and dimethyl carbonate: A green match. *Beilstein Journal of Organic Chemistry* **2016**, 12, 2256–2266.
- [14] Cope, A. C.; Shen, T. Y. The Stereochemistry of 1,4: 3,6-Dianhydrohexitol Derivatives1. *Journal of the American Chemical Society* **1956**, 78, 3177–3182, Publisher: American Chemical Society.
- [15] Brimacombe, J.; Foster, A.; Stacey, M.; Whiffen, D. Aspects of stereochemistry—I: Properties and reactions of some diols. *Tetrahedron* **1958**, 4, 351–360.
- [16] Wright, L. W.; Brandner, J. D. Catalytic Isomerization of Polyhydric Alcohols.1 II. The Isomerization of Isosorbide to Isomannide and Isoidide. *The Journal of Organic Chemistry* **1964**, 29, 2979–2982, Publisher: American Chemical Society.
- [17] Lemieux, R. U.; McInnes, A. G. THE PREFERENTIAL TOSYLATION OF THE ENDO-5-HYDROXYL GROUP OF 1,4;3,6-DIANHYDRO-D-GLUCITOL. *Canadian Journal of Chemistry* **1960**, 38, 136–140, Publisher: NRC Research Press.
- [18] Tundo, P.; Aricò, E.; Gauthier, G.; Rossi, L.; Rosamilia, A.; Bevinakatti, H.; Sievert, R.; Newman, C. Green Synthesis of Dimethyl Isosorbide. *ChemSusChem* **2010**, 3, 566–570, Publisher: John Wiley & Sons, Ltd.
- [19] Pruvost, R.; Boulanger, J.; Léger, B.; Ponchel, A.; Monflier, E.; Ibert, M.; Mortreux, A.; Chenal, T.; Sauthier, M. Synthesis of 1,4:3,6-Dianhydrohexitols Diesters from the Palladium-Catalyzed Hydroesterification Reaction. *ChemSusChem* **2014**, 7, 3157–3163, Publisher: John Wiley & Sons, Ltd.
- [20] Pfützenreuter, R.; Rose, M. Aqueous-Phase Amination of Biogenic Isohexides by using Ru/C as a Solid Catalyst. *ChemCatChem* **2016**, 8, 251–255, Publisher: John Wiley & Sons, Ltd.
- [21] Le Nôtre, J.; van Haveren, J.; van Es, D. S. Synthesis of Isoidide through Epimerization of Isosorbide using Ruthenium on Carbon. *ChemSusChem* **2013**, 6, 693–700, Publisher: John Wiley & Sons, Ltd.
- [22] Engel, R. V.; Niemeier, J.; Fink, A.; Rose, M. Unravelling the Mechanism of the Ru/C-Catalysed Isohexide and Ether Isomerization by Hydrogen Isotope Exchange. *Advanced Synthesis & Catalysis* **2018**, 360, 2358–2363, Publisher: John Wiley & Sons, Ltd.

- [23] WRIGHT, L.; HARTMANN, L. Catalytic Isomerization of the Hexitols; D-Glucitol, D-Mannitol, L-Iditol, and Galactitol. *The Journal of Organic Chemistry* **1961**, 26, 1588–1596, Publisher: American Chemical Society.
- [24] Imm, S.; Bähn, S.; Zhang, M.; Neubert, L.; Neumann, H.; Klasovsky, F.; Pfeffer, J.; Haas, T.; Beller, M. Improved Ruthenium-Catalyzed Amination of Alcohols with Ammonia: Synthesis of Diamines and Amino Esters. *Angewandte Chemie International Edition* **2011**, 50, 7599–7603, Publisher: John Wiley & Sons, Ltd.
- [25] Pinggen, D.; Diebolt, O.; Vogt, D. Direct Amination of Bio-Alcohols Using Ammonia. *ChemCatChem* **2013**, 5, 2905–2912, Publisher: John Wiley & Sons, Ltd.
- [26] Vanbésien, T.; Delaunay, T.; Wiatz, V.; Bigot, S.; Bricout, H.; Tilloy, S.; Monflier, E. Epimerization of isosorbide catalyzed by homogeneous ruthenium-phosphine complexes: A new step towards an industrial process. *Inorganica Chimica Acta* **2021**, 515, 120094.
- [27] Hu, H.; Ramzan, A.; Wischert, R.; Jérôme, F.; Michel, C.; de Olivera Vigier, K.; Pera-Titus, M. Pivotal role of H₂ in the isomerisation of isosorbide over a Ru/C catalyst. *Catal. Sci. Technol.* **2021**, 7973–7981, Publisher: The Royal Society of Chemistry.
- [28] Kresse, G.; Furthmüller, J. Efficient iterative schemes for ab initio total-energy calculations using a plane-wave basis set. *Phys. Rev. B* **1996**, 54, 11169–11186, Publisher: American Physical Society.
- [29] Perdew, J. P.; Burke, K.; Ernzerhof, M. Generalized Gradient Approximation Made Simple. *Phys. Rev. Lett.* **1996**, 77, 3865–3868, Publisher: American Physical Society.
- [30] Steinmann, S. N.; Corminboeuf, C. A generalized-gradient approximation exchange hole model for dispersion coefficients. *The Journal of Chemical Physics* **2011**, 134, 044117, Publisher: American Institute of Physics.
- [31] Blöchl, P. E. Projector augmented-wave method. *Phys. Rev. B* **1994**, 50, 17953–17979, Publisher: American Physical Society.
- [32] Kresse, G.; Joubert, D. From ultrasoft pseudopotentials to the projector augmented-wave method. *Phys. Rev. B* **1999**, 59, 1758–1775, Publisher: American Physical Society.
- [33] Arblaster, J. W. Crystallographic Properties of Ruthenium. *Platinum Metals Review* **2013**, 57, 127–136.
- [34] Michel, C.; Zaffran, J.; Ruppert, A. M.; Matras-Michalska, J.; Jędrzejczyk, M.; Grams, J.; Sautet, P. Role of water in metal catalyst performance for ketone hydrogenation: a joint experimental and theoretical study on levulinic acid conversion into gamma-valerolactone. *Chem. Commun.* **2014**, 50, 12450–12453, Publisher: The Royal Society of Chemistry.

-
- [35] Zaffran, J.; Michel, C.; Delbecq, E.; Sautet, P. Trade-Off between Accuracy and Universality in Linear Energy Relations for Alcohol Dehydrogenation on Transition Metals. *The Journal of Physical Chemistry C* **2015**, *119*, 12988–12998, Publisher: American Chemical Society.
- [36] Brookhart, M.; Green, M. L. H.; Parkin, G. Agostic interactions in transition metal compounds. *Proceedings of the National Academy of Sciences* **2007**, *104*, 6908–6914, Publisher: National Academy of Sciences _eprint: <https://www.pnas.org/content/104/17/6908.full.pdf>.
- [37] Michel, C.; Göltl, F.; Sautet, P. Early stages of water/hydroxyl phase generation at transition metal surfaces – synergetic adsorption and O–H bond dissociation assistance. *Phys. Chem. Chem. Phys.* **2012**, *14*, 15286–15290, Publisher: The Royal Society of Chemistry.
- [38] Lejaeghere, K.; Van Speybroeck, V.; Van Oost, G.; Cottenier, S. Error Estimates for Solid-State Density-Functional Theory Predictions: An Overview by Means of the Ground-State Elemental Crystals. *Critical Reviews in Solid State and Materials Sciences* **2014**, *39*, 1–24, Publisher: Taylor & Francis.
- [39] Delbecq, E.; Sautet, P. Adsorption of aldehydes and ketones on platinum and palladium: influence of steps, open faces and metal nature: A theoretical study. *Surface Science* **1993**, *295*, 353–373.
- [40] Kozuch, S.; Shaik, S. How to Conceptualize Catalytic Cycles? The Energetic Span Model. *Accounts of Chemical Research* **2011**, *44*, 101–110, Publisher: American Chemical Society.
- [41] Kaźmierczak, K.; Ramamoorthy, R. K.; Moisset, A.; Viau, G.; Viola, A.; Giraud, M.; Peron, J.; Sicard, L.; Piquemal, J.-Y.; Besson, M.; Perret, N.; Michel, C. Importance of the decoration in shaped cobalt nanoparticles in the acceptor-less secondary alcohol dehydrogenation. *Catal. Sci. Technol.* **2020**, *10*, 4923–4937, Publisher: The Royal Society of Chemistry.
- [42] Walsh, A.; Catlow, C. R. A. Structure, stability and work functions of the low index surfaces of pure indium oxide and Sn-doped indium oxide (ITO) from density functional theory. *J. Mater. Chem.* **2010**, *20*, 10438–10444, Publisher: The Royal Society of Chemistry.
- [43] Andersen, M.; Panosetti, C.; Reuter, K. A Practical Guide to Surface Kinetic Monte Carlo Simulations. *Frontiers in Chemistry* **2019**, *7*, 202.
- [44] Yun, J.-H.; He, Y.; Otero, M.; Düren, T.; Seaton, N. In *Studies in Surface Science and Catalysis*; Rodriguez-Reinoso, F., McEnaney, B., Rouquerol, J., Unger, K., Eds.; Elsevier, 2002; Vol. 144; pp 685–692.
- [45] Lawrence, S. A. *Amines: Synthesis, Properties and Applications*; Cambridge University Press, 2004.

- [46] Pelckmans, M.; Renders, T.; Van de Vyver, S.; Sels, B. F. Bio-based amines through sustainable heterogeneous catalysis. *Green Chem.* **2017**, *19*, 5303–5331, Publisher: The Royal Society of Chemistry.
- [47] Jasinska, L.; Dudenko, D.; Rozanski, A. J.; Thiyagarajan, S.; Sowinski, P.; Es, D., van; Shu, J.; Hansen, M. R.; Koning, C. E. Structure and molecular dynamics in renewable polyamides from dideoxy-diamino isohexide. *Macromolecules* **2012**, *45*, 5653–5666, Publisher: American Chemical Society.
- [48] Wu, J.; Jasinska-Walc, L.; Dudenko, D.; Rozanski, A.; Hansen, M. R.; van Es, D.; Koning, C. E. An Investigation of Polyamides Based on Isoidide-2,5-dimethyleneamine as a Green Rigid Building Block with Enhanced Reactivity. *Macromolecules* **2012**, *45*, 9333–9346, Publisher: American Chemical Society.
- [49] Ji, X.; Wang, Z.; Yan, J.; Wang, Z. Partially bio-based polyimides from isohexide-derived diamines. *Polymer* **2015**, *74*, 38–45.
- [50] Pera-Titus, M.; Shi, F. Catalytic Amination of Biomass-Based Alcohols. *ChemSusChem* **2014**, *7*, 720–722, Publisher: John Wiley & Sons, Ltd.
- [51] SCHELWIES, M.; Brinks, M.; Schaub, T.; Melder, J.-P.; Paciello, R.; Merger, M. PROCESS FOR THE HOMOGENEOUSLY CATALYZED AMINATION OF ALCOHOLS WITH AMMONIA IN THE PRESENCE OF A COMPLEX CATALYST WHICH COMPRISES NOANONIC LIGANDS. 2014.
- [52] Jacolot, M.; Moebis-Sanchez, S.; Popowycz, F. Diastereoselective Iridium-Catalyzed Amination of Biosourced Isohexides Through Borrowing Hydrogen Methodology. *The Journal of Organic Chemistry* **2018**, *83*, 9456–9463, Publisher: American Chemical Society.
- [53] Bahé, F.; Grand, L.; Cartier, E.; Jacolot, M.; Moebis-Sanchez, S.; Portinha, D.; Fleury, E.; Popowycz, F. Direct Amination of Isohexides via Borrowing Hydrogen Methodology: Regio- and Stereoselective Issues. *European Journal of Organic Chemistry* **2020**, *2020*, 599–608, Publisher: John Wiley & Sons, Ltd.
- [54] Wang, T.; Yan, Z.; Michel, C.; Pera-Titus, M.; Sautet, P. Trends and Control in the Nitridation of Transition-Metal Surfaces. *ACS Catalysis* **2018**, *8*, 63–68, Publisher: American Chemical Society.
- [55] Hermes, E. D.; Janes, A. N.; Schmidt, J. R. Micki: A python-based object-oriented microkinetic modeling code. *The Journal of Chemical Physics* **2019**, *151*, 014112.
- [56] Hermes, E. D.; Janes, A. N.; Schmidt, J. R. Mechanistic Insights into Solution-Phase Oxidative Esterification of Primary Alcohols on Pd(111) from First-Principles Microkinetic Modeling. *ACS Catalysis* **2018**, *8*, 272–282.

-
- [57] Herron, J. A.; Tonelli, S.; Mavrikakis, M. Atomic and molecular adsorption on Ru(0001). *Surface Science* **2013**, *614*, 64–74.
- [58] Feibelman, P. J. Partial dissociation of water on Ru(0001). *Science (New York, N.Y.)* **2002**, *295*, 99–102, Place: United States.



4 Surface State of Ru catalysts

4.1 Introduction

As established in our work on isosorbide, supported-Ru catalysts are quite ubiquitous in biomass valorization and subsequent transformations of biomass-derived *platform molecules* into value added products¹⁻⁵. Ruthenium, therefore, holds a special promise in the attempt to devise routes for the conversion of biomass into useful chemicals that not only could potentially replace the fossil-derived products but also give rise to novel biobased-products with new and improved properties⁶.

Although supported-Ru catalysts have been found extremely useful in the biomass-related transformations, there are still some puzzling aspects about the reactivity of these catalysts. In particular, supported-Ru catalysts have been found to show increased reactivity in liquid water compared to other non-aqueous solvents. For conversion of 2-butanone into 2-butanol, a Ru/SiO₂ catalyst showed 33 times higher reactivity in water than in methanol (Table 4.1)⁷. Using a combination of DFT calculations, spectroscopy and reaction kinetics data, the authors rationalized this enhanced activity of water in terms of its ability to lower the activation barriers, by making hydrogen-bonds with the reaction intermediates and transition states, and to facilitate the proton diffusion.

Table 4.1: Comparison of initial reaction rate at 303.15 K, 3 bar H₂ and 1400 rpm using 5 wt% Ru/SiO₂ (measured at 298.15 K) for conversion of 2-butanone into 2-butanol. Adapted from ref. ⁷.

Solvent	Rate(mol min ⁻¹ g ⁻¹ × 10 ⁴)
Water	31.90
IPA	4.55
Methanol	0.95
Heptane	1.25

Similar water-induced enhanced activity for Ru was observed in the conversion of levulinic acid (LA), another important *platform molecule* derived from cellulose, into γ -valerolactone (GVL) on Ru/TiO₂ catalysts⁸. A DFT-based study of the full reaction coordinate using acetone as a model ketone with and without a co-adsorbed water molecule demonstrated a 35 % decrease in effective activation barrier in the former case. Furthermore, this behavior was in contrast with other hydrogenation catalysts like Pd and Pt which were found to be insensitive to the solvent.

Both of the studies reported above relied upon the intuitive idea to include one or few water molecules in a so-called *microsolvation* approach to extract the major effects of water on the reaction species. However, it still remains to be seen if these water moieties assumed *a priori* to exist on the surface are thermodynamically viable. In other words, a full characterization of the surface species under complicated experimental conditions involving liquid water, high

temperature and high pressure of H_2 is required.

Adlayers of water on Ru(0001) surface have been well studied using both theoretical and surface science techniques. Feibelman, and more recently Messaoudi et. al., have shown that partially-dissociated monolayer of water on Ru(0001) comprising of H_2O/OH hexagonal patterns with H occupying the empty top sites is more stable than an intact water layer⁹. This was further supported by TPD experiments which demonstrated the presence of H species on the surface after desorption of H_2O ; the remaining H was subsequently desorbed at higher temperature (Figure 4.1)¹⁰. Recently, STM experiments were performed to observe thermally-induced dissociation structures of water on Ru(0001) at temperatures as low as 120 K; and a passivation effect was observed for further adsorption of H_2O or CO which was attributed to presence of dilute H adlayers formed by dissociation of water molecules¹¹. In addition, formation of $Ru(OH)_x$ species on Ru/SiO₂ catalyst was hypothesized to account for the observed deactivation in the initial activity of the catalyst for hydrogenation of 2-butanol in water¹².

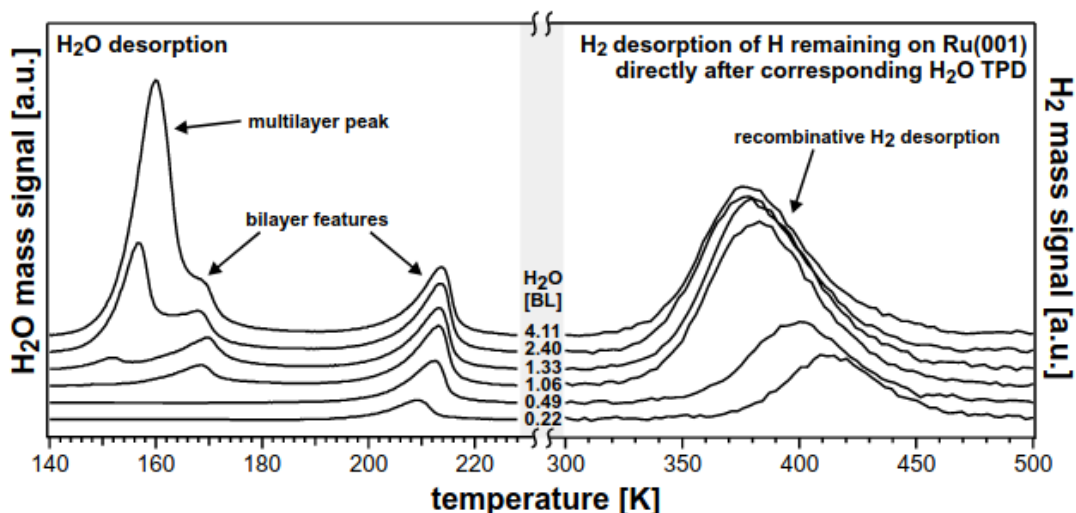


Figure 4.1: Coverage dependent TPD spectra of H_2O (left; heating rate 0.5 K/s) together with the corresponding H_2 TPD recorded directly afterwards (right; 2 K/s). The initial H_2O coverage is given in the middle normalized to one bilayer (BL). Data are offset for clarity. Taken from ref¹⁰.

These theoretical and experimental observations serve as a good starting point in an attempt to characterizing the surface state of supported-Ru catalysts at a more atomistic level. In particular, the surface science studies are performed in ultra-vacuum conditions at low temperatures and a more sophisticated approach is required to bridge the gap to more realistic reaction conditions of temperature and pressure. DFT-based *ab-initio* atomistic thermodynamics is a well-established technique to study the relative stability of a different solid phase in contact with a gas phase environment at specified temperature and pressure and was, therefore, adopted in our current study.

4.2 Methodology - Ab-initio Thermodynamics

In this section we extend the thermodynamic formalism presented in Chapter 2 to a more general case of a catalyst (solid) surface in contact with a gas phase environment potentially comprising of *one or more* species at specified temperature and pressure (partial pressure in case of more than one gas phase species). Figure 4.2 shows such a system where a Ru catalyst is in contact with a gaseous environment of H_2 and water vapor. Following the reasoning

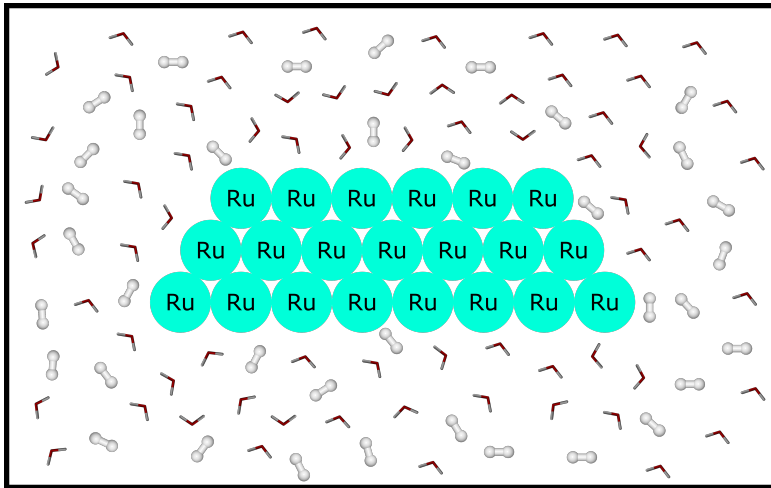


Figure 4.2: Pictorial representation of a solid catalyst surface in contact with a gas phase environment, in this example comprising of H_2 and water vapor.

presented in ref.¹³, one could focus on the interface of the system, energetics of the bulk phases (solid bulk or homogeneous gas) are unaffected by the adsorption, and define a so called surface energy γ of the system,

$$\gamma = \frac{1}{2A} (G - G_{solid} - G_{gas}) \quad (4.1)$$

where G is the Gibbs free energy of the total system; G_{solid} and G_{gas} are the corresponding Gibbs free energies of the solid and gaseous phases, respectively. The factor of two is required to account for the symmetry of the interface resulting from solid-gas interactions when using a periodic slab model and A is the surface area of the solid phase in contact with the gaseous environment.

One could define the above quantity by a finite part of the total system as moving away from the interface results in unaffected solid bulk and homogeneous gas phase contributions of which are cancelled out in Eq. 4.1. For our case of interest, if one considers that this (finite) interfacial part of the total system is comprised of N_{Ru} atoms of Ru; N_O atoms of O and N_H

atoms of H, then we can rewrite γ as,

$$\gamma(T, p) = \frac{1}{2A} \left(G(T, p, N_{Ru}, N_H, N_O) - N_{Ru} g_{Ru}(T, p) - N_H \mu_H(T, p) - N_O \mu_O(T, p) \right) \quad (4.2)$$

where we have used the Gibbs free energy per atom of bulk Ru, g_{Ru} , and the chemical potentials of H, $\mu_H(T, p)$ and O, $\mu_O(T, p)$, as defined by the gaseous reservoir. Under this definition, $\gamma > 0$ represents the cost of creating the interface between bulk solid and gas phase reservoir.

In the present work, we are interested in the most stable phases that result from the adsorption of gas phase species on the solid surface at the given conditions of temperature and pressure. For such case, one could define surface free energy, γ_{ref} , of a reference phase which, say, is comprised of N_{Ru}^{ref} atoms of Ru; N_O^{ref} atoms of O and N_H^{ref} atoms of H,

$$\gamma_{ref}(T, p) = \frac{1}{2A_{ref}} \left(G(T, p, N_{Ru}^{ref}, N_H^{ref}, N_O^{ref}) - N_{Ru}^{ref} g_{Ru}(T, p) - N_H^{ref} \mu_H(T, p) - N_O^{ref} \mu_O(T, p) \right)$$

and then calculate the Gibbs free energy of adsorption as the difference,

$$\begin{aligned} \Delta G_{ads}^{gas}(T, p) &\equiv \gamma(T, p) - \gamma_{ref}(T, p) \\ &= \frac{1}{2A} \left(G(T, p, N_{Ru}, N_H, N_O) - G(T, p, N_{Ru}, N_H^{ref}, N_O^{ref}) \right. \\ &\quad \left. - (N_H - N_H^{ref}) \mu_H(T, p) - (N_O - N_O^{ref}) \mu_O(T, p) \right) \end{aligned} \quad (4.3)$$

where we have assumed that the reference phase and the given phase have the same number of Ru atoms, N_{Ru} and surface area, A . The superscript *gas* signifies that all the species are in gas or vapor phase defined by the temperature and their partial pressure. With the above definition, $\Delta G_{ads} < 0$ indicates a phase more stable than the reference phase.

In addition to the gas phase reservoir interacting with the solid catalyst surface, we are interested in the case where a solvent is present in the system. In particular, we want to understand the effect of solvent in liquid phase on the adsorption of different species (Figure 4.3). This requires an explicit treatment of the solvent for which we have used the MMSol scheme described in chapter 2, Figure 2.5. The reference phase described above could be chosen to perform the MMSol calculation to obtain the ΔG_{solv} using Eq. 2.36. Once ΔG_{solv} is known, Eq.

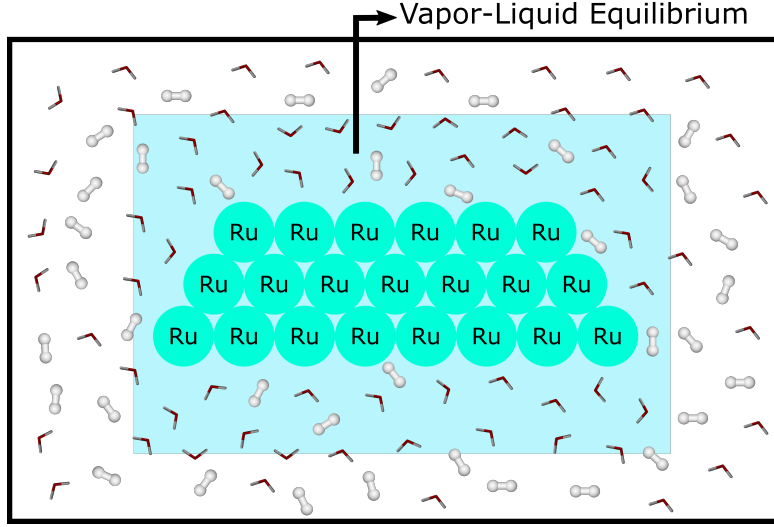


Figure 4.3: Pictorial representation of a solid catalyst surface immersed in liquid water (blue box) under a gas phase pressure of H_2 . The liquid water is in equilibrium with the vapor phase above the liquid.

4.3 can be updated as,

$$\begin{aligned} \Delta G_{ads}^{solv}(T, p) = & \frac{1}{2A} \left(G(T, p, N_{Ru}, N_H, N_O) + G_{solv} \right. \\ & - G(T, p, N_{Ru}, N_H^{ref}, N_O^{ref}) \\ & \left. - (N_H - N_H^{ref})\mu_H(T, p) - (N_O - N_O^{ref})\mu_O(T, p) \right) \equiv \gamma_{solv} - \gamma_{ref} \end{aligned} \quad (4.4)$$

where γ_{solv} is the surface free energy of the given phase taking into account ΔG_{solv} . In the following we briefly describe how different terms in Eq. 4.3 and 4.4 are calculated.

4.2.1 Solid Phase

Eq. 4.3, and in turn, Eq. 4.4, require calculating terms of the form $G(T, p, N_{Ru}, N_H, N_O)$, which is the Gibbs free energy of a given solid phase. First, one could notice that a difference of such terms enters the equations which allows for a considerable degree of error cancellation in the underlying electronic energy calculations. In our work, these solid phases are comprised of a given surface termination of Ru with or without adsorbed H/O/OH/ H_2O species. Periodic DFT is well suited to calculate the energy of such phases as shown in chapter 3. The $G(T, p, N_{Ru}, N_H, N_O)$ term can further be broken down into various contributions,

$$\begin{aligned} G(T, p, N_{Ru}, N_H, N_O) = & E_{elec}(T, p, N_{Ru}, N_H, N_O) \\ & + F_{vib}(T, p, N_{Ru}, N_H, N_O) + F_{con}(T, p, N_{Ru}, N_H, N_O) + pV \end{aligned} \quad (4.5)$$

4.2. Methodology - Ab-initio Thermodynamics

where E_{elec} is the total electronic energy easily accessible from a periodic DFT calculation and accounts for the *ab initio* part of the corresponding ab-initio atomistic thermodynamics methodology; F_{vib} and F_{conf} are the vibrational and configurational Helmholtz free energies, respectively. It should be noted that the formalism of ab-initio atomistic thermodynamics is general and the E_{elec} term can in principle be obtained from any electronic structure method (i.e. parameterized force fields) subject to arbitrary level of approximation, however, the accuracy of the resulting thermodynamic picture is only valid to that level of theory and the predictive power of such low level electronic-energy calculation schemes can be limited. The last term pV has a contribution of the order of tenth of meV¹⁴ and thus can be neglected. The vibrational term can further be decomposed into energetic and entropic terms,

$$F_{vib}(T, p, N_{Ru}, N_H, N_O) = E_{vib}(T, p, N_{Ru}, N_H, N_O) - TS_{vib}(T, p, N_{Ru}, N_H, N_O) \quad (4.6)$$

where $E_{vib}(T, p, N_{Ru}, N_H, N_O)$ is now the total vibrational energy including the zero-point energy and $S_{vib}(T, p, N_{Ru}, N_H, N_O)$ is the corresponding vibrational entropy. As demonstrated in chapter 3, the vibrational contribution can be included by calculating the vibrational modes of, at least, the adsorbate species at DFT level under the harmonic approximation; and in general this contribution is not negligible and can alter the overall thermodynamic picture of stability of different phases¹⁵ especially for systems comprised of H containing species i.e. OH and H₂O¹⁶. A simple recipe to include the vibrational contribution is also given in ref.¹⁶, however, it is not implemented in the preparation of the results reported. We did, however, performed DFT-level frequency calculations for phases containing only atomic H and O species and the effect of the vibrational contribution on the thermodynamic stability of these phases is discussed.

The final term in Eq. 4.5 is the configurational free energy which is computationally more involved and time consuming since it requires sampling a large phase space of all possible surface adsorption configurations under given thermodynamic conditions. This problem can in principle be addressed by advanced computational techniques like Monte Carlo^{17;18} but they require prohibitively large number of free energy calculation steps each performed at a reasonably accurate level of electronic structure description¹⁹. This problem is often circumvented by model Hamiltonians which are fast to evaluate and whose parameters can be derived from a few first principles calculations^{19;20}. A simpler alternative, which is also employed in our current work reported in this chapter, is to scan a few relevant, ordered structures and then see which one of them is most stable under given thermodynamic conditions (which one minimizes the surface free energy or Gibbs free energy of adsorption as defined above). This approach leads to an additional configurational entropy term arising from the potential defects in the ordered structures considered. This additional contribution is of the order of 3 meV/Å² for temperatures below 1000 K and thus can be ignored¹³.

Chapter 4. Surface State of Ru catalysts

This approach, however, puts an obvious limitation on the predictive power of the ab-initio atomistic thermodynamics technique: only the stability of those configurations can be discussed which have been plugged into the thermodynamic model and it gives no information as to the stability of the configurations not considered in the treatment. Still, the method gives an important tool to compare different structures and also gives one an idea of which configurations should be considered in future. Generating a large collection of potentially random configurations might be a good way to sample enough structures to make the underlying thermodynamic picture reliable and of predictive quality. Same was done in our work and is described in detail in the next section. It is worth mentioning that this approach does not include the problem of kinetics whereby certain structures which are thermodynamically stable might be inaccessible kinetically.

4.2.2 Challenge of Phase Space

In this work we are interested in the surface state of the supported Ru catalysts in water (either liquid or vapor phase) under a pressure of H_2 . As shown in Figure 2.1, a Ru nanoparticle in equilibrium with a gas phase environment can expose various facets with different surface morphologies. Under isolated, equilibrium conditions, the shape of the nanoparticle and the fraction of each exposed facet can be determined by Wulff construction²¹ based on the surface free energy of each facet. Table 4.2 gives the surface free energy of five most exposed facets of Ru and the corresponding area fractions determined from the Wulff construction shown in Figure 4.4. As can be seen, Ru(0001) is the most stable surface termination, however, it is not the most exposed one. Any reasonably detailed sampling of the surface morphology phase space must, therefore, include other exposed facets and potential adsorption of various gas phase species on their surface. We have chosen to include the 3 most exposed facets, namely Ru(0001), Ru(10-10) and Ru(10-11).

Table 4.2: Surface free energy and the area fraction of the five most exposed facets on the surface of an isolated Ru nanoparticle under equilibrium. The values taken from ref²².

Miller Indices	γ (J.m ⁻²)	Area Fraction
(0001)	2.6	16
(10-11)	2.88	43
(10-10)	2.91	21
(10-12)	3.05	10
(2-1-12)	3.11	6

Once the facets have been chosen, next step is to study the adsorption of different species on their surface. This further requires identifying the potential, distinct adsorption sites on the surface of these facets. Figure 4.5 shows the top and side view of the selected Ru terminations

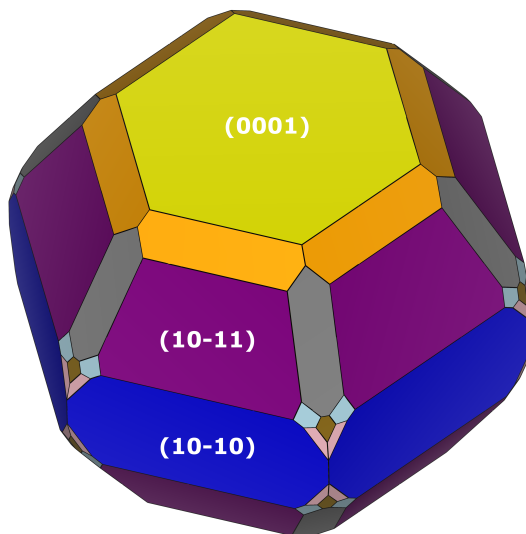


Figure 4.4: The Wulff construction of an isolated Ru nanoparticle in equilibrium using the surface free energy values given in Table 4.2. The 3 most exposed facets have been marked. Made with VESTA²³.

and also highlights the distinct adsorption sites. Ru(0001) is a close-packed planar surface with well-known *fcc*, *hcp*, *top* and *bridge* adsorption sites; Ru(10-10) and Ru(10-11), on the other hand, are more corrugated and offer a wider range of adsorption sites for the potential adsorbates.

Random Generator

A random generator based on the adsorption behavior of different gas phase species was developed to randomly generate a database of the surface configurations for the three facets considered. For this purpose, the adsorption free energy (Eq. 2.26) of different atomic and molecular species was computed for all possible adsorption sites on a given facet. A Python program was developed to build random adsorption geometries based on this site-preference of different species which consists of the following steps.

- Pre-build a collection of all sites on a given facet and the potential species that might bind to that site i.e for Ru(0001) *fcc* site can accommodate OH or H but not O whereas potentially all three species can bind to *hcp* site.
- Pre-build a collection of the coordinates of all sites and group them into unique categories shown in Figure 4.5.
- Pre-build a collection of adsorption distances for each species; OH was allowed two different distances based on whether adsorption is vertical or horizontal.

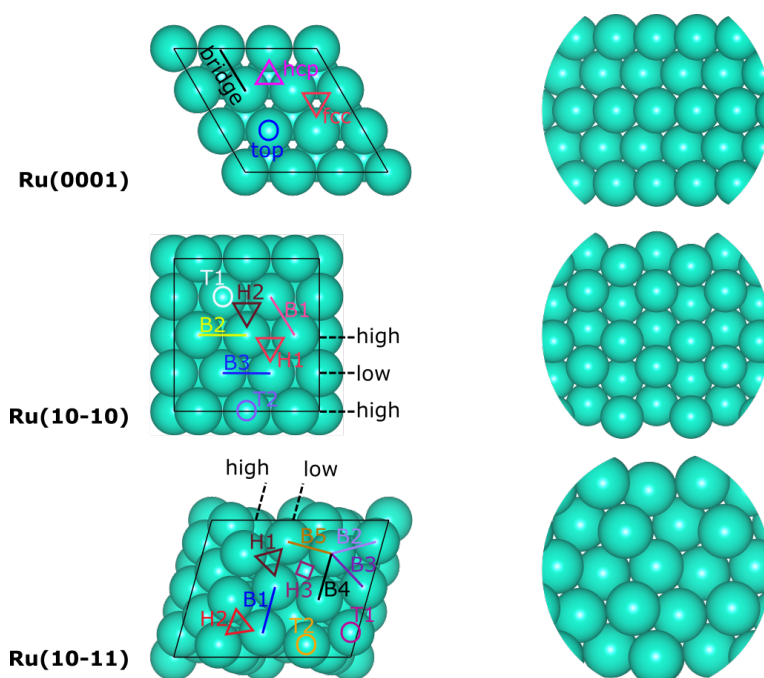


Figure 4.5: Top (left) and side (right) view of the three Ru facets considered in this work. The unique adsorption sites have been indicated.

- Choose a random site type (fcc, hcp, H1, B1, etc.)
- Choose a random site available for the chosen type
- Choose a random specie that potentially goes to that site
- Adsorb the specie on that site with specified distance
- Check for «clashes»: if Clashes, stick to the old adsorption structure otherwise update the adsorption geometry and delete the chosen site from the pre-built collection (step 2).
- Repeat the previous steps for a given number of iterations to achieve reasonably large coverage.

In addition to the steps described, if H₂O or OH were selected for adsorption on the corresponding top sites, the H atom(s) were randomly rotated by $\pm 30^\circ$. The «clashes» criterion was chosen such as to achieve the reasonable starting adsorption geometries without atoms being too close. This allowed for a considerable speedup in the subsequent optimization at the DFT level.

Furthermore, in addition to the random configurations, the adsorption of O and H atoms was systematically studied at each level of coverage (Figure 3.9) for all three facets. The well-known intact and partially dissociated water layers on Ru(0001)⁹ were also included in the data set.

4.2.3 Gas Phase Reservoir

Eq. 4.3 and 4.4 require calculating the chemical potential of the species in the gas phase environment surrounding the solid surface. We employ the ideal gas approximation for the gas phase species and chemical potential under this approximation is simply the Gibbs free energy per particle¹⁴,

$$\mu_i = \left(\frac{\partial G}{\partial N_i} \right)_{T,p,N_{j \neq i}} = \frac{G}{N_i}. \quad (4.7)$$

Since Gibbs free energy is a potential functions of temperature and pressure, one can start with the following Maxwell relation which relates the partial derivative of Gibbs free energy w.r.t. pressure with volume,

$$\left(\frac{\partial G}{\partial p} \right)_T = V \quad (4.8)$$

and then use the ideal-gas law $pV = NkT$ to substitute the volume,

$$\left(\frac{\partial G}{\partial p} \right)_T = \frac{NkT}{p} \quad (4.9)$$

to get an expression in terms of only temperature and pressure, where k is the Boltzmann constant. Integrating the above equation from a reference pressure p° to p , gives,

$$\int_{p^\circ}^p \left(\frac{\partial G}{\partial p} \right)_T dp = G(T, p) - G(T, p^\circ) = NkT \ln \left(\frac{p}{p^\circ} \right) \quad (4.10)$$

and using Eq. 4.7, and after some rearrangement, one could get

$$\mu_i(T, p) = \mu_i(T, p^\circ) + NkT \ln \left(\frac{p_i}{p^\circ} \right), \quad (4.11)$$

which gives the desired expression for the chemical potential of gas phase species in terms of temperature and their partial pressure, if the temperature dependence at one reference pressure, $\mu_i(T, p^\circ)$ is known. Taking the reference pressure p° to be 1 atm at reference temperature $T = 298.15$ K, the $\mu_i(T, p^\circ)$ term can be calculated from the entropy and enthalpy values tabulated in thermodynamic data as¹⁵,

$$\mu_i(T, p^\circ) = E_{elec}^i + E_{ZPVE}^i + \left[H^i(T, p^\circ) - H^i(298.15K, p^\circ) \right] - T \left[S^i(T, p^\circ) - S^i(0K, p^\circ) \right]. \quad (4.12)$$

Chapter 4. Surface State of Ru catalysts

As shown in Figure 4.2, we are interested in a gas phase reservoir comprised of H_2 and H_2O . The corresponding enthalpy and entropy values taken from the thermochemical tables for H_2 and H_2O are given in Table 4.3. Under thermodynamic equilibrium, the following relationships

Table 4.3: Enthalpy and entropy values for H_2O and H_2 taken from the thermochemical tables²⁴.

H_2O			H_2	
T (K)	S (J/(mol.K))	H (J/mol)	S (J/(mol.K))	H (J/mol)
0	0	-9.904	0	-8.467
100	152.388	-6.615	100.727	-5.468
200	175.485	-3.282	119.412	-2.774
298.15	188.834	0	130.68	0
300	189.042	0.062	130.858	0.053
400	198.788	3.452	139.216	2.959
500	206.534	6.925	145.737	5.822
600	213.052	10.501	151.077	8.811
700	218.739	14.192	155.606	11.749
800	223.825	18.002	159.548	14.702
900	228.459	21.938	163.051	17.676
1000	232.738	26	166.216	20.68

hold,

$$\mu_H(T, p) = 1/2\mu_{H_2}(T, p), \quad (4.13)$$

and

$$\mu_O(T, p) = \mu_{H_2O}(T, p) - \mu_{H_2}(T, p), \quad (4.14)$$

which signify an equilibrium between the solid phase and the gas phase and between species within the gas phase. In addition, the formalism still holds when there is a liquid phase present (Figure 4.3) since under a full thermodynamic equilibrium species will have the same chemical potential in the liquid and gas phase.

Furthermore, one could fix the $\mu_O(T, p)$ by fixing the chemical potential of H_2O . This was achieved by assuming that water is always at the saturation vapor pressure which, in turn, is a function of temperature. The saturation vapor pressure of H_2O was obtained by using the following polynomial²⁵

$$\ln\left(\frac{p}{p_c}\right) = \frac{T_c}{T} [a_1\tau + a_2\tau^{1.5} + a_3\tau^3 + a_4\tau^{3.5} + a_5\tau^4 + a_6\tau^{7.5}] \quad (4.15)$$

where $T_c = 647.096$ K and $p_c = 22.064$ MPa are the critical temperature and pressure of water, respectively, and

$$a_1 = -7.85951783; a_2 = 1.84408259$$

$$a_3 = -11.7866497; a_4 = 22.6807411$$

$$a_5 = -15.9618719; a_6 = 1.80122502.$$

Once the pressure of water is fixed at the corresponding saturation vapor pressure at the given temperature, one could present all the thermodynamic information in terms of more chemically familiar quantities i.e. temperature and pressure of H_2 .

4.3 Computational Details

The computational set up employed for this work was similar to what has been described in Section 3.2 with the exception that symmetric slabs were used to avoid the expensive dipole corrections in the DFT optimization step. The symmetric slabs were also found to be necessary in the subsequent MMSolv calculations: non-symmetric slabs led to a non-zero binding energy for MM water molecules even very far from the surface, probably because of the interaction with the infinite dipole generated by non-symmetric slabs. The different parameters for the three facets are listed in Table 4.4. Ru(10-10) and Ru(10-11), unlike Ru(0001), can have two different terminations but only the most stable ones were considered.

Table 4.4: Simulation parameters for the three facets considered in this work.

Facet	Supercell	No. of Layers	Vacuum (\AA)	K-point
Ru(0001)	p(3x3)	5	31	5x5x1
Ru(10-10)	p(3x2)	5	30	5x5x1
Ru(10-11)	p(2x3)	5	31	5x5x1

Computational Details of MM calculations

The MMSolv calculations were performed using the in-house developed, stand alone SolvHybrid package. SolvHybrid requires the optimized CONTCAR and corresponding OUTCAR files from a VASP calculation done using the dDSc dispersion correction. As a first step, the CONTCAR files for both the reference configuration and the given configuration are extended in the planar direction by a factor of 5 to construct a bigger supercell for the MM calculation. A TIP3P water box of 30 \AA is added to the extended supercell of the given configuration and then the water is cut around the edges to achieve a water layer only above and below the surface (Figure 4.6). An initial minimization of the water box is performed which is then exactly

Chapter 4. Surface State of Ru catalysts

replicated over the reference configuration to obtain a similar starting point of MM water for thermodynamic integration (TI). The TI is performed according to the criterion described in Chapter 2 with an initial minimization of 100 steps using steepest descent method for each window which is followed by 100000 steps of heating phase where temperature is gradually increased from 5 K to 300 K at constant pressure (1 bar) using weak coupling algorithm with coupling strength of 1 ps. Finally an equilibration of 150000 steps is done at constant temperature using Langevin dynamics with a collision frequency of 2.0 ps^{-1} . SHAKE algorithm²⁶ was used for the H atoms of the TIP3P water in both heating and equilibration steps which allowed for a 2 fs time step. Only the MM water was allowed to move while the DFT part (Ru + adsorbate) were kept fixed.

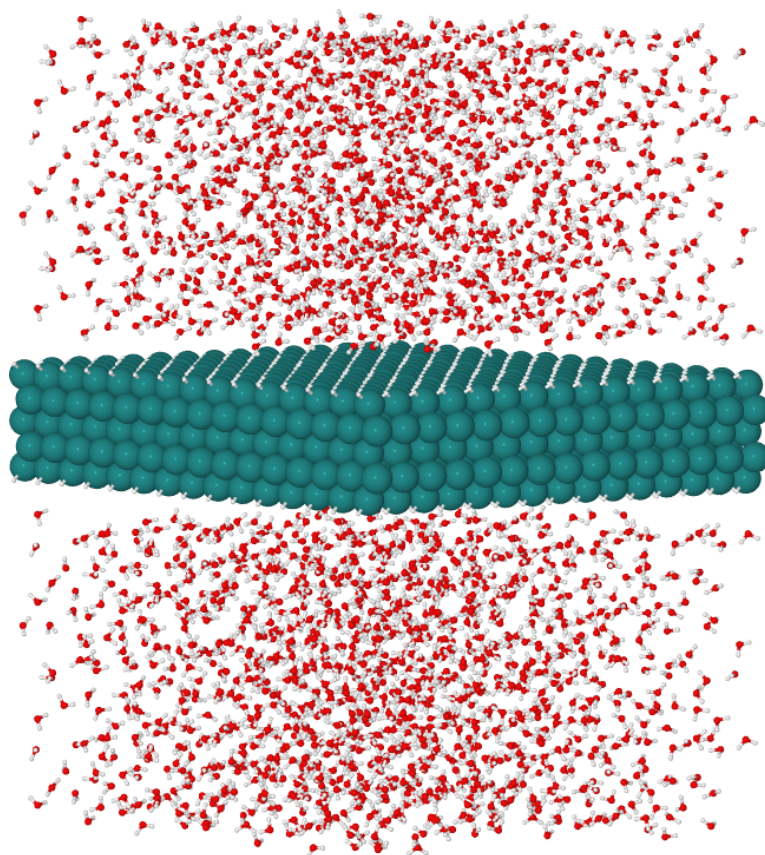
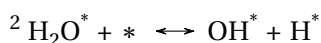
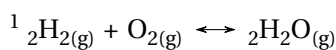


Figure 4.6: The extended supercell with TIP3P water above and below a 1MLH@Ru(0001) surface used for MMSolv calculation. The box is periodic in all directions.

4.4 Results and Discussion

4.4.1 Single atom/molecule adsorption

To facilitate the phase-space sampling by the random generator described in Section 4.2.2, the adsorption free energy of different atomic and molecular species (at single atom/molecule coverage) was computed on all possible adsorption sites available on the three different facets of Ru considered in this study. The obtained results are reported in Table 4.5. The values for H and H₂O were calculated w.r.t H_{2(g)} and H₂O_(g) as references whereas the following references were used for O and OH:



where g signifies the gas phase; and *, X* indicate the bare surface and adsorbed species, respectively.

It is evident from the results that the species show preferences for different adsorption sites. On Ru(0001), for example, H is most stable on fcc site with hcp being close second. However, O on the same termination strongly prefers hcp site. Moreover, some species like OH display different adsorption geometry based on the adsorption site they are adsorbed at: OH at fcc site displays vertical adsorption geometry where O is bound to the 3-fold hollow site and H is pointing vertically above the O where on bridge or top site OH displays a rather horizontal adsorption geometry. H₂O is almost always bound to the top site on all three facets. The corresponding optimized geometries were used to build the adsorption-distance dictionary required for the random generator.

4.4.2 Validation of MMSolv approach

The unique aspect of our study was to include the solvation effects in the thermodynamic model to explicitly account for the liquid water ubiquitous in biomass transformations involving Ru as a catalyst. This was done using the in-house developed MMSolv approach which is an explicit-solvation scheme. Since it's the first time this scheme has been employed to treat systems like these, we first investigated the validity and reliability of this approach.

Chapter 4. Surface State of Ru catalysts

Table 4.5: Adsorption free energies ($\text{kJ}\cdot\text{mol}^{-1}$) of different species on three different Ru facets at different adsorption sites. The naming scheme of the sites is the same as in Figure 4.5. The entropic and enthalpic contributions to the free energy were computed under ideal-gas, harmonic approximation at 160 °C temperature and 1 atm pressure. The –'s signify either a transition state or movement to a different site as a result of optimization.

Ru(0001)				
Site	H*	O* ¹	OH* ²	H ₂ O*
fcc	-35	-3	-52	–
hcp	-28	-32	-46	–
top	-8	–	-45	14
bridge	–	–	-17	–

Ru(10-10)				
Site	H*	O* ¹	OH* ²	H ₂ O*
H1	-34	-25	-75	–
H2	-24	–	-22	–
B1	–	–	–	–
B2	-37	-25	-68	–
B3	–	-8	–	–
T1	–	–	–	–
T2	–	17	-49	4

Ru(10-11)				
Site	H*	O* ¹	OH* ²	H ₂ O*
H1	-36	-19	-92	–
H2	-39	-45	-135	–
H3	-39	-31	-107	–
B1	–	–	-61	–
B2	–	–	-91	–
B3	–	–	–	–
B4	–	-15	-114	–
B5	-31	3	-112	–
T1	–	–	–	–
T2	–	–	–	4

Self-consistency

Self-consistency of the MMSolv approach was confirmed by building self-consistency cycles for well-known, ordered adsorption structures on all three facets which are shown in Figure 4.7. For Ru(0001), well-known, half dissociated monolayer of H₂O (H₂O-001, top-left) along with monolayers of H (H-001, top-right) and O (O-001, top-center) were employed to check the consistency cycle. Surprisingly, our results show that H-001 and O-001 are better solvated

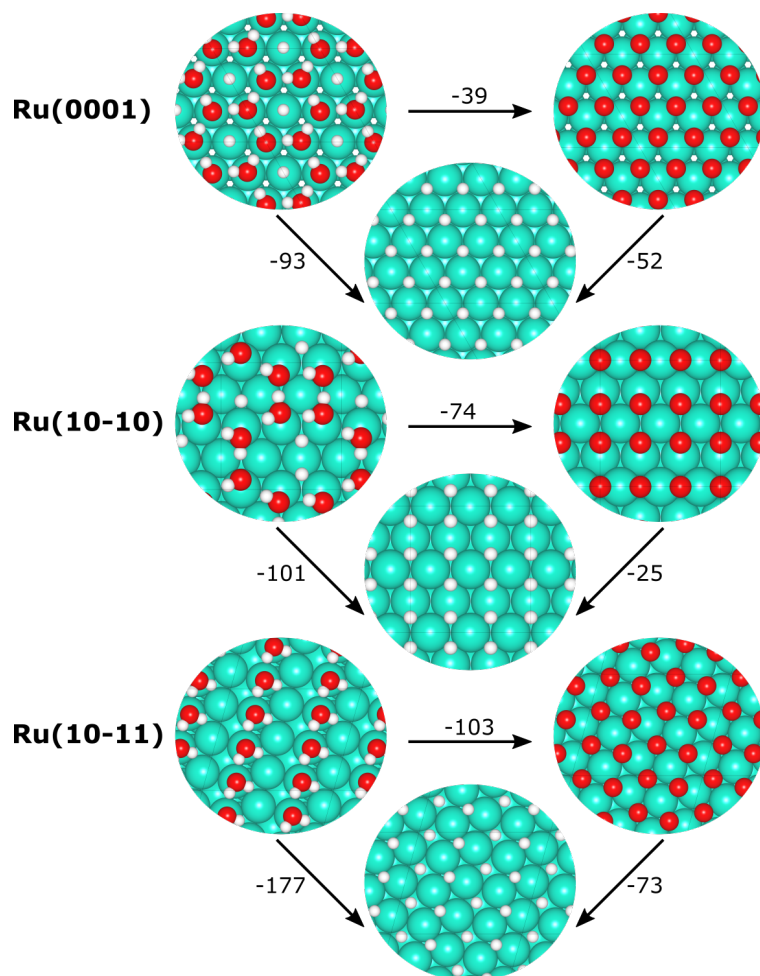


Figure 4.7: Self-consistency cycles of MMSolv approach. The values are ΔG_{solv} in kJ.mol^{-1} .

than H₂O-001 and that H-001 is more solvated than O-001. The biggest change in solvation enthalpy (-93 kJ.mol^{-1}) is observed when going from H₂O-001 to H-001 which is 54 kJ.mol^{-1} more stable than the corresponding change for O-001. This difference in H-001 and O-001 is confirmed by -52 kJ.mol^{-1} solvation change in going from O-001 to H-001 making over all cycle consistent. This consistency allows for an arbitrary choice of the reference state and, consequently, the arrows in Figure 4.7 can be reversed and the corresponding enthalpy change of solvation can be obtained by simply a sign change.

The consistency cycle was confirmed for other two terminations using corresponding H and O monolayers, hereby referred to as H-100, O-100 for Ru(10-10) and H-101, O-101 for Ru(10-11), and adsorption geometries of intact or dissociated water species, hereby referred to as H₂O-100 for Ru(10-10) and H₂O-101 for Ru(10-11). The H₂O-100 configuration was

Chapter 4. Surface State of Ru catalysts

generated using the random generator and the subsequent optimization leads to a rather ordered structure with 4, 6 and 8 membered rings of intact and dissociated water species. This serves as an example of the promise of our approach involving the random generator followed by DFT optimization to sample the complicated phase space. Quite like H-001, H-100 and H-101 are better solvated relative to their corresponding O-hkl and H₂O-hkl adsorption geometries.

The H₂O-001, H₂O-100, and H₂O-101 adsorption geometries were subsequently used as reference configurations to perform the MMSolv calculations for other ordered and random configurations.

Characterization of MM water

The self-consistency cycles in Figure 4.7 serve as the first step towards establishing the reliability of the MMSolv approach as well as SolvHybrid program used to run the MMSolv simulations. However, the observed values of ΔG_{solv} are hard to rationalize at first glance: one would expect the O-hkl and H₂O-hkl adsorption geometries to be better solvated than H-hkl surfaces as the former are better suited to make more hydrogen bonds with the MM water. To understand these surprising results of ΔG_{solv} , we analyzed the structure of MM water above the frozen metal-adsorbate surface. First, we looked at the distribution of O and H atoms present in MM water as a function of distance from the metallic surface. The corresponding graphs are given in Figure 4.8 for H₂O-001, H-001, O-001 and another random adsorption configuration containing two fully dissociated water molecules (OH-001) on Ru(0001) termination. Since H₂O-001 was used as the reference configuration for MMSolv scheme, the graph for H₂O-001 presented here corresponds to the MMSolv simulation of the OH-001 configuration. However, the distribution curves were similar in all cases for the H₂O-001 configuration irrespective of the other configuration for which solvation was simulated.

Looking at the shape of the distribution curves one immediately sees that they all converge to 1 (O-WAT, 2 for H-WAT) far from the surface which is the expected bulk-like behavior as water moves away from the surface. Secondly, all the curves involve a first peak (x_{peak} corresponds to the distance at which O-WAT shows highest value) which shows a accumulation of the water at the interface. A useful quantity one could extract is the estimate of the area under this first peak which would give an indication of the number water molecules in the first layer ($N_1^{H_2O}$). These numbers, along with ΔG_{solv} values, have been tabulated in Table 4.6 which shows that O-001 has the highest number of H₂O molecules in the first layer followed by OH-001, H-001 and H₂O-001, respectively. This in part explains the favorable enthalpy change for H-001, however, highest value of $N_1^{H_2O}$ for O-001 seems at odds with the fact that O-001 has the lowest enthalpy change upon solvation. We believe this is because of the rather long-range

4.4. Results and Discussion

Table 4.6: Number of H₂O molecules in the first layer above the surface calculated as the integral of first peak in the graphs given in Figure 4.8 and the corresponding solvation enthalpy change for four adsorption configurations of Ru(0001).

Config.	$N_1^{H_2O}$	ΔG_{solv}
H2O-001	297	0
H-001	337	-93
O-001	462	-39
OH-001	393	-191

structuring observed in the distribution of MM H₂O above O-001 adsorption configuration which in turn can be ascribed to the interaction of MM H₂O with an infinite surface dipole generated by the separation of non-negligible charges (-0.2e on O; +0.2e on Ru). Similar separation of charges is indeed present in H-001 as well, however, the charges are small in magnitude (-0.1 for H; +0.1 for Ru). This surface dipole causes accumulation of a large number of water molecules near the interface, however, the long-range structuring results in loss of solvation capability of water.

Furthermore, the random configuration OH-001, which has a mixture of O and H species on the surface and has a coverage of 0.66ML, has the highest enthalpy change of solvation, even more than that of H-001 and O-001 combined. This behavior was observed for other similar configurations with mixed O and H species on the surface. This can be rationalized on the similar grounds as before: it has a higher value of $N_1^{H_2O}$ than that of H-001 and it lacks the long-range structuring observed for O-001. The O and H species on the surface act in some synergistic fashion to allow MM water closer approach to the surface (signified by the lowest x_{peak} value) which could account for a better solvation of the surface. Moreover, a closer look at the distribution graphs of O-001 and OH-001 reveals that H-WAT for OH-001 has a stronger, longer tail (below 2.5 Å) and has a peak at $x > x_{peak}$ hinting at a H₂O orientation with one H pointing down to better engage in a hydrogen bond with O species on the surface as well as with the exposed surface atoms. This special orientation is facilitated by the free-space pockets available between O and H species (Figure 4.9).

We would like to emphasize here that such close approach of MM water to the surface brings into question reliability of the underlying UFF parameters to account for a potentially chemisorption regime. The UFF parameters we have used were parameterized against H2O-001, O-001 and H-001 which have full monolayer coverages and expose very little to no free pockets of Ru atoms. Extending these UFF parameters to sub-monolayer coverages similar to those in OH-001 might induce significant force-field-based error in the corresponding values of the computed changes in solvation free enthalpies. This is the theme of the on going work aimed at improving the UFF parameters to better simulate the interactions of MM water approaching very close to the surface. In conclusion, the MMSolv scheme adopted here is well suited to include the solvation effects explicitly and can be systematically improved upon.

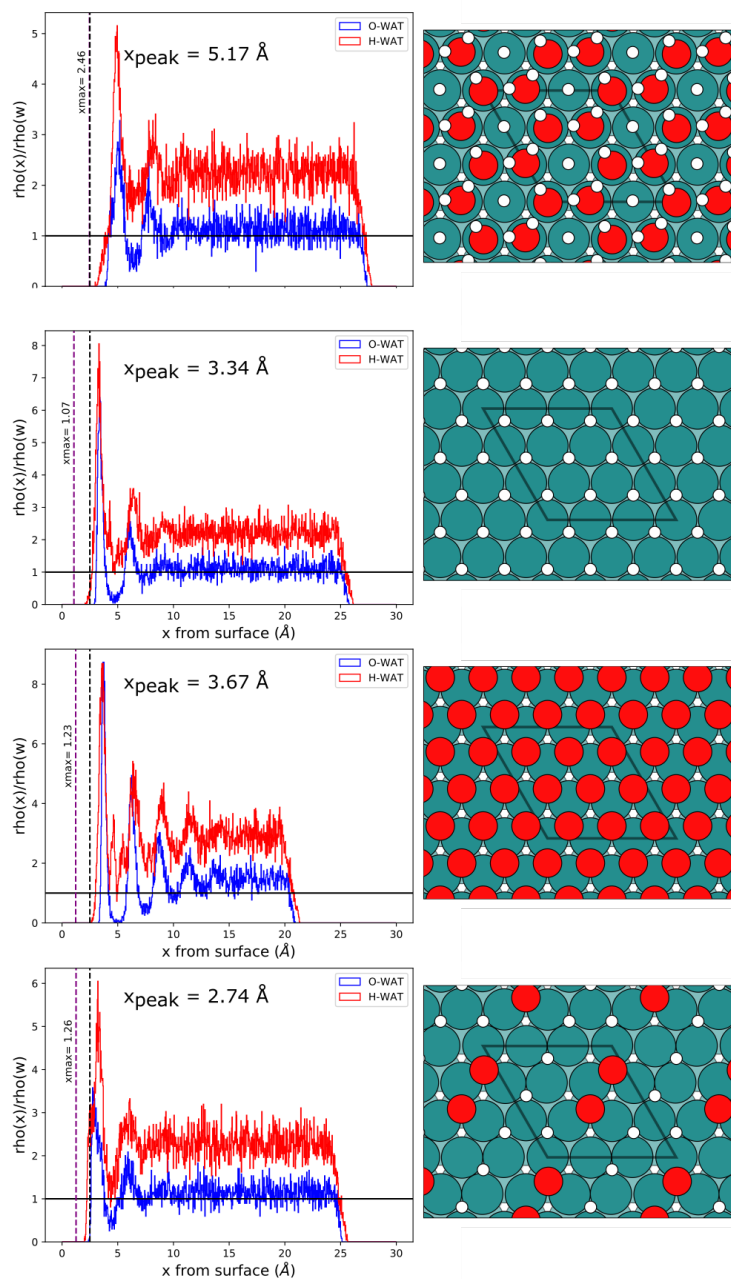


Figure 4.8: Distribution of O and H atoms present in TIP3P water during the equilibration run of the MMSolv calculation as a function of distance from the average height of the top most layer of Ru atoms. Results are averaged over every 10000 steps of the simulation and are normalized with respect to bulk water. x_{peak} is the position at which O-WAT has highest value; dashed black line is 2.50 Å; x_{max} , and the dashed purple line, is the position of the highest lying adsorbate atom.

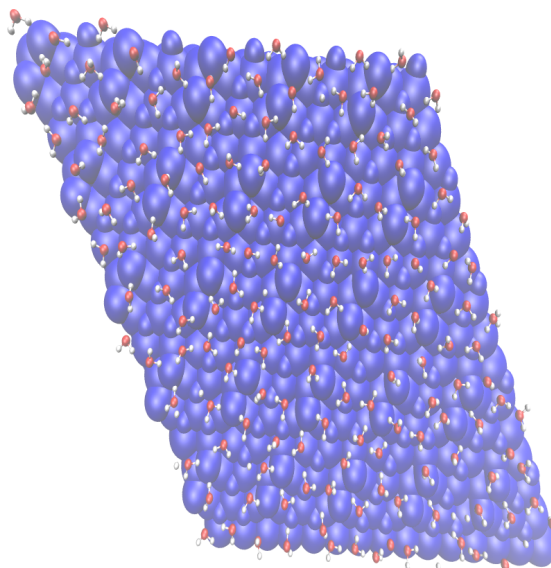


Figure 4.9: A snapshot of the MM water molecules in the first layer over OH-001 configuration taken from the final point of the equilibration trajectory. The DFT-optimized part is blue with smaller spheres at the top corresponding to H and the larger spheres to O atoms.

4.4.3 Systematic adsorption of H and O

Since H and O adsorb dissociatively on Ru surface and could lead to ordered adsorption structures, we studied their systematic adsorption from single atom up to 1ML coverage. We consider water, water vapor to be precise, as the source of O atoms on the surface. In principle, water is expected to produce OH and H_2O species too on the surface, however, in this section we simplify the problem and assume that only O species are produced on the surface. Furthermore, in this section, we restrict the phase space to only adsorption structures of H and O, separately, and ignore mixed structures like OH-001 configuration in Figure 4.8.

The simplest situation one could imagine is to consider only a pressure of H_2 . This should give rise to ordered H adlayers on different Ru terminations. A variation of pressure and temperature can result in different coverages on the surface under a thermodynamic equilibrium with the surrounding gas-phase reservoir, therefore, we have systematically studied all coverages starting from one H atom up to a monolayer. At each coverage, all possible combinations of putting corresponding number of H atoms were checked to find the most stable distribution of adsorbed atoms.

On Ru(0001) surface, the preferred adsorption site for H is fcc from single atom up to 1ML coverage. With increasing coverage, the H atoms tend to bind to fcc sites such as to increase their lateral distances. Figure 4.10 shows the most stable adsorption geometries of H on Ru(0001) at each coverage as well as the thermodynamic map (T-p map) for the stability of different phases

Chapter 4. Surface State of Ru catalysts

in terms of temperature and pressure of H_2 . The map is mostly comprised of 1ML coverage of H, the H-001 configuration discussed above and labelled 9/9 on the map; the bare Ru(0001) surface, labelled 0/9 on the map and small regions in between where intermediate coverages are most stable. It is worth mentioning that the T-p map in Figure 4.10 included the vibrational contributions for the calculation of the ΔG_{ads}^{gas} . This was achieved by calculating the normal modes at the same DFT level for the adsorbate atoms only; the vibrational contribution from the metallic atoms was ignored.

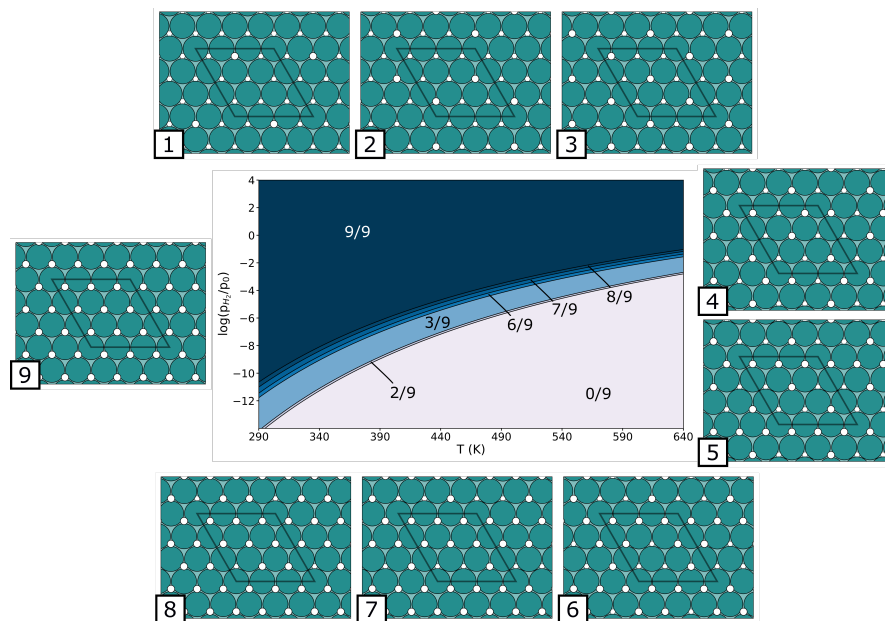


Figure 4.10: The most stable adsorption geometries of H for different coverages on Ru(0001) surface and the corresponding T-p map displaying the stability of different adsorption phases.

On Ru(10-10), the preferred adsorption site for H at lower coverages is H1, however, with increasing coverage the H atoms tend to occupy B2 sites as well. Figure 4.11 gives the most stable adsorption geometries at different coverages along with the corresponding T-p map. First, it is noteworthy that, unlike Ru(0001), on Ru(10-10) the H atoms tend to form clusters with increasing coverages, for example, see the inset in Figure 4.11 corresponding to 4/12 coverage. The T-p map for Ru(10-10) is significantly different than that of Ru(0001). First, the region of stability for 1ML coverage, H-100 surface and labelled 12/12 on the map, is much smaller compared to the corresponding region for H-001 surface: it requires a much higher pressure, 7 order of magnitudes at 290 K temperature, to achieve a 1ML coverage on Ru(10-10). The regions of intermediate coverages are quite prominent, especially 9/12ML coverage, and, consequently, fewer intermediate coverages are thermodynamically stable.

Ru(10-11), on the other hand, shows a T-p map similar to Ru(0001) with two big regions

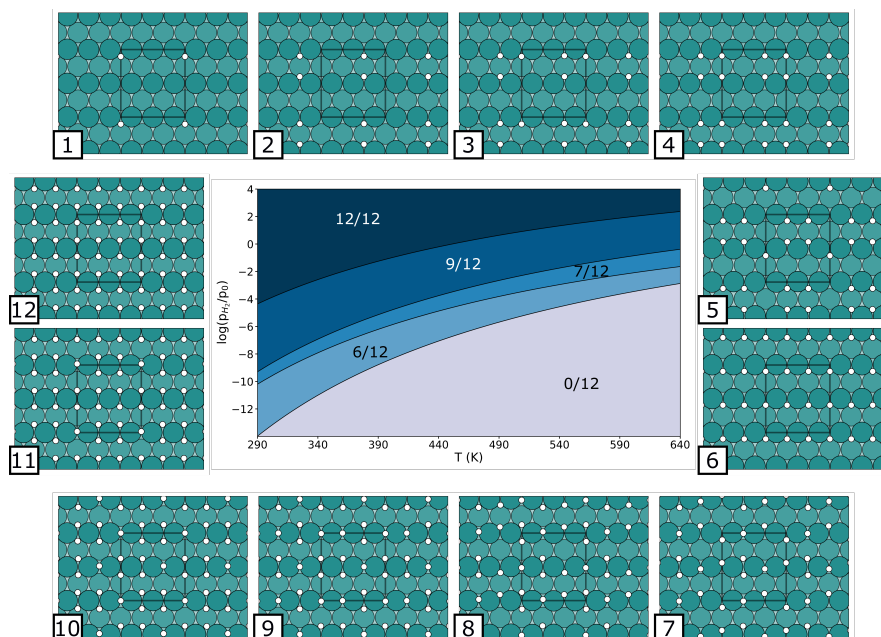


Figure 4.11: The most stable adsorption geometries of H for different coverages on Ru(10-10) surface and the corresponding T-p map displaying the stability of different adsorption phases.

corresponding to 1ML coverage, H-101 configuration, and the bare Ru(10-11) surface. Up to 0.5ML coverage, the most stable adsorption site is H2 and any further number of H atoms are accommodated at H3 hollow sites.

As a natural next step, we considered the presence of water vapor in the system which, we assume, gives rise to ordered structures of O species on the surface. This further complicates the phase space and, in addition to H structures described above for three facets, O adsorption structures need to be included in the thermodynamic model. Fixing the pressure of water to the corresponding saturation vapor pressure at given temperature, one could construct a T-p map in terms of temperature and pressure of H₂ but with a larger phase space for each facet.

For Ru(0001), the corresponding T-p map with the enhanced phase space, along with the most stable adsorption geometries of O atoms at each coverage, is shown in Figure 4.12. The main region of thermodynamic stability is still the H-001 surface, however it is pushed up and more pressure of H₂ is required to keep the surface fully covered with H. Surprisingly, even with water vapor, the surface is prone to poisoning by O species if little or no H₂ pressure is supplied. The poisoning is further facilitated by higher temperatures and a full monolayer of O, O-001 surface, becomes most stable above 415 K at very small pressure of H₂ is supplied. Similar T-p maps were found for Ru(10-10) and Ru(10-11): the top region covered by the 1ML H surface i.e. H-100 for Ru(10-10) and H-101 for Ru(10-11); and the lower half covered by O adsorption structures at different coverages.

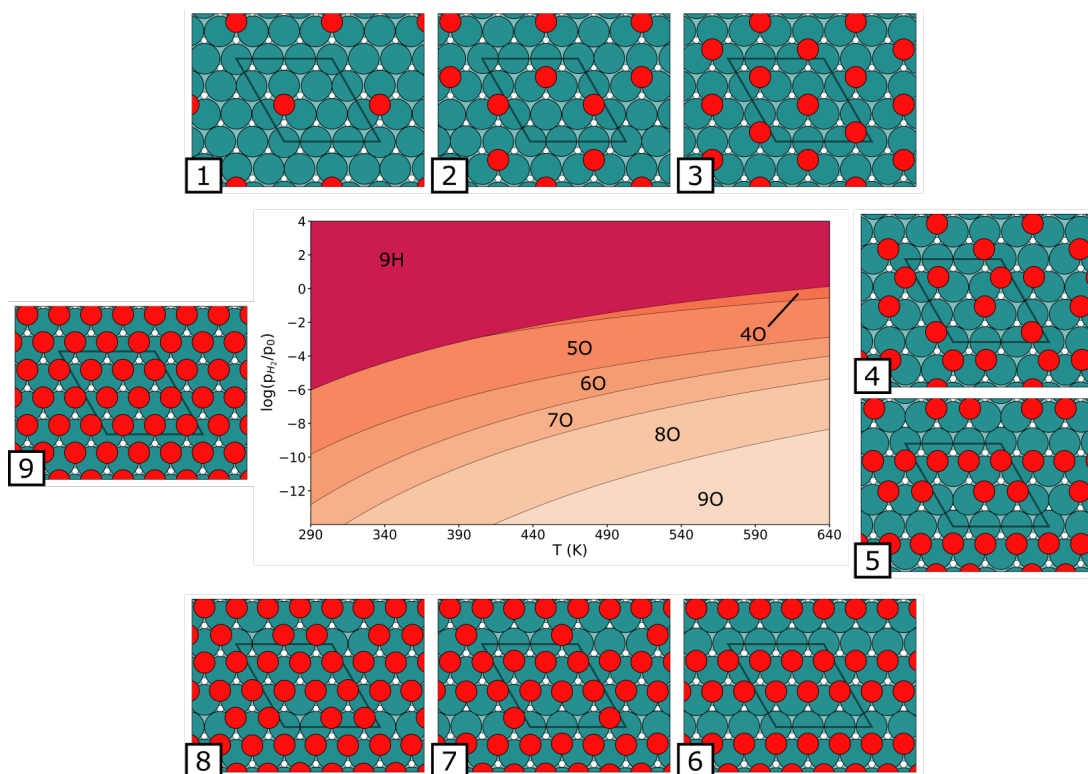


Figure 4.12: The most stable adsorption geometries of O for different coverages on Ru(0001) surface and the corresponding T-p map displaying the stability of different adsorption phases.

Using this extended phase space of Ru-H and Ru-O configurations, we looked at the potential modification in the shape of the underlying Ru nanoparticle employing Wulff construction scheme. We find that the three facets considered here display similar area fraction in a wide temperature and pressure range with Ru(0001):Ru(10-10):Ru(10-11) = 20:20:60, on average.

4.4.4 Full Phase Space: H/O/OH/H₂O

As the goal of the study is to characterize the surface state of Ru catalysts in water under a pressure of H₂, we need to include OH and H₂O species that could potentially exist on the surface as demonstrated by previous theoretical and experimental studies. This further complicates the phase space which was randomly sampled using the random generator described in Section 4.2.2. In the following we present the results for this full phase space. Two sub cases can be differentiated: presence of water, in vapor or liquid phase, in absence of H₂ and water with H₂ pressure.

Case 1: Water in absence of H₂

This case can be distinguished from the more general case where H₂ is also present by the fact that only those surface structures are possible which have O:H ratio of 1:2. This still allows for a full or partial water splitting on the surface but since there is no H₂ gas phase reservoir, no desorption of H species is possible as H₂; desorption of H₂O species is still possible. Two further subcases can be easily recognised: (i) water as vapor - typical in Fisher-Tropsch reaction, or any reaction that generates water as a product, and in surface science and (ii) water as liquid in equilibrium with its vapor - typical of reactions performed in an autoclave with a neutral gas such as N₂ or Ar. In both subcases, one could calculate $\gamma(T)$, and correspondingly ΔG_{ads} , as

$$\gamma(T) = \frac{1}{2A} [G_{O:H=1:2} - n_{Ru}\mu_{Ru} - n_{H_2O}\mu_{H_2O}(T)] \quad (4.16)$$

where μ_{H_2O} is fixed by saturation vapor pressure of water which, in turn, is fixed by the temperature. This makes it a one-dimensional phase space characterized only by temperature and one could look at the stability of the different adsorption configurations by simply calculating their $\Delta G_{ads}^{gas}(T)$, if only water vapor is present, or correspondingly, $\Delta G_{ads}^{sol}(T)$, if water is treated as liquid in contact with its vapor, and then determining which one has the lowest (more negative) difference of adsorption free energy at the given temperature. It should be noted that the reference configuration for calculation of γ_{ref} must also have a O:H = 1:2, which was made possible by the choice of H₂O-hkl configurations shown in Figure 4.7 as reference for three facets considered. Furthermore, since we have used an extended sample space containing hundreds of randomly generated configurations, the vibrational contributions to the free energy were not included in this case and the subsequent cases. However, we expect this not to alter the qualitative picture of the findings we report here.

For Ru(0001), we have 111 ordered (i.e. H₂O-001 and its non-dissociated counterparts) or randomly generated configurations at various coverages which fulfill the ratio requirement. Figure 4.13 gives the plot of ΔG_{ads} in terms of temperature depicting the most stable phases at each temperature. If water is considered only as vapor, below ~ 340 K, the most stable phase is the half-dissociated monolayer of water, H₂O-001, consistent with previous surface science and theoretical studies. However, above this temperature, the most stable phase was found to be the 0.67ML OH-001 configuration described in Section 4.4.2 with two water molecules fully dissociated and O and H both binding to hcp hollow sites. This can be rationalized based on the tendency of water to easily split on Ru(0001) and the entropic gain achieved by the water being in the vapor phase as the temperature increases. Surprisingly, configurations with OH species do not appear in the stability plot and a full dissociation of water is thermodynamically

more feasible. However, there might be kinetic factors that could potentially hinder reaching these fully dissociated configurations.

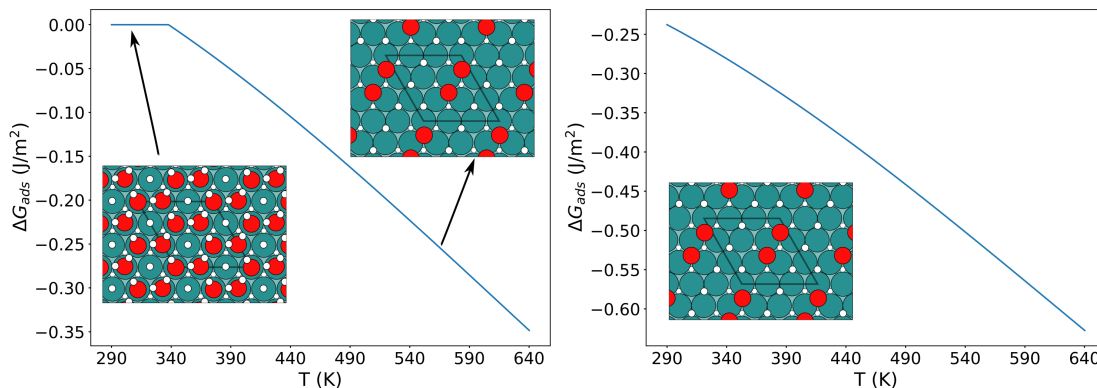


Figure 4.13: Plot of difference of adsorption free energy in terms of temperature in (left) water as a vapor at saturation pressure and (right) water as liquid in equilibrium with its vapor. The value at each temperature corresponds to the most stable phase which are shown on the plot.

When water is considered as liquid in equilibrium with its vapor at saturation pressure, one needs to take into account the solvation effects which in our case was done by calculating ΔG_{solv} using MMSolv scheme (Figure 2.5). The MMSolv calculation has been performed for 11 configurations which were subsequently included in the thermodynamic model involving solvation enthalpies. The modified plot containing the solvation effects shows that OH-001 configuration is the most stable at all temperatures. This makes sense given that OH-001 has a very high value of solvation enthalpy (Table 4.6). This result is quite surprising and indicates that liquid water is more prone to splitting than water vapor. However, more work is needed to validate the solvation scheme and gain more confidence in the solvation enthalpy values obtained thereof.

It is worth mentioning that the plots in Figure 4.13 were prepared without putting any limits on the minimum surface coverage thereby including all 111 configurations, 11 for the solvation case, in the thermodynamic treatment. In principle, that is a valid protocol as solid surface can easily exchange H₂O species with the surrounding vapor environment which could lead to a variable coverage. However, if a minimum threshold is set for the surface coverage, other configurations become more stable. For example if minimum coverage was set to 0.7ML, slightly above 0.67ML of OH-001 configuration, the new plot obtained is given in Figure 4.14 along with the new most stable configurations, both of 0.78ML coverage. Even with this coverage threshold, there were still 37 configurations in the data set and the plot obtained using these 37 configurations has remarkable differences from that given in Figure 4.13. Firstly, the temperature range of stability of H₂O-001 configuration is increased up to ~ 540 K indicating that H₂O-001 configuration is the optimum arrangement of water species on the surface at

high coverages. Secondly, the new configurations that are most stable above ~ 540 K do indeed have H_2O and OH species, however, the range of values on the y-axis is almost 3 times smaller than that in Figure 4.13 indicating that these configurations are only slightly stable than the the reference H_2O -001 configuration. This problem of having to choose a coverage threshold can be important and more work is needed to generate ample data at each coverage.

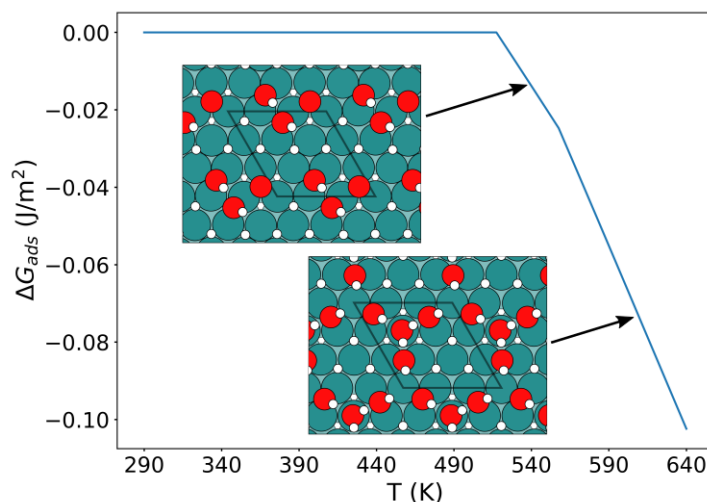


Figure 4.14: Plot of difference of adsorption free energy in terms of temperature in water vapor if minimum coverage is set to 0.7ML.

Finally, we remark that similar plots were obtained for the other two terminations considered in this work where H_2O -hkl configurations are stable at low temperatures and mixed OH-hkl configurations become stable at higher temperatures. The corresponding data sets for the other two terminations are still comparatively small and more configurations are needed to amply sample the phase space and to draw valid conclusions.

Case 2: Water under a pressure of H_2

The second, more general and relevant, case accounts, other than water in vapor or liquid form, for the catalyst surface to be subjected also to a pressure of H_2 during the reaction, as is common during many chemical transformation involving biomass. Presence of H_2 makes it a 2-dimensional phase space, expressed in terms of either $\mu_{\text{H}}(T, p)$ and $\mu_{\text{O}}(T, p)$ or, if one fixes the pressure of H_2O at the corresponding saturation vapor pressure at the given temperature, temperature and pressure of H_2 , p_{H_2} . Figure 4.15 gives the most stable adsorption configurations and the corresponding T-p maps for Ru(0001) both in gas or solvent phase for Ru(0001). The map for the gas phase included 316 configurations; MMSolv treatment was performed for 216 configurations which were subsequently included in the preparation of T-p map for the solvent phase.

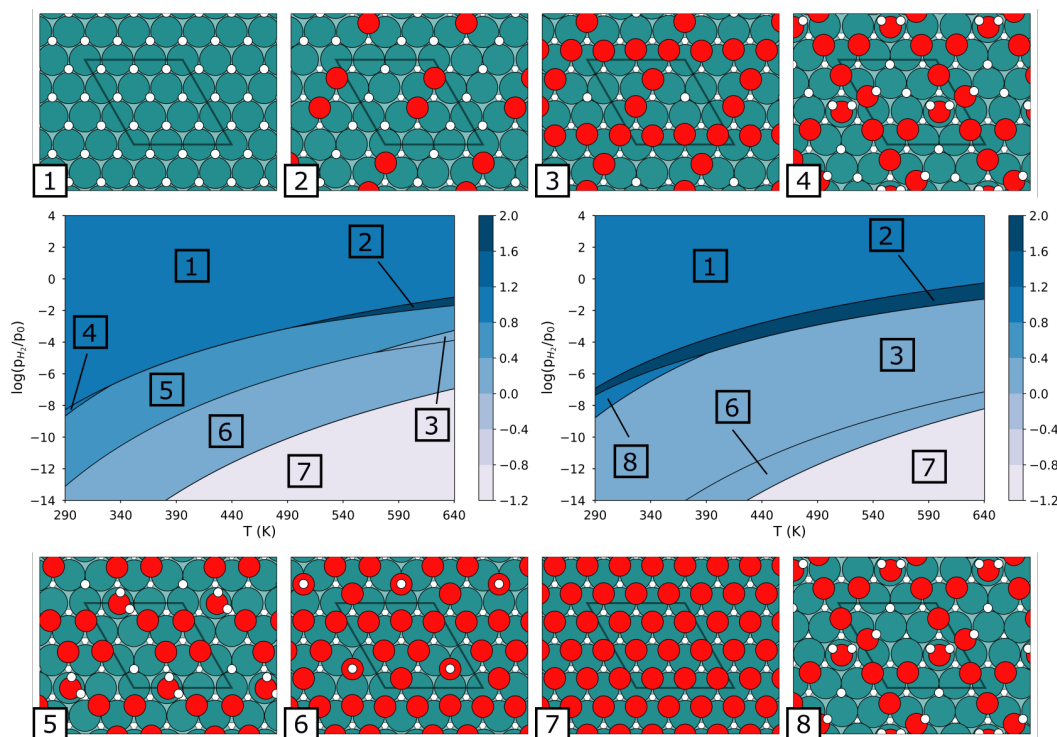


Figure 4.15: The most stable adsorption geometries of H₂O/OH/O/H on Ru(0001) exposed to a pressure of H₂ and the corresponding T-p maps displaying the stability of different adsorption phases in (left) water as vapor at saturation pressure and (right) water as a liquid in equilibrium with its vapor.

Even with the extended phase space, the most stable surface topology at experimental conditions relevant in biomass is still the H-001 configuration, labelled **1** on the T-p maps in Figure 4.15, both for vapor and liquid phase. The second most stable surface topology at lower p_{H_2} is **5** configuration in the vapor phase which is replaced by the **2** and **3** configurations in the liquid phase confirming again that liquid water is more susceptible to splitting than water vapor. At very low values of p_{H_2} , and high temperatures, the surface is fully oxidized as shown by regions labelled **6** and **7** - the full monolayer O-001 configuration.

The T-p maps in Figure 4.15 give the most stable adsorption configurations at each (T,p) value, however, it might be worthwhile to look at the stability of these phases relative to other phases which do not appear in the T-p maps. This can be achieved by looking at the slices of the T-p maps at given value of p_{H_2} . This should give plots similar to those in Figure 4.13 and Figure 4.16 gives the corresponding plots at $p_{\text{H}_2} = 1$ bar for both vapor and liquid phase. As can be clearly seen that at temperature values relevant in the biomass i.e. 300-500 K, H-001 configuration is more than 1 J.m⁻² stable than the next most stable phase.

For the other two facets, Ru(10-10) and Ru(10-11), similar T-p maps were obtained even at

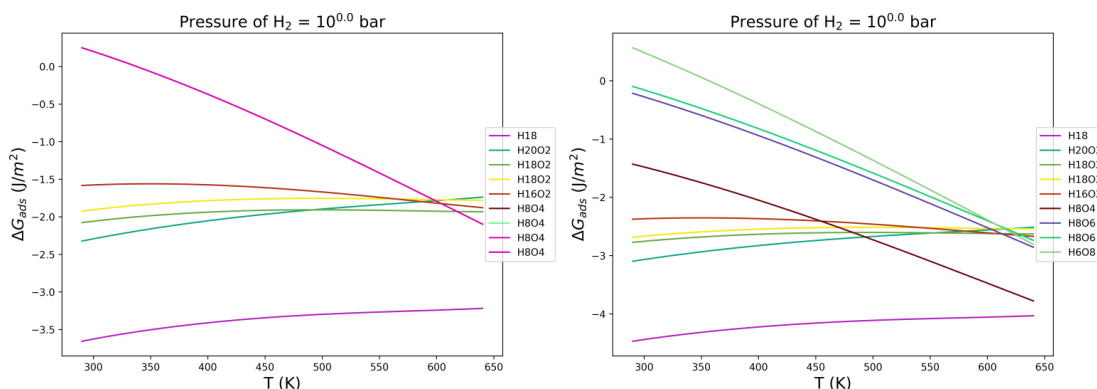


Figure 4.16: Plots of difference of adsorption free energy at 10 bar H_2 pressure in (left) water vapor at saturation pressure and (right) liquid water in equilibrium with its vapor.

the enhanced phase space with H-hkl configurations being the most stable at experimentally relevant conditions. These findings are in contrast with previous experimental and theoretical studies which ascribed the higher activity of Ru catalysts in water to the presence of H_2O species on the surface, or hypothesized the formation of Ru-OH species leading to a diminished reactivity of the reused catalyst.

4.5 Conclusion

Ru is an important catalytic material and supported-Ru catalysts are ubiquitous in chemical reactions involving biomass. Characterizing the surface state of these catalysts which are often subjected to high pressures of H_2 in vapor or liquid water is still a puzzling question. Here we report the result of surface characterization of supported Ru-catalysts using well-established technique of *ab-initio* atomistic thermodynamics along with a random generation scheme to amply sample the complicated phase space of adsorption configurations that might result when Ru is exposed to water and H_2 . On three separate, most abundant facets of a typical Ru nanoparticle, the most stable adsorption topology at relevant conditions of temperature and pressure is H-hkl both in liquid or vapor water. This is in line with our work on isosorbide where a partial coverage of H was assumed *a-priori* (3). The surface terminations, however, are prone to a partial or full oxidation at high temperatures if little or no H_2 pressure is supplied. We have also implemented an explicit solvation scheme to account for the liquid water in these reactions and we have found that solvation tends to stabilize H-hkl, O-hkl and mixed OH-hkl configurations more than the configurations with OH and H_2O species on the surface and that liquid water is more prone to splitting than water vapor. These findings are surprising and in contrast with previous theoretical models, which assumed presence of chemisorbed H_2O species on the surface to account for higher reactivity of Ru in liquid water, and experimental observations which attributed the passivation of Ru catalyst over multiple usage cycles to

Chapter 4. Surface State of Ru catalysts

formation of Ru-OH species.

In perspective, more sampling of the phase space is required to gain better confidence in the results obtained so far. The FF parameters used for MMSolv calculations need to be validated against a robust and diverse set of adsorption configurations to better account for the solvation effects.

Bibliography

- [1] Zhao, L.; Zhou, J.; Sui, Z.; Zhou, X. Hydrogenolysis of sorbitol to glycols over carbon nanofiber supported ruthenium catalyst. *20th International Symposium in Chemical Reaction Engineering—Green Chemical Reaction Engineering for a Sustainable Future* **2010**, *65*, 30–35.
- [2] Kobayashi, H.; Matsushashi, H.; Komanoya, T.; Hara, K.; Fukuoka, A. Transfer hydrogenation of cellulose to sugar alcohols over supported ruthenium catalysts. *Chem. Commun.* **2011**, *47*, 2366–2368, Publisher: The Royal Society of Chemistry.
- [3] Fang, R.; Liu, H.; Luque, R.; Li, Y. Efficient and selective hydrogenation of biomass-derived furfural to cyclopentanone using Ru catalysts. *Green Chem.* **2015**, *17*, 4183–4188, Publisher: The Royal Society of Chemistry.
- [4] Lv, J.; Rong, Z.; Sun, L.; Liu, C.; Lu, A.-H.; Wang, Y.; Qu, J. Catalytic conversion of biomass-derived levulinic acid into alcohols over nanoporous Ru catalyst. *Catal. Sci. Technol.* **2018**, *8*, 975–979, Publisher: The Royal Society of Chemistry.
- [5] Bonnin, I.; Méreau, R.; Tassaing, T.; Jérôme, F.; De Oliveira Vigier, K. Hydrogenation of Sugars to Sugar Alcohols in the Presence of a Recyclable Ru/Al₂O₃ Catalyst Commercially Available. *ACS Sustainable Chemistry & Engineering* **2021**, *9*, 9240–9247, Publisher: American Chemical Society.
- [6] Corma, A.; Iborra, S.; Velty, A. Chemical Routes for the Transformation of Biomass into Chemicals. *Chemical Reviews* **2007**, *107*, 2411–2502, Publisher: American Chemical Society.
- [7] Akpa, B.; D'Agostino, C.; Gladden, L.; Hindle, K.; Manyar, H.; McGregor, J.; Li, R.; Neurock, M.; Sinha, N.; Stitt, E.; Weber, D.; Zeitler, J.; Rooney, D. Solvent effects in the hydrogenation of 2-butanone. *Journal of Catalysis* **2012**, *289*, 30–41.
- [8] Michel, C.; Zaffran, J.; Ruppert, A. M.; Matras-Michalska, J.; Jędrzejczyk, M.; Grams, J.; Sautet, P. Role of water in metal catalyst performance for ketone hydrogenation: a joint experimental and theoretical study on levulinic acid conversion into gamma-valerolactone. *Chem. Commun.* **2014**, *50*, 12450–12453, Publisher: The Royal Society of Chemistry.
- [9] Feibelman, P. J. Partial dissociation of water on Ru(0001). *Science (New York, N.Y.)* **2002**, *295*, 99–102, Place: United States.
- [10] Denzler, D.; Wagner, S.; Wolf, M.; Ertl, G. Isotope effects in the thermal desorption of water from Ru(001). *Proceedings of the 7th International Conference on Nanometer-Scale Science and Technology and the 21st European Conference on Surface Science* **2003**, 532–535, 113–119.

Chapter 4. Surface State of Ru catalysts

- [11] Schilling, M.; Behm, R. J. Partial dissociation of water on Ru(0001) at low temperatures – Adsorption, structure formation and hydrogen passivation effects. *Surface Science* **2018**, 674, 32–39.
- [12] Manyar, H. G.; Weber, D.; Daly, H.; Thompson, J. M.; Rooney, D. W.; Gladden, L. F.; Hugh Stitt, E.; Jose Delgado, J.; Bernal, S.; Hardacre, C. Deactivation and regeneration of ruthenium on silica in the liquid-phase hydrogenation of butan-2-one. *Journal of Catalysis* **2009**, 265, 80–88.
- [13] Rogal, J.; Reuter, K. *Experiment, Modeling and Simulation of Gas-Surface Interactions for Reactive Flows in Hypersonic Flights*; Educational Notes RTO-EN-AVT-142, Paper 2; RTO: Neuilly-sur-Seine, France, 2007; pp 2–1–2–18.
- [14] Reuter, K.; Scheffler, M. Composition, structure, and stability of RuO₂(110) as a function of oxygen pressure. *Phys. Rev. B* **2001**, 65, 035406, Publisher: American Physical Society.
- [15] Zhang, M.; Wang, W.; Chen, Y. Insight of DFT and ab initio atomistic thermodynamics on the surface stability and morphology of In₂O₃. *Applied Surface Science* **2018**, 434, 1344–1352.
- [16] Sun, Q.; Reuter, K.; Scheffler, M. Effect of a humid environment on the surface structure of $\text{RuO}_2(110)$. *Phys. Rev. B* **2003**, 67, 205424, Publisher: American Physical Society.
- [17] Frenkel, D.; Smit, B. In *Understanding Molecular Simulation (Second Edition)*, second edition ed.; Frenkel, D., Smit, B., Eds.; Academic Press: San Diego, 2002; pp 23–61.
- [18] Landau, D.; Binder, K. *A Guide to Monte Carlo Simulations in Statistical Physics*, 5th ed.; Cambridge University Press: Cambridge, United Kingdom, 2021.
- [19] Reuter, K.; Stampfl, C.; Scheffler, M. *Handbook of Materials Modeling, Part A. Methods*; Springer: Berlin, 2005.
- [20] Sanchez, J.; Ducastelle, F.; Gratias, D. Generalized cluster description of multicomponent systems. *Physica A: Statistical Mechanics and its Applications* **1984**, 128, 334–350.
- [21] Barmbaris, G. D.; Lodziana, Z.; Lopez, N.; Remediakis, I. N. Nanoparticle shapes by using Wulff constructions and first-principles calculations. *Beilstein journal of nanotechnology* **2015**, 6, 361–368, Publisher: Beilstein-Institut.
- [22] Tran, R.; Xu, Z.; Radhakrishnan, B.; Winston, D.; Sun, W.; Persson, K. A.; Ong, S. P. Surface energies of elemental crystals. *Scientific data* **2016**, 3, 160080.
- [23] Momma, K.; Izumi, F. VESTA 3 for three-dimensional visualization of crystal, volumetric and morphology data. *Journal of Applied Crystallography* **2011**, 44, 1272–1276.

- [24] Chase, M. *NIST-JANAF Thermochemical Tables, 4th Edition, Part I, Al-Co*; American Institute of Physics, 1998.
- [25] Wagner, W.; Pruss, A. International Equations for the Saturation Properties of Ordinary Water Substance. Revised According to the International Temperature Scale of 1990. Addendum to J. Phys. Chem. Ref. Data 16, 893 (1987). *Journal of Physical and Chemical Reference Data* **1993**, 22, 783–787, Publisher: American Institute of Physics.
- [26] Ryckaert, J.-P.; Ciccotti, G.; Berendsen, H. J. Numerical integration of the cartesian equations of motion of a system with constraints: molecular dynamics of n-alkanes. *Journal of Computational Physics* **1977**, 23, 327–341.



Conclusions and Outlook

Biomass-derived platform molecules hold immense potential to replace the traditional fossil-based feedstock and becoming the backbone of a greener economy with less harmful environmental footprint. This work aimed at a theoretical, atomistic understanding of the role of various parameters in industrially relevant, heterogeneously catalyzed reactions of biobased platform molecules, in particular, isosorbide. We employed the widely-used periodic density functional theory which has become the workhorse of all modern computational endeavors in heterogeneous catalysis.

In Chapter 3, we have explored the peculiar role of a very high H_2 pressure indispensable in reactions involving supported-Ru catalysts, specifically for isomerization of isosorbide. We were able to demonstrate that high pressure of H_2 leads to a coverage effect that, in turn, pushes up the otherwise very stable reaction intermediates deemed to be the bottleneck of the reaction. Furthermore, we have recognized the intrinsic structural specificity of isosorbide, rendered by its special bicyclic nature, which leads to very stable intermediates during the reaction due to combined interaction of alcohol and ether functionality with the metallic surface. The deformation-interaction analysis performed indicates that the destabilizing effect of H coadsorption is irregular for different reaction intermediates and transition states which allows a decrease in over all span of the reaction leading to a ~ 50 times increase in the TOF of reaction at 0.75 ML coverage of H. However, no clear pattern was displayed by the energy-decomposition analysis and the over all effect is a cumulative contribution arising from many different steric and to a lesser extent electronic effects.

Secondly, we also investigated the potential poisoning of supported-Ru catalysts by NH_x species during the aqueous-phase amination of isosorbide with NH_3 . Using a simplified microkinetic model based on DFT energies, we find that the surface is mostly covered with NH_3 and NH species, concentration of NH increases with increasing temperature if pressure of H_2 is kept fixed indicating that increased temperature leads to increased poisoning. At constant temperature, on the other hand, higher H_2 pressure simply reverses the surface concentrations of NH_3 and NH thereby lowering the potential passivation of the catalyst as NH_3 is less poisoning than NH species. This further hints at the potential role of H_2 in amination

Chapter 4. Surface State of Ru catalysts

reaction as a protecting agent.

In Chapter 4 we report the results of surface characterization of supported Ru-catalysts using well-established technique of ab-initio atomistic thermodynamics along with a random generation scheme to amply sample the complicated phase space of adsorption configurations that might result when Ru is exposed to water and H_2 . We find that on three separate, most abundant facets of a typical Ru nanoparticle, the most stable adsorption topology at relevant conditions of temperature and pressure is H-hkl both in liquid or vapor water. This is in line with our work on isosorbide where a partial coverage of H was assumed *a-priori*. The surface terminations, however, are prone to a partial or full oxidation at high temperatures if little or no H_2 pressure is supplied.

We have also implemented an explicit solvation scheme to account for the liquid water in these reactions and we have found that solvation tends to stabilize H-hkl, O-hkl and mixed OH-hkl configurations more than the configurations with OH and H_2O species on the surface and that liquid water is more prone to splitting than water vapor. These findings are surprising and in contrast with previous theoretical models, which assumed presence of chemisorbed H_2O species on the surface to account for higher reactivity of Ru in liquid water, and experimental observations which attributed the passivation of Ru catalyst over multiple usage cycles to formation of Ru-OH species.

In perspective, the reaction profile data for isomerization can be used to construct ab-initio microkinetic models to better understand the coverage of various reaction intermediates under a pressure of H_2 and temperature which, in turn, will be useful for the elucidation of the selectivities observed in amination as they both share the same first step involving the dehydrogenation of alcohols into corresponding ketones.

On the surface state characterization, the FF parameters used for the QM/MM explicit water model need to be improved by doing more scans of different water topologies at DFT level. More enhanced sampling of the phase space is required, especially at higher coverages, to gain confidence in the thermodynamic model which is only as predictive as the configuration fed into it.